A proposed Origin and Timeline for Plagioclase and Pyroxene bearing Clasts in Martian Meteorite NWA 7034

MSc Thesis

Line Schug Wageningen University and Research 30.03.2019

ABSTRACT

NWA 7034 is a unique Martian meteorite. It is one of the few pieces of Martian crust that has made its way to Earth. It has been classified as a breccia, meaning it is a clast composed of older clasts, bound by a matrix. This made it possible to study the compositions and textures of multiple generations of rocks, enriching our knowledge about the processes that defined rock formation on the surface of Mars over billions of years.

Based on compositional differences of feldspars and pyroxenes, and textural differences of basaltic clasts, it is likely that NWA 7034 underwent at least two generations of brecciation, resulting in a diverse assembly of clasts. High pressure shock textures, such as fractures, twinning in pyroxene, quenched pyroxene and plagioclase glass, were observed in older generation clasts and to a lesser extent in the youngest generation clasts. The distribution of shock textures indicate that the source rock underwent at least three impacts prior to impacting on Earth. Using spectral analysis, the compositions of feldspars and pyroxenes was obtained. Pyroxenes were magnesic and occurred both as ortho- and clinopyroxene, implying different cooling rates and therefore multiple heating events. Formation temperatures of 1210-<500˚C ± 50˚C in older generation clasts, and 1225-600˚C ± 50˚C in the youngest generation clasts were inferred from their composition. Both alkali and plagioclase feldspars were found. The plagioclase was sodic, denoting a formation temperature of 1260-1150˚C ± 25˚C in older generation clasts, and 1245-1150˚C ± 25˚C in the youngest generation clasts. Unless part of a gabbroic rock, alkali feldspar occurred as perthite, implying a formation temperature of ≤1000˚C ± 50˚C, and pressure <0.5 GPa. In gabbroic rocks, its composition suggests a crystallization temperature of ≤1070˚C ± 50˚C. Bulk rock composition and general mineralogical assemblage match mineral composition of Gusev crater, which has been suggested to be situated above an alkali volcanic source. Furthermore, a cumulate clast was found in NWA 7034 whose composition matches a Noachian-age (~4.1 – ~3.7 Ga) layered intrusion that was exposed following the meteorite impact that formed Gusev crater during the Hesperian period (~3.7 – ~3.0 Ga). Petrology and molar composition of plagioclase and pyroxene in the subsamples closely match the clasts analysed at Gale crater. It is likely that rocks sourced from both these regions ended up in NWA 7034, and that its ejection location was in the zone that encompasses impact ejecta from both Gale and Gusev crater.

Overall, the petrologic evidence suggests that NWA 7034's formation and alteration history began with alkaline rocks formed in the Pre-Noachian (~>4.4 Ga), followed by accumulation, brecciation and alteration occurring throughout the Amazonian period (~3.0 Ga – present) until its ejection from Mars and subsequent impact on Earth (~7.3 Ma).

ACKNOWLEDGEMENTS

I would like to thank Stephen Mojzsis and Nigel Kelly for their guidance and inspiration, the amazing opportunity to study NWA 7034, and inviting me to be there in person to watch and participate first-hand how data was being obtained in the laboratories in Colorado. I would also like to thank Benny Guralnik for supervising the project and for Cathelijne Stoof and Jakob Wallinga for taking over after Benny Guralnik's departure from the University. I am grateful to everyone who has believed in me and encouraged me to go on. Last but not least, I would like to thank my family for their support and allowing me to pursue a scientific career.

Thank you for taking the time to read this thesis. I hope it will be an informative and enjoyable experience for you.

Line Schug

TABLE OF CONTENTS

TABLE OF FIGURES

TABLE OF TABLES

TABLE OF INFO BOXES

1 INTRODUCTION

1.1 BACKGROUND

Amongst the ~200 Martian meteorites documented so far, NWA 7034 is considered unique thanks to its unusual chemical and mineral composition, and high water content (Agee *et al.,* 2013). Its mineral and isotopic composition is such that it cannot be grouped together with the major Martian meteorite groups: shergottites, nakhlites, chassignites. Agee *et al.,* (2013) identified it as a regolith breccia, composed of multiple pieces of the Martian crust, fused together by a poorly sorted impact melt matrix. It is believed to be a polymict, a breccia containing multiple generations of brecciation (Wahl, 1952; Santos *et al.,* 2015). This allows an insight into the formation history of the Martian crust.

Atmospheric inclusions in apatite were used to determine the planetary origin of NWA 7034. These provide a unique compositional fingerprint that can be compared to a well-documented database (Agee *et al.,* 2013). Additionally, oxygen isotopic composition, and Fe/Mn ratios in pyroxenes were measured and compared, confirming a Martian origin (Figure 1).

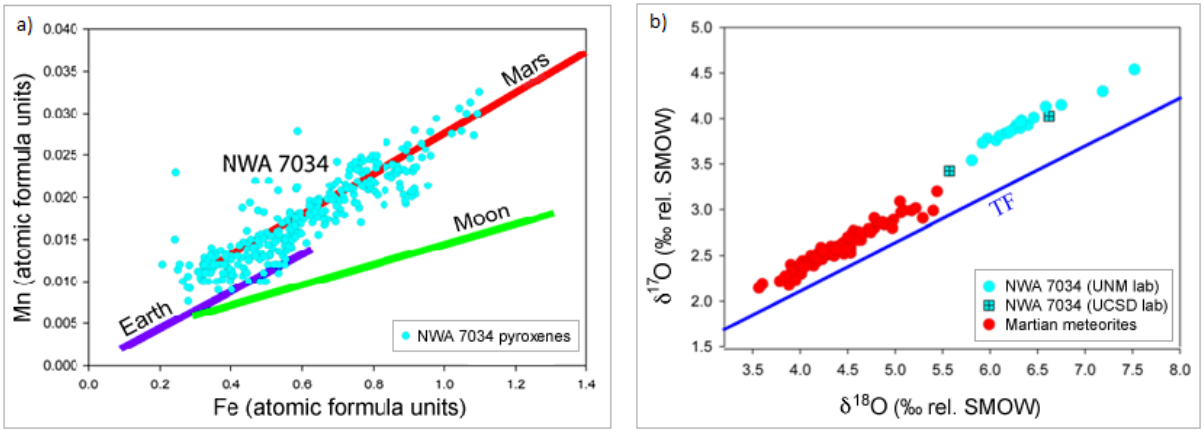

Figure 1: a) Comparison of Fe/Mn ratios in pyroxenes in NWA 7034 plotted with pyroxene samples from Mars, Earth and Moon. b) Comparison of oxygen isotope compositions of NWA 7034 and other Martian meteorites. Both taken from Agee et al., 2013.

Whole-rock Rb-Sr geochronology yielded a five-point isochron age of 2.089 ± 0.081 Ga (Agee *et al.,* 2013); this is believed to be the time at which the breccia accreted. This formation age would make it significantly younger than its Martian relatives (except its paired meteorite NWA 7553). However, this is not the crystallisation age of most of the major components of the meteorite (Bellucci *et al.,* 2016). NWA 7034 is a breccia, meaning it is composed of clasts of rock intermixed with a matrix (Norton, 1917). Textural

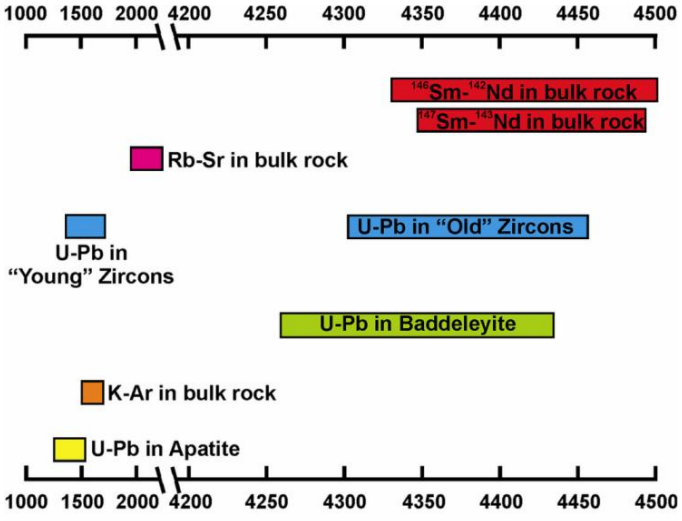

Figure 2: Summary of dating techniques applied to samples of NWA 7034 and their respective results. Taken from Nyquist et al, 2016.

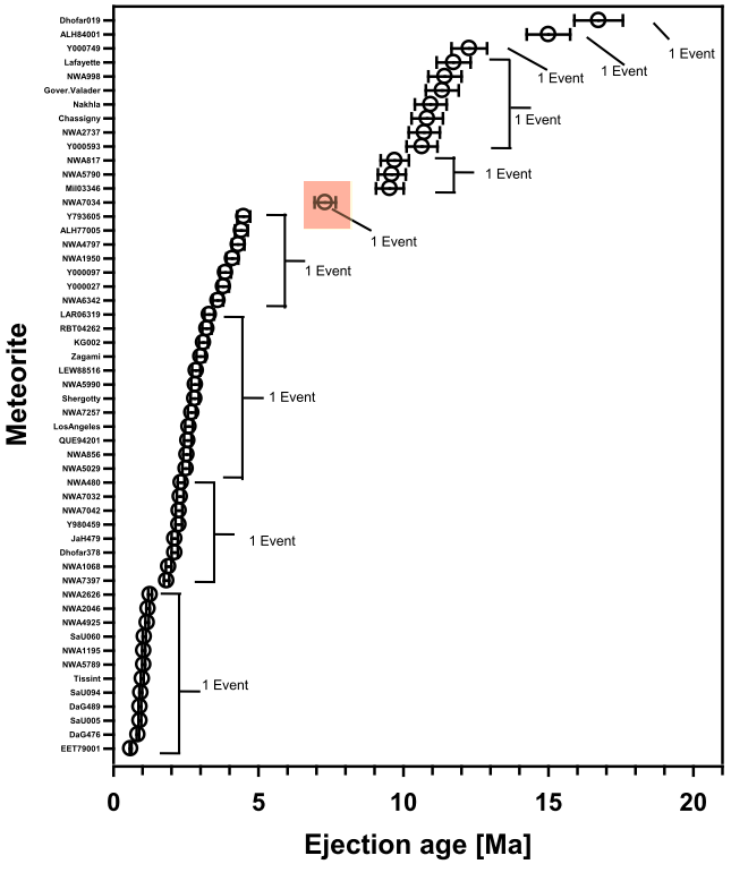

Figure 3: Ten proposed ejection events of Martian Meteorites (Mahajan, 2015), where NWA 7034 (red square) is proposed to have been ejected as part of a distinct event.

evidence suggests that the older generation melt was formed by a previous impact (Goderis *et al.,* 2016). Therefore, it is to be expected that there will be a large spread of mineral ages.

For instance, U-Pb dating of baddeleyite and zircons have revealed that some of these mineral phases (if not the majority) crystallised at a much earlier time, which coincides with crustal formation on Mars and Earth (~4.4 Ga, Agee *et al.,* 2013) (Figure 2) and even ~4.7 Ga, McCubbin *et al.*, 2016). These minerals require very high temperatures for their U-Pb ratios to be reset (>1000 °C), which explains how they are still intact despite the material in which they are found being polycyclic.

Ejection age was determined from cosmic radiation exposure ages, based on noble gas isotope ratios. Cartwright *et al.,* (2014) calculated three ages: 5.1 Ma, 11.4 Ma (corrected to 9.0 Ma) and 5.4 Ma, and expressed confidence in the younger ejection dates. Mahajan (2015) averaged these, proposing an ejection age of 7.3 Ma, making NWA 7034 the only meteorite to be transported to Earth from Mars in a ~5 Ma period of low activity (Figure 3). Meteorites with matching ejection ages typically have the same chemical-petrologic classififcation, indicating singular ejection events from one locality (McSween, 2015). Based on its noble gas composition, NWA 7034 likely had a distinct ejection event. However, it is possible NWA 7034 launched from the same ejection event as the others, but from a location of distinct composition. This supports the hypothesis that NWA 7034 is enriched in rare earth elements to the point where it must have originated from a geochemically enriched zone, which are typically limited to small geographic areas (Agee *et al.*, 2013; Liu *et al.*, 2016).

Dating of NWA 7034 components resulted in a maximum age of ~4.4 Ga and ~4.7 Ga, based on Sm–Nd, U-Pb in phosphates, zircons and baddeleyite grains found in igneous clasts (Agee *et al.,* 2013; Humayun *et al.,* 2013; McCubbin *et al.*, 2016). These are expected to be analogous with crustal building processes. Clasts show evidence of degassing of water and CO_2, and are alkali rich, implying similar formation conditions and geochemistry to early Earth (Yin *et al.,* 2014). In fact, evidence of a hydrological cycle and abundant weathering suggest that Mars might have once supported life (Mojzsis and Arrhenius, 1997).

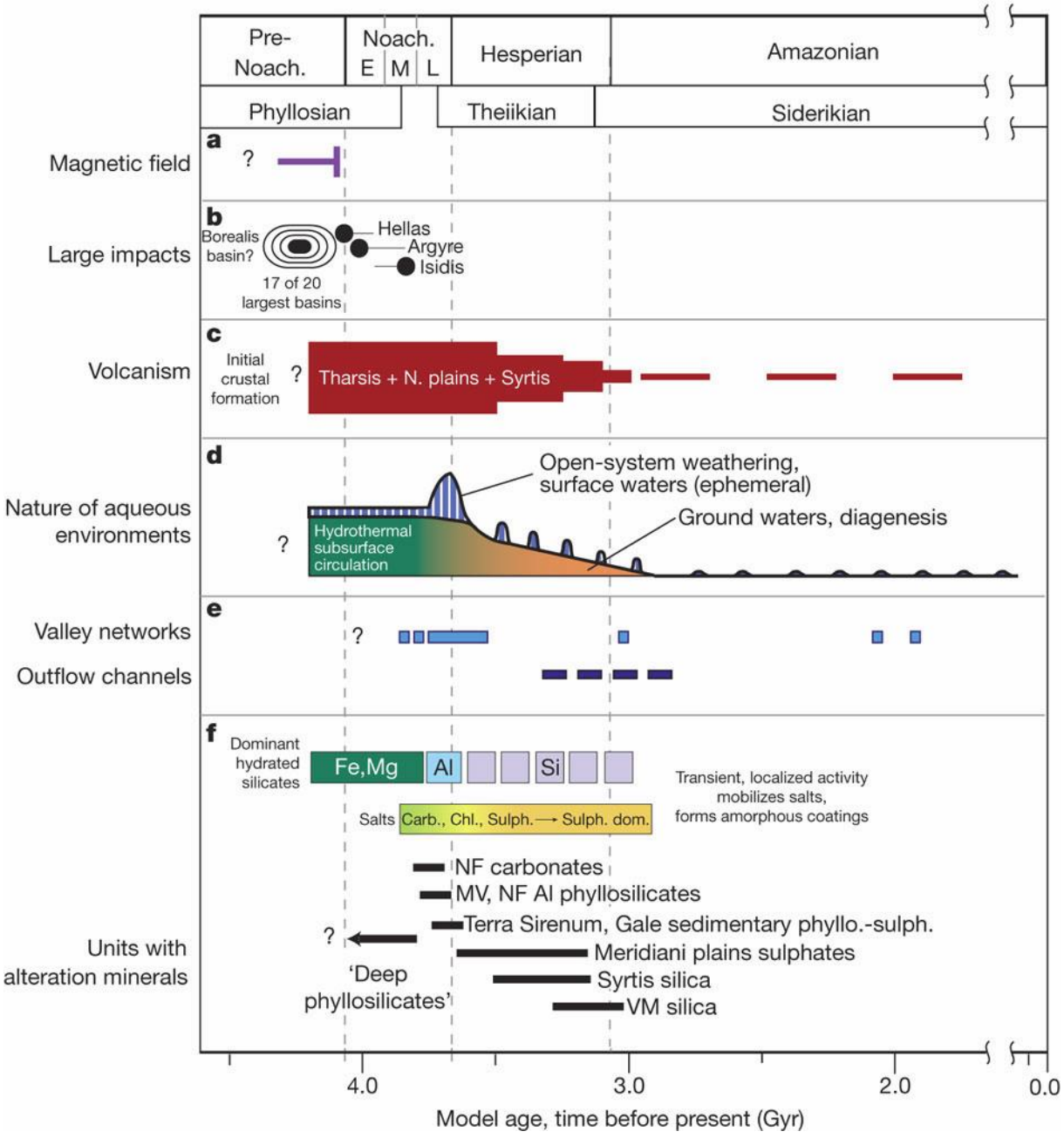

Figure 4: Timeline of major processes in Martian history taken from Ehlmann et al., (2011). The environment in which NWA 7034 is believed to have been accreted (~2.1 Ga) was rich in siderophiles, weathering was dominated by oxidation and some water was available (Ehlmann et al., 2011).

Brecciation is believed to have occurred <2.0 Ga (~2.1 Ga based on disturbances in Rb-Sr, Agee *et al.,* 2013). This time period had abundant siderophiles, weathering was dominated by oxidation and some water was available (Figure 4; Ehlmann *et al.,* 2011). Several thermal events followed, such as resetting of K–Ar at ~1.6 Ga, and ~170 Ma for U–Th/He (Cartwright *et al.,* 2014); U-Pb of phosphates at about 1.35–1.5 Ga, and zircons at ~1.7 Ga (Humayun, Nemchin, Zanda, Hewins, Grange, Kennedy, J. P. Lorand, *et al.*, 2013). However, the exact timing of breccia formation is still being debated, with some scientists placing it later, at ~1.44 Ga (Yin *et al.,* 2014), making it possible to have originated from Mars' relatively young Northern Hemisphere. These dates place breccia formation in the early to mid-Amazonian, a period believed to have had abundant lava flows, glacial-interglacial cycles and some water, however post-dating the most extensive water coverage and volcanism on Mars (Figure 4; Ehlmann *et al.,* 2011).

1.2 What makes NWA 7034 special?

NWA 7034 it is the most hydrated Martian meteorite found yet, with a water content (~6000 ppm), largely preserved in phyllosilicates and phosphates an order of magnitude larger than that of any other of its clan (Muttik *et al.,* 2014). However, it is unknown what caused the hydration or when it took place. Light and heavy hydrogen isotope ratios found in apatite crystals have shown that the water involved in the reaction was enriched in Deuterium (D), indicative of surface/groundwater (the lighter hydrogen isotope escaped into space) as opposed to "juvenile" magmatic water (Greenwood *et al.,* 2008). When step-heating a sample of NWA 7034, the majority of the H_2O contained within NWA 7034 was released at low temperature (62% prior to reaching 300°C), which implies that the water in NWA 7034 is primarily contained within secondary mineral phases (Muttik *et al.,* 2014). Hydrogen (H) isotopic compositions in apatites of NWA 7034 can be broken down into two δD, both significantly lighter (-100 and +300‰, Agee *et al.,* 2013) than what is typical for the Martian atmosphere and Martian meteorites (i.e. >2500%, Greenwood *et al.,* 2008). The two degassing events support the theory that NWA 7034 experienced multiple impacts (Humayun *et al.*, 2013). Muttik *et al.,* (2014) suggested terrestrial contamination but pointed out that there is evidence for the existence of a light isotopic reservoir on Mars.

Another quality that makes NWA 7034 special is that it is a breccia. This allows studying clasts of different geographic and temporal origins, giving a broad insight into Mars 'crustal history. The bulk rock is heavily enriched in light rare earth elements (LREE), resembling KREEP-rich lunar rocks. "KREEP" stands for potassium (K), phosphorus (P) and rare earth elements (REE) (Hubbard *et al.,* 1971). This suggests geochemical enrichment of the crust early in Martian history (Yin *et al.,* 2014). The bulk composition of NWA 7034 is close to the composition of rocks and soils found at the Gusev crater landing site (Figure 5), and with estimates of the average Martian surface composition measured by the Mars Odyssey Orbiter (Agee *et al.,* 2013; McSween *et al.,* 2009). This would imply that at least parts of NWA 7034 originate from the Martian surface or close to the surface, meaning it can provide us insight into the regolith interaction with the hydrosphere, and weathering and -alteration processes occurring there (Muttik *et al.,* 2014). If the clasts really did originate from melts of different generations, it would be possible to put temporal constraints on these.

Furthermore, a resetting of Rb-Sr ratios, as seen at ~2.1 Ga, can be caused either by partial melting and/or hydrothermal alteration (Evans et al, 1995), but so far it is uncertain how much influence each of those processes had on the Sr-Rb ratio of NWA 7034. There is evidence for secondary and possibly tertiary brecciation at 1.44 Ga and 170 Ma (Agee *et al.,* 2013; Cartwright *et al.,* 2014).

Hydrothermal alteration of minerals within NWA 7034 may have occurred, most evidently shown by the high abundance of iron rich oxides, such as magnetite, maghematite, of various sizes throughout the fine-grained basaltic groundmass (Agee *et al.,* 2013; Santos *et al.,* 2015). However, it is unclear whether this secondary alteration occurred prior to impact in the Martian crust or due to the impact that excavated it and launched the sample to Earth, possibly involving a water rich impactor (Lorand *et al.,* 2015; McCubbin *et al.,* 2016). It is unlikely that this alteration took place on Earth, as these iron oxides are not only found exclusively along cracks or clast boundaries. On Mars, these oxides make up the red dust that covers the surface (Bandfield, 2002). On Earth these phases are commonly found in weathered rocks and soils, implying there might have been more advanced soil development on Mars than what is popularly believed (Schwertmann, 1958; Ehlmann *et al.,* 2011).

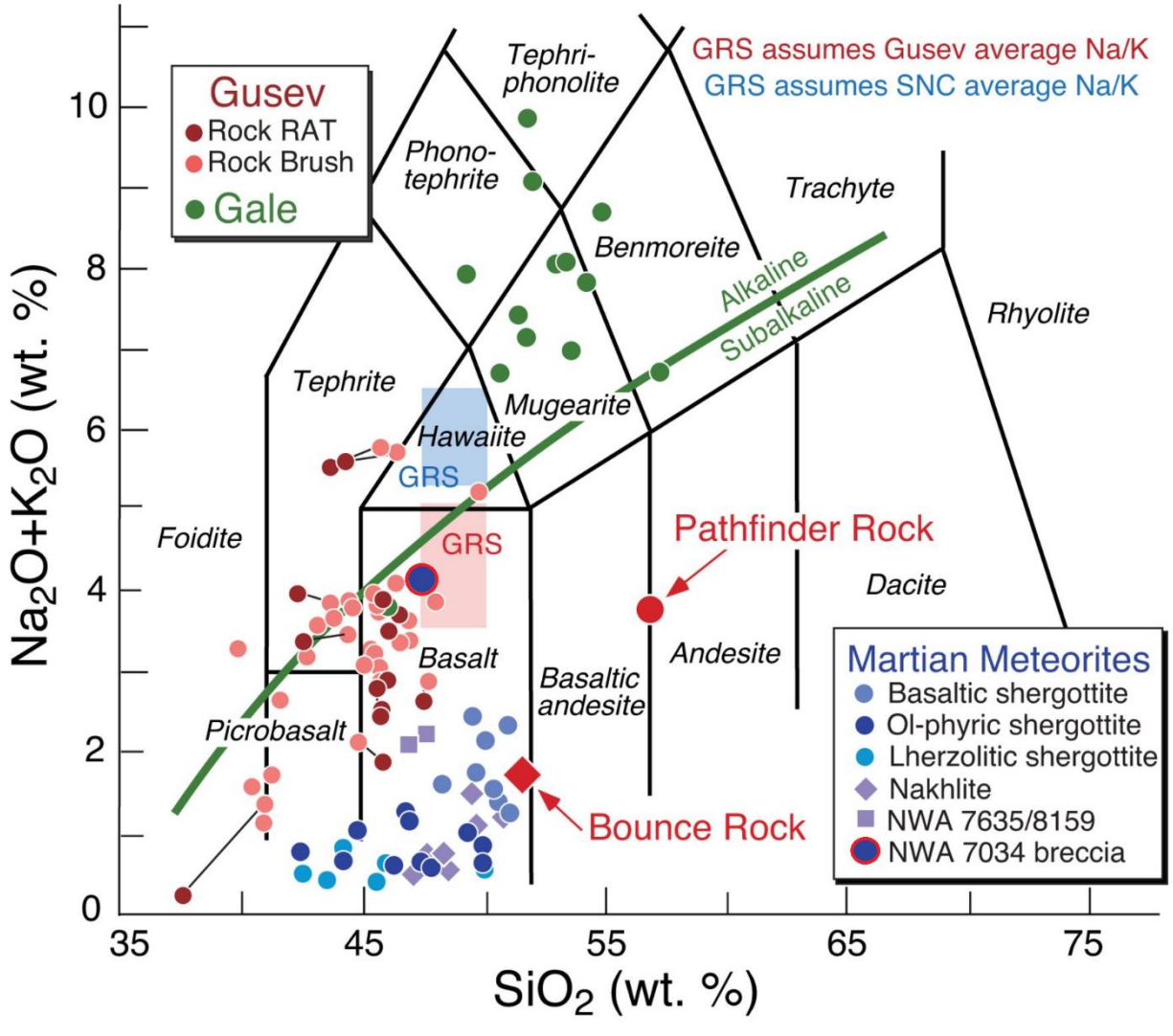

Figure 5: Taken from McSween (2015). Volcanic rock classification scheme, contrasting the weight percent silicon- and alkali oxides of NWA 7034 (large blue dot with red outline, mean bulk value, determined by 225 electron microprobe analyses of the fine-grained groundmass) (Agee et al., 2013) with other known Martian ratios: Green dots represent compositions of rocks and soils at Gale Crater, red dots at Gusev Crater (measured using an Alpha Particle X-ray Spectrometer (Gellert et al., 2006; Ming et al., 2008). The blue and red squares represents the composition of the average Martian crust (measured by the gamma ray spectrometer on the Mars Odyssey orbiter (Boynton et al., 2007)). The blue and purple dots represent meteorites (Agee et al., 2013.

1.3 RESEARCH MOTIVATION

While many of the special clasts in NWA 7034 have been identified, and compositions studied, we do not know the sequence of breccia formation and subsequent thermal and chemical alterations, and what minerals were affected by which processes. The aim of this study is to create an inventory of minerals and clast types to make a statement about the formation conditions and timing that led to this assembly. This data will then be used to make further predictions concerning the make-up of NWA 7034 and its compositional variability and the timing of compositional changes in the Martian crust. It will then serve as the basis for isotope work aiming to determine whether phases that were formed at different times will preserve different isotopic oxygen signatures.

By studying the texture of clasts and groundmass, and by determining phase compositions in minerals, we can learn more about the nature of the Martian surface that was impacted to form the. Additionally, microstructures and mineral superposition indicate whether alteration preserved in the meteorite is a result of its formation through impact, or alteration that affect components on or below the Martian surface (Bowen, 1912; Leroux, 2001; Leroux *et al.,* 2016).

NWA 7034 has the potential to allow us an insight in both the past and the future of Mars, to one day make predictions about our own planet's future, such as what minerals could form if water were no longer available and physical weathering would dominate over chemical. By assuming NWA 7034 provides an accurate and typical representation of Martian crust, knowing its composition and formation history may add to the existing data base of possible human applications of Martian rocks, such as mineral and material resources for construction, energy and life sustaining applications (Zubrin and Baker, 1991; Boston *et al.,* 2003; Zubrin, 2015).

1.4 RESEARCH QUESTIONS

This study aims to answer the following research questions:

I. Does the mineral and rock assemblage of NWA 7034 support the theory that it was aggregated and ejected near Gale and Gusev crater (near boundary of highlands and lowlands)?
II. Does the timeline of petrogenesis for NWA 7034 follows the one proposed in Table 1?

A hypothetical timeline of petrogenesis (rock forming events) was proposed, based on existing literature and first impressions looking at mount photographs. To support this history of petrogenesis, mineral phases and -assemblages, commonly associated with the pressure and temperature conditions of the events listed in Table 1, were looked for. Additionally, mineral cross cutting and superposition were taken into consideration, as they preserve the sequence of mineral growth and -weathering (Bowen, 1912). Based on these, conclusions were drawn about circumstances and conditions that led to the genesis of the minerals inside of the meteorite and on the surface of Mars.

Table 1: Proposed timeline of rock-forming events for NWA 7034.

Period	*Time*	*Event*	*Evidence (literature)*	*Kinetic rate*	*Temperature*	*Pressure*
Pre-Noachian	~4.4 Ga	formation of gabbronorite	Whole rock composition of NWA 7034 established it is mafic-ultramafic (trachybasalt) (Agee *et al.*, 2013), U-Th and Sm-Nd ages of zircons, phosphates, baddeleyite (Humayun *et al.,* 2013)	high	high	medium to low
Noachian and Hesperian	long period of non-disturbance		excess Xe^{136} (Cartwright *et al.*, 2014)	low	low	low
Amazonian	~2.1 Ga	Impact (I) into gabbronorite formation	Only high T phases survived impact	high	high	high
	~2.1 Ga	Breccia formation (I)	porphyritic and brecciated texture, atmospheric inclusions, Rb-Sr ages (Agee *et al.,* 2013)	low	high – low	low
	uncertain	Intrusion of meteoric water and weathering (I)	abundant water present on mars; high T/P phases are not stable at surface conditions and slowly break down into stable phases (Bowen reaction series)	low	low	low
	~1.56 Ga	metamorphic resetting event	K-Ar age (Cartwright *et al.,* 2014)	high	medium	high
	~1.44 Ga	breccia formation (II)	zircon and baddeleyite ages (Humayun *et al.,* 2013)	high	high	high
	~1.35 Ga	metamorphic resetting event	1.35 - 1.5 Ga phosphate ages (Humayun *et al.,* 2013; Yin *et al.,* 2014)	high	High	high
	~170 Ma	resetting event	U-Th/He age of atmospheric inclusions (Cartwright *et al.,* 2014)	high	High	high
	~7.3 Ma	Ejection from Mars	known to be Martian meteorite; Mars has low escape velocity, so no high P/T required; Cosmic Ray exposure (Cartwright *et al.,* 2014)	low	low	low
Neogene	~7.3 Ma	Impact (II) on Earth	reaction rind; found in desert	medium (T too low to have effect past reaction rind)	medium (too low to have effect past reaction rind)	medium (lower impact velocity due to lower mass)
	~7.3 Ma to present	Weathering (II)		low	low	low

2 METHODS

This section introduces the approach taken to answer the research questions. Firstly, scanning electron microscopy, backscatter electron imagery, cathodoluminescence, x-ray spot analysis, and Qemscan software were used to describe mineralogy and petrology, obtain geochemical composition, and deduce formation environments. Additionally, the sample preparation process was described. Lastly, the assumptions necessary to follow the approach were listed, as well as the process for assessing validity and significance of results. Table 2 explains the abbreviations used throughout the text. Table 3 lists the mineral phases and components, and the empirical formulas used to define them.

Table 2: Abbreviations used and their respective meanings.

Group	*Abbreviation*	*Meaning*
Instrument	(FE-)SEM	(Field Emission) Scanning Electron Microscope
	EPMA	Electron Probe Micro-Analyzer
	BSE	Backscatter Electron
	EDS	Energy Dispersive Spectrum
	SED	Secondary Electron Detector
Ion	K	Potassium
	Ca	Calcium
	Na	Sodium
	Mg	Magnesium
	Fe	Iron
	Cr	Chromium
	Al	Aluminium
	Ti	Titanium
	Mn	Manganese
	Si	Silicone
	H	Hydrogen
	Th	Thorium
	Sm	Samarium
	Nb	Niobium
	Sr	Strontium
	Rb	Rubidium
	U	Uranium
Clast labels	ipc	Ilmenite-plagioclase clast
	sph	Spherule
	pc	Phosphate (apatite) clast

Table 3: Mineral abbreviations used and their respective meanings. The empirical formula used to define phase- and phase components were derived from the International Mineralogical Association (Pasero, 2018).

Group	*Abbreviation*	*Meaning*	*Definition*
Mineral phase	Pl/plag	Plagioclase (albite anorthite series)	$NaAlSi_3O_8$-$CaAl_2Si_2O_8$
	Alk	Alkali feldspar (albite orthoclase series)	$KAlSi_3O_8$-$NaAlSi_3O_8$-$CaAl_2Si_2O_8$
	Pyx/px	Pyroxene	$Ca(Mg, Fe)Si_2O_6$-$(Mg, Fe)Si_2O_6$
	Cpx	Clinopyroxene	$Ca_{5\text{-}50\%}(Mg, Fe)Si_2O_6$
	Opx	Orthopyroxene	$Ca_{0\text{-}5\%}(Mg, Fe)Si_2O_6$
	Apt	Apatite	$Ca_5(PO_4)_3(Cl, F, OH)$
	Il	Ilmenite	$FeTiO_3$
	Pyr	Pyrrhotite	Fe_7S_8
Phase component		Augite (clinopyroxene)	$Ca_{20\text{-}45\%}(Mg, Fe)Si_2O_6$
	Di	Diopside (clinopyroxene)	$(Ca_{50\text{-}5\%},Mg_{50\text{-}100\%},Fe_{0\text{-}50\%})Si_2O_6$
	En	Enstatite (orthopyroxene)	$(Ca_{5\text{-}0\%},Mg_{50\text{-}100\%}, Fe_{0\text{-}50\%})_2Si_2O_6$
	Fs	Ferrosilite (orthopyroxene)	$(Ca_{5\text{-}0\%},Fe_{50\text{-}100\%},Mg_{0\text{-}50\%})_2Si_2O_6$
	Hd	Hedenburgite (clinopyroxene)	$(Ca_{55\text{-}5\%},Fe_{50\text{-}100\%},Mg_{0\text{-}5\%})Si_2O_6$
	Pig	Pigeonite (clinopyroxene)	$(Ca_{5\text{-}20\%}, Mg, Fe)_2Si_2O_6$
	Ab	Albite (endmember) alkali feldspar plagioclase	$(Na_{90\text{-}100\%}, Ca, K)AlSi_3O_8$ $(Na_{100\text{-}50\%}, K_{0\text{-}50\%},Ca)AlSi_3O_8$ $(Na_{100\text{-}50\%}, Ca_{0\text{-}50\%})AlSi_3O_8$
	An	Anorthite (endmember) plagioclase	$(Ca_{90\text{-}100\%})Al_2Si_2O_8$ $(Ca_{90\text{-}100\%},Na_{0\text{-}10\%})Al_2Si_2O_8$
		Andesine (plagioclase)	$(Ca_{70\text{-}50\%},Na_{50\text{-}30\%})Al_2Si_2O_8$
		Anorthoclase (alkali feldspar)	$(Na_{70\text{-}90\%},K_{30\text{-}10\%})Al_2Si_2O_8$
		Bytownite (plagioclase)	$(Na_{30\text{-}10\%},Ca_{70\text{-}90\%})Al_2Si_2O_8$
		Labradorite (plagioclase)	$(Na_{50\text{-}30\%},Ca_{50\text{-}70\%})Al_2Si_2O_8$
		Oligoclase (plagioclase)	$(Na_{70\text{-}90\%},Ca_{30\text{-}10\%})Al_2Si_2O_8$
	Or	Orthoclase (endmember) alkali feldspar	$(K_{50\text{-}100\%},Na_{30\text{-}0\%},)AlSi_3O_8$ $(K_{70\text{-}100\%},Na_{50\text{-}0\%})AlSi_3O_8$

2.1 SAMPLE PREPARATION

A total of 11 thin section mounts of NWA 7034, sized approximately 5000 x 6000 µm, were used to varying extend in this study. All three instruments to be utilized in this study allowed for the sample to be mounted in a 1 inch circular epoxy mould. Prior to any analysis the samples have been prepared by another researcher at the University of Colorado, based on the recommended process for SEM mount preparation suggested by Goldstein *et al.,* (1981). Mounts were prepared by pressing thin section cuts down onto conducting carbon tape, leaving as little space as possible for the epoxy to intrude. A 1 inch circular mould was placed around the sample and epoxy was added. After the epoxy had fully hardened, the mount surfaces were polished down to about 1 µm using a diamond saw. Mounts will hereon be referred to by their names: A, B, D, Janis 1, Janis 2, 534, 362, 372, 458-1, 458-2, 458-3. Conductive coating of the sample with carbon tape and -oil, to create a conductive bridge, was required prior to any analysis via Scanning Electron Microscope (SEM) or Electron Microprobe Analyzer (EPMA). This was done to reduce electrical recharging of susceptible iron oxides and iron-titanium oxides, which are highly abundant in NWA 7034.

The sample mounts are scattered with small (typically <10 µm) iron oxides. These exhibited variable magnetic properties strong enough to induce a magnetic field that deflected an electron beam. The beam was not consistently deflected in one direction, meaning the iron oxides had magnetic fields of different orientations. As a result, the charging effect was too severe to allow for reliable spectral analysis via EPMA. This was mitigated by demagnetizing the samples for 12 hours using a demagnetizer prior to analysis.

2.2 INSTRUMENTAL ANALYSIS

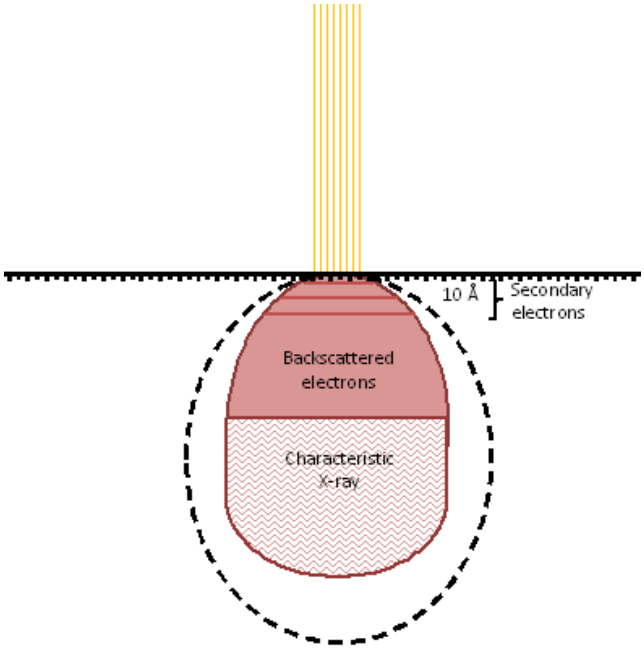

Figure 6: Illustration showing the locations within the surface of the sample site where the different signals originate from when excited by the electron beam (yellow). The dotted area represents the excitation volume. Note how the secondary electrons are generated in the upper 10 Å of the site.

A SEM can be used for different analyses based on the detectors attached (Smith and Oatley, 1955). For this project, two SEMs, each with different functional strengths, were used. Both machines are located at the Geology Laboratory of the School of Mines in Golden, Colorado. Secondary electrons, backscattered electrons and characteristic x-rays were used to confirm mineral identity.

The area within the sample surface that is stimulated by the beam is called the excitation volume. Secondary electrons are deflected from the first 10 Å of the sample surface, backscattered electrons from a little deeper. The deepest signal to be used for this analysis stemmed from the characteristic x-rays (Figure 6).

Secondary electrons give an idea of the surface topography. Backscattered electrons provide the atomic number. When an atom is excited, electrons shift in between shells, while they are moving, they release energy in the form of an x-ray, which can be detected. From the wavelength, frequency and the energy released that is specific to an element, one can obtain the proportions of an element within a mineral. These are output in an energy dispersive spectrum (Zworykin and Ramberg, 1941).

For all spot analyses (including x-ray), analytical errors can arise when the excitation volume exceeds the grainsize or when the sample spot is located on a boundary between two minerals. In this situation the detectors will still yield the full chemical composition of the sampled area, however minerals can be misidentified as the composition of two separate mineral phases blurred into one (Figure 7; Bohor and Hughes, 1971). This effect was mitigated by avoiding placing sampling positions close to grain boundaries and cracks. Measurements were repeated for low elemental totals (~<95%).

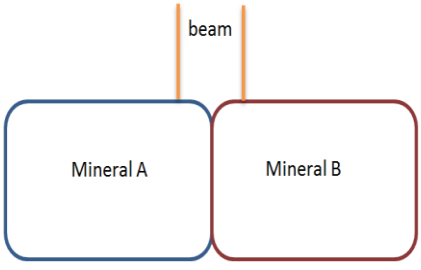

Figure 7: Diagram illustrating how a mineral can be misidentified when the beam is fixated on a spot too close to the boundary of another mineral phase.

Backscattered electron (BSE) images of NWA 7034 were collected from ten mounts using the Field Emission (FE-) SEM of the JEOL 8200 EPMA at the Colorado School of Mines, equipped with a Backscatter Electron (BSE), Energy Dispersive Spectrum (EDS), and Secondary Electron (SED) detector (Figure 9). The advantage of this machine is that it utilises a narrow beam (nanometres in size compared to 1 µm for the Qemscan), allowing for spectral analysis at higher resolution (Smith and Oatley, 1955; Bohor and Hughes, 1971).

Quantitative x-ray spot analysis allows for precise identification of mineral phase components by determining stoichiometry using the x-ray and EDS detectors of the EPMA (Castaing, 1960). This technique can distinguish between polymorphs, minerals that contain the same chemical composition at different stoichiometric proportions, e.g. hematite and magnetite; and minerals containing atoms, with masses too low to be picked up by the FE-SEM (e.g. minerals containing hydrogen). The EPMA is optimized for spot analysis and yields a better quantitative result than the FE-SEM. However, minor damage (burning) can occur with prolonged, high intensity exposure. For this project, the JEOL JXA 8230 electron probe microanalyzer, located at the Geology Laboratories of the University of Colorado, Boulder, was used to determine mineral components of pyroxenes, plagioclases. Si, Al, Na, Mg, Ca, Ti, Cr, K, Fe, Mn, O were computed for each selected spot, using an acceleration voltage of 15 kV, electron beam current of 20 nA, and varied beam sizes based on mineral identification (0 µm for pyroxene and metal oxides, 5 µm for plagioclase. Centre and the rim of the grain were probed to investigate within-grain zoning (Figure 8). By sampling the rim, mantle and core of a clast one can infer if the composition changed as the clast was forming due to a maturing melt. This would imply slower cooling/ more rapidly maturing melt. Atomic percentages were derived from counts based on the formulaic number of oxygen (e.g. 8 for plagioclase, 6 for pyroxene) and for unknowns, using the number of oxygens that yielded relative proportions that best aligned with the count data.

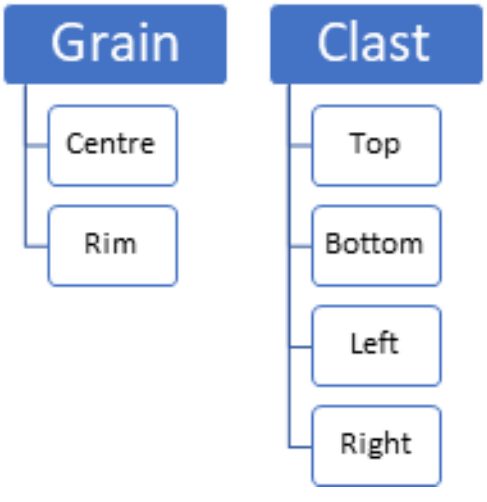

Figure 8: Sampling strategy for x-ray spot analysis.

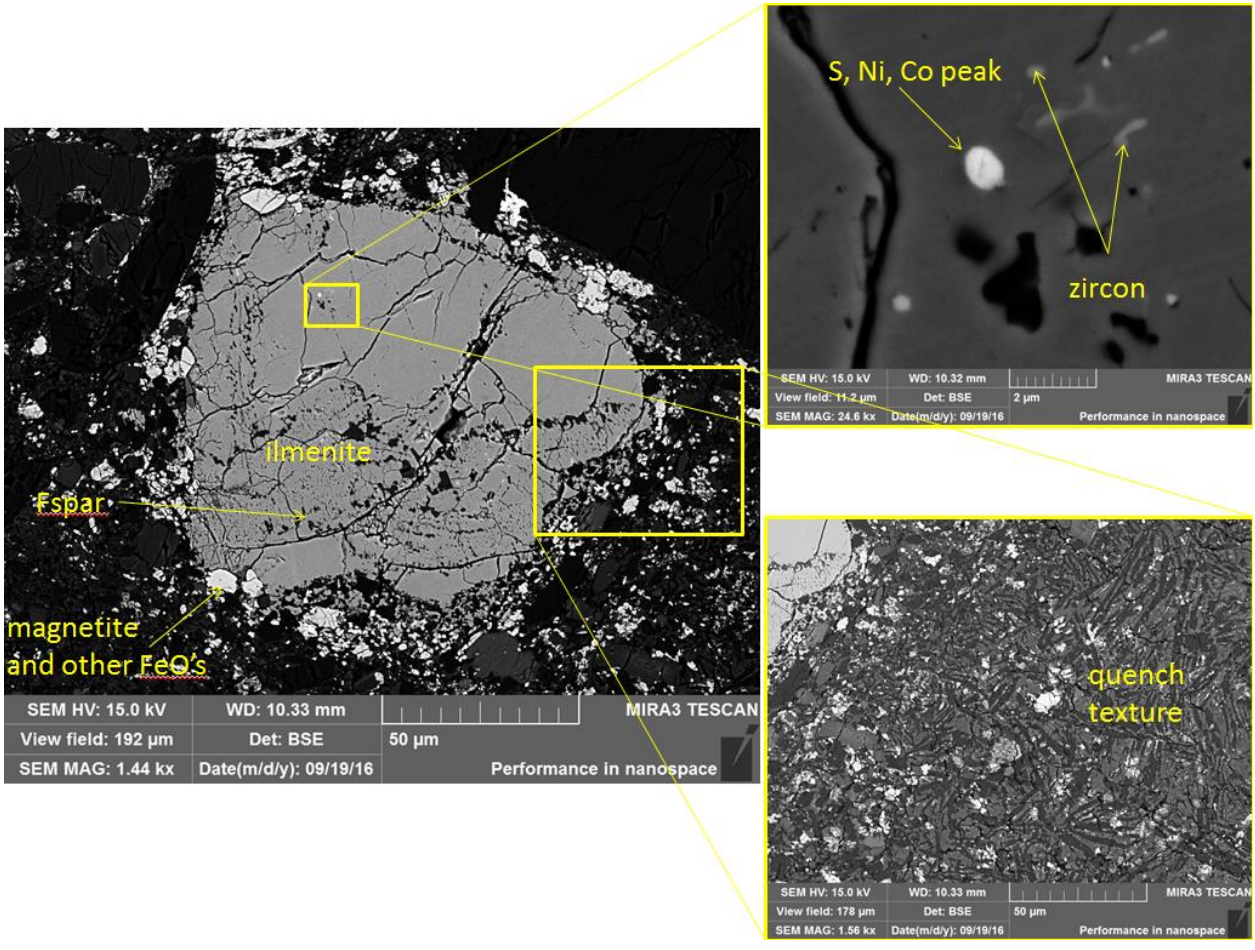

Figure 9: Example output of the FE-SEM. Brightness is indicative of atomic number and is used to distinguish between minerals of different composition and identify alteration. Note the resolution. The narrow beam diameter allows the identification of zircons sized <1 µm.

Qemscan stands for Quantitative Evaluation of Materials by Scanning Electron Microscopy. It is a special SEM, equipped with a BSE detector and four EDS detectors (Pirrie *et al.,* 2002; Gottlieb *et al.,* 2000). Qemscan combines the intensity of backscattered electron signal with energy spectra generated from characteristic x-ray intensities to output customized mineral maps (Figure 10). The maps are easily legible and greatly simplify the mineral identification process. Furthermore, the four EDS detectors allow for fast analysis, thanks to short computation time. Qemscan assigns a minerals identification to an area of set size, based on the relative elemental abundance it records by spot sampling. These are then combined into a map. The map resolution corresponds to the beam size, in this case 1 micron.

Maps were created for 11 mounts. Using Adobe photoshop, separate maps were created for all major minerals. Relative abundance of minerals within a clast and subsequently rock types could be determined by computing the pixels each mineral occupied within a select area. The same technique was used to determine clast size and how much of the mount area select clast types occupy.

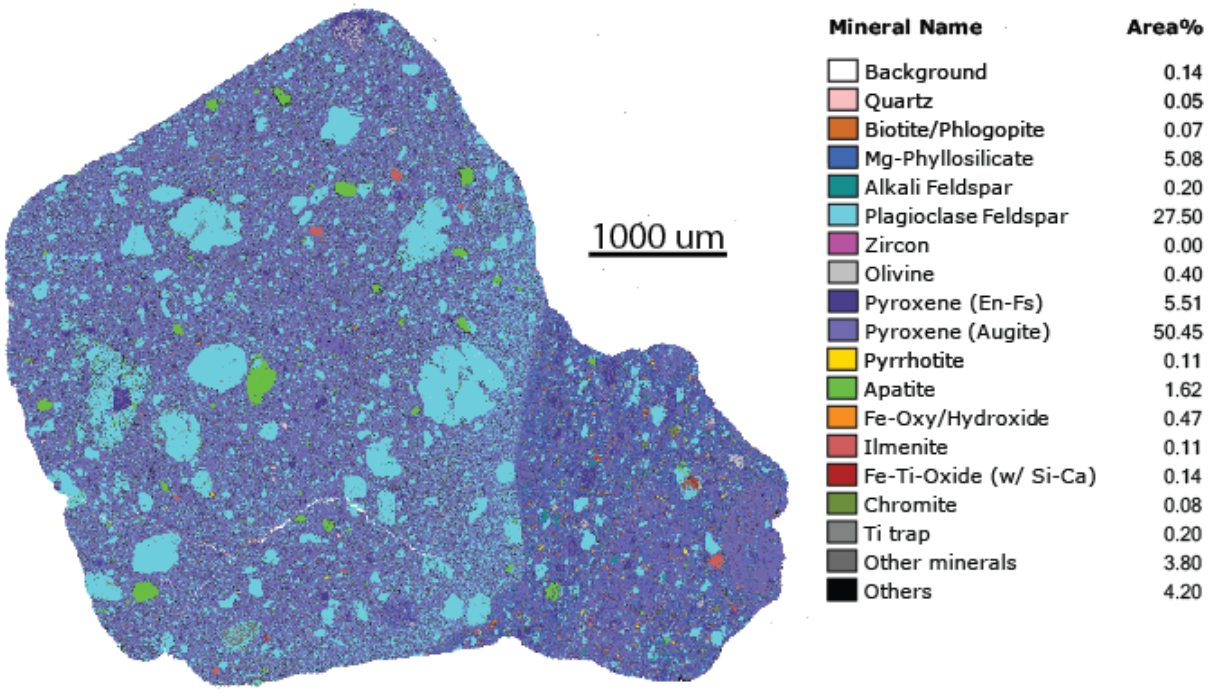

Figure 10: Example output of automated mapping in Qemscan, using pre-assigned compositional standards to group minerals.

2.3 INTERPRETATION OF RESULTS

To interpret the results, a two-step approach was conducted. First mineralogy and petrology were described in detail, then the formation environment was deduced based on existing knowledge of petrology and Martian geology. Mineral phases and rock types were classified based on composition, texture, size, identity, co-occurrence and abundance of clasts and minerals contained within NWA 7034, including feldspar, pyroxene, ilmenite, apatite, pyrrhotite, zircon and chromite. This was done by creating maps of clast types and minerals for 11 mounts, based on characteristic x-ray signals and back scatter electron imaging (BSE). A preliminary identification of mineral phases and -components was done using the Qemscan at School of Mines.

Mineral phase components were identified based on their molar composition. This allowed, for example, the type of feldspar to be identified (i.e. sanidine, labradorite, etc.). These helped identify the type of alteration and the cause behind zoning. The chemical composition was obtained by quantitative x-ray spot analysis on an Electron Probe Micro-Analyzer (EPMA) at the University of Colorado.

The aim was to define formation and post formation conditions (such as temperature) based on phase composition of melt. Cooling models were used to estimate crystallization temperature and cooling rate for plagioclase (Bowen, 1913; Lindsley and Fuhrman, 1988), alkali feldspar (Yoder *et al.,* 1957; Morse, 1970), and pyroxene (Poldervaart and Hess, 1951; Lindsley and Andersen, 1983). Crustal age, temporal and geographic proximity to other impacts, impact density, burial depth, atmospheric thickness factor into crustal pressure and -temperature (Abramov and Mojzsis, 2016). These factors would need to be considered for each clast and data was not available, therefore, a pressure of 1 atm was assumed as a standard to constrict formation temperature. By identifying the composition and working backwards, it was possible to infer chemical reactions taking place in the immediate surroundings. To determine

whether a mineral crystallised from the impact melt or had been emplaced prior, it was helpful to look at crystal size, growth pattern and zoning. Using backscatter electron microscope imaging and x-ray maps it was possible to determine if compositional zoning was present (Figure 11).

Relative time sequences of mineral growth and alteration were inferred from textural relationships between minerals in clasts and matrix domains by applying the principles of superposition and cross cutting (Steno, 1669; Bowen, 1912). Intrusive structures, such as fractures that cross-cut multiple levels of brecciated rock, or veins in which atypical phases grew, were regarded as evidence of an outside event, such as remnants of shock metamorphism or hydrothermal activity. By looking at what levels of brecciated rock they crosscut, a timing of these events could be estimated. The extent to which a mineral was consumed by melt, whether minerals were able to recrystallize in fractures, whether a mineral was a rounded or angular were used to deduce which alteration processes might have taken place prior to impact and which might have occurred after, and how they were limited by temperature.

By considering what components were stable, it could be inferred what composition and temperature the melt might have had (Kirkpatrick, 1975). For simplicity and due to a lack of availability, it was assumed that phase composition, temperature- and pressure conditions for minerals formed on Earth were similar enough to be applied for minerals formed on Mars.

Growth patterns (e.g. nucleation vs lath, radial growth etc.) gave an idea of cooling rate and hence the process that had led to that characteristic cooling rate, e.g. spherules with radial and lath growth indicative of melt pockets being projected and rapidly cooling as they come in contact with air or other cooler material, such as cooled regolith (i.e. Dowty, 1976; Shore and Fowler, 1996). Zoning patterns, representing lateral changes in composition, were recorded in ternary diagrams and used to identify a temperature, pressure or compositional change.

Grain size provided information on growth rate, such as whether it was continuous, disrupted, recrystallised or compositionally limited. For example, a granoblastic clast with equigranular grains likely formed in a plutonic environment over a long time, while for porphyritic rocks the formation environment was not so straight forward and required a closer look at textures and composition (Watts, 1804; Judd and Cole, 1883).

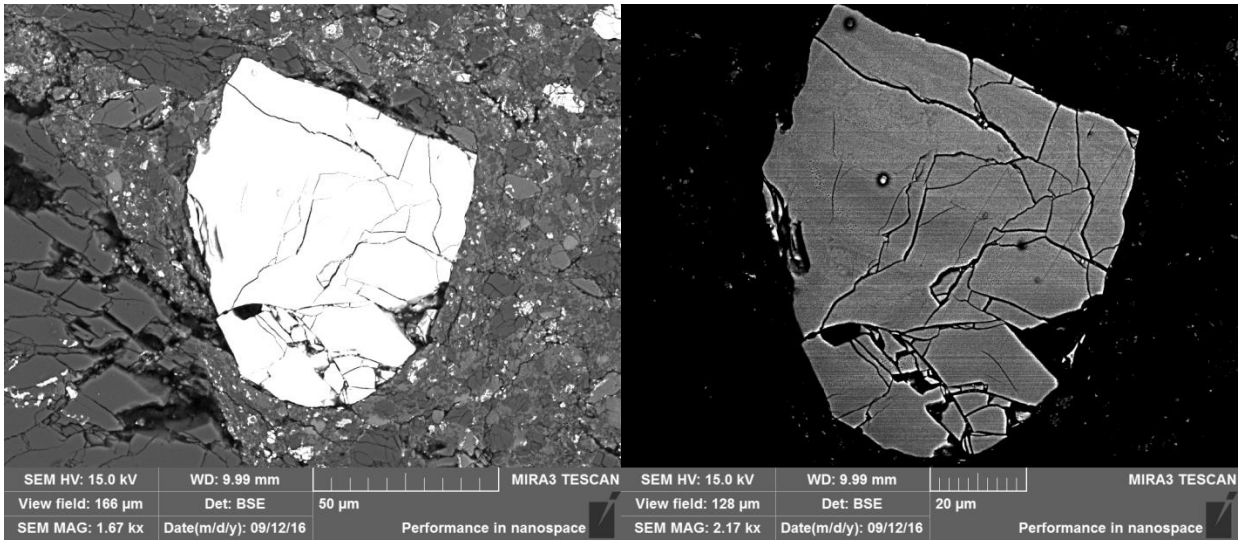

Figure 11: Back scatter imaging revealing differences in elemental composition in the form of light and dark shading of a zircon from mount 534, with heavy elements appearing brighter than light elements. When increasing the contrast and brightness in Tescan (SEM analytical program) zoning patterns could be detected. The images show a broken zircon with zoning in direction parallel to the grain boundary/ fracture zone. Also note the change in colour outlining the edges and along cracks, showing further chemical alteration.

2.4 ASSUMPTIONS

The results were analysed based on the following five assumptions:

(1) Phase components, temperature- and pressure conditions for minerals formed on Earth are similar enough to be applied to minerals formed on Mars.

(2) Pressure was assumed to be 1 atmosphere unless otherwise stated. While this is not realistic, determining the accurate pressure would require the burial depth, impact pressure, and atmospheric thickness at formation for all components. This is out of scope.

(3) Impact melt clasts found within matrix originated from an older impact event.

(4) Composition of feldspars, pyroxenes, polymineralic clasts contained in older generation impact melt clasts vary in composition to feldspars, pyroxenes and polymineralic clasts contained in groundmass.

(5) Clast composition and textures reflect the climate and main rock-forming processes that were characteristic of their period in Mars' history.

3 RESULTS

This section identifies and describes the assemblage of clasts identified via electron microprobing and Qemscan analysis. The focus was on clasts made up of or containing feldspar and pyroxene. Normalised mineral compositions for the most abundant phases were determined based on Qemscan data from mounts: 458-1, 458-2, 458-3, 372, 362 and 534; Figure 1, Figure 12). These were: clinopyroxene (45%), orthopyroxene (15%), Mg-phyllosilicates (17%), plagioclase (17%), alkali feldspar (1%), oxides (3%), apatite (1%), and olivine (1%). Notable was the presence of microscopic zircons scattered throughout, with the largest piece being 70x70 µm long and found in mount 534 (Figure 11). Overall, mounts sampled had similar composition. They were all mafic and contained a high amount of microscopic iron oxides and varied only in the distribution and quantity of phenocrysts and polymineralic clasts. They contained phenocrysts of plagioclase, orthoclase, pyroxene, olivine, apatite, ilmenite, chromite and pyrrhotite; and several types of polymineralic clasts, such as: norite-pyroxenite, gabbronorite, gabbro, pyroxene and plagioclase spherules, apatite-plagioclase and ilmenite-plagioclase clasts. Clasts were grouped into clast types and sub-types based on their composition and textural characteristics. The five most abundant clast types were defined as major clasts (Table 4). These included: gabbroids (gabbro and gabbronorite), plagioclase phenocrysts (albites and anorthites), pyroxene phenocrysts (enstatites and augites), impact melt clasts, and apatite-plagioclase clasts. Chemical compositions, as determined by electron microprobing, were normalised according to Ca-Na-K content for feldspars and Ca-Mg-Fe content for pyroxene, and were plotted in ternary phase diagrams developed by Yoder *et al.,* (1957) and Lindsley (1983), respectively.

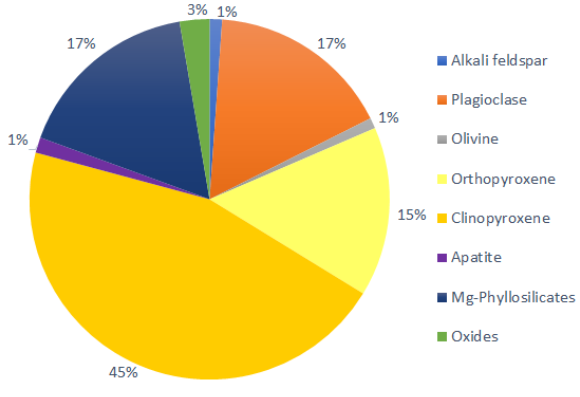

Figure 12: Normative mineralogy of the major minerals making up NWA 7034, recorded by Qemscan.

The main matrix, heron referred to as matrix, was a porphyritic, aphanitic, intergranular intergrowth of feldspar (primarily plagioclase), pyroxene (enstatite and augite), and interstitial metal oxides and Mg-phyllosilicates. Groundmass that differed to the main matrix in composition, texture, or grainsize was deemed an impact melt clast. For the most part, impact melt clasts had a higher clinopyroxene/orthopyroxene ratio, contained less Mg-phyllosilicates. Some contained more alkali feldspars/plagioclase than the matrix, others less (see Supplementary Material). Feldspar compositions overlapped for the most part, however impact melt clasts contained components of extremely potassic (>80%) composition. A trend could be identified in the pyroxenes. Pyroxenes in impact melt clasts had a higher Mg/Fe ratio than those in the matrix (Figure 13).

Table 4: Clast types identified in NWA 7034.

Clast Type	*Sub-Type*	*Major/Minor*
Gabbroic clast	norite-pyroxenite	minor
	gabbronorite	major
	gabbro	major
Feldspar phenocryst	perthite	minor
	albite (Na end member)	major
	anorthite (Ca end member)	major
	orthoclase (K end member)	minor
Pyroxene phenocryst	enstatite (orthopyroxene, Mg end member)	major
	augite (clinopyroxene, intermediate)	major
	ferrosilite (orthopyroxene, Fe end member)	minor
	pigeonite (clinopyroxene, intermediate)	minor
Apatite-plagioclase	-(ilmenite)	major
Peridotite		minor
Fe-Ti oxides	magnetite	minor
	ilmenite	minor
	transitional	minor
Sulphide	in veins	minor
	as part of clasts	minor
Impact melt clast		major
Quench clasts	quenched pyroxene phenocrysts	minor
	spherules	minor

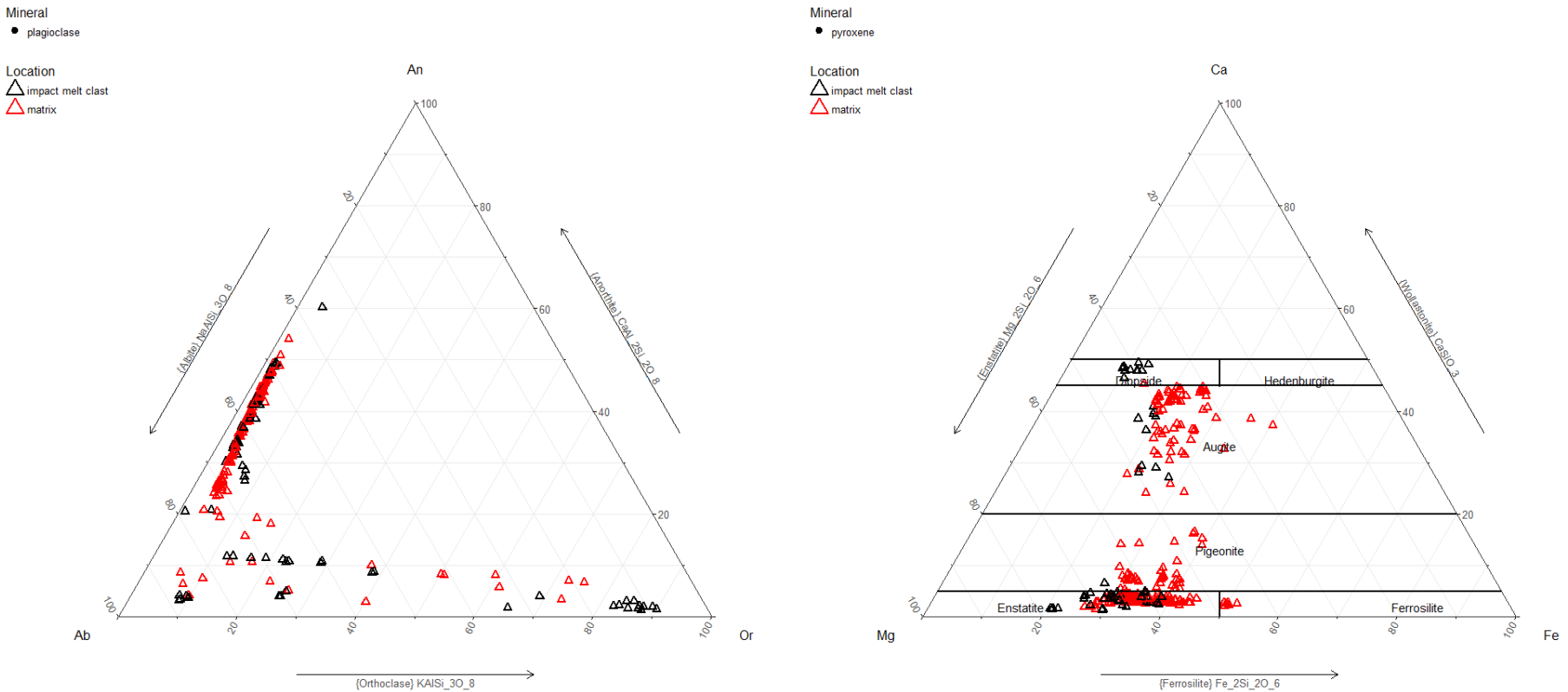

Figure 13: Composition of feldspars (left) and pyroxene (right) in matrix and impact melt clasts, based on normalized proportions of Na, Ca, K (left), and Mg, Ca, Fe (right). Grid represents areas of stability for the separate phase components.

3.1 FELDSPAR PHENOCRYSTS

Plagioclase were for the most part sodic. Highly calcic components were not present. Alkali feldspar phenocrysts occurred as perthites. Feldspars were grouped, based on their defining zoning patterns and composition. Four sub-types were observed: perthite, albite, anorthite (Table 5).

Table 5: Feldspars with their defining characteristic composition and -textures, and zoning patterns (from core to rim of spherule) and associated samples.

Classification	*Defining characteristics*	*Growth textures*	*Zoning in feldspar*	*Representative sample(s)*
Perthite	Irregular intergrowths of orthoclase and albite	perthitic, patchy (honeycomb), embayed	K - Na, Ca	372 alk, 372 pl (c)1, 372 pl (c)1 GM, 362 pl (c)2
Albite [a)]	Na-rich composition	none, exsolution lamellae	none; core to rim (Ca to Na); exsolution lamellae (Ca – Na)	362 pl (c)1, 362 pl (c)3, 372 pl (c)1, 362 pl (m)1, 362 pl (m)3
Albite [b)]	Na-rich composition with irregular intergrowths of andesine and oligoclase	exsolution lamellae, patchy	exsolution lamellae (Ca – Na)	458-3 pl (m)2
Anorthite	Ca-rich composition	None	none	458-3 pl (m)1

Perthite phenocrysts had a "honeycomb" texture featuring irregular intergrowths of potassium rich orthoclase and sodium rich albite. Some perthites contained both honeycomb and lamellar exsolution (Figure 17). Neither component was dominantly present, making them mesoperthite (Michot, 1951). Clast boundaries were well defined. There were no reaction coronas along clast boundaries. Matrix around rim was deformed and contained accumulations of iron oxides and other phases arranged in sinusoidal shapes (Figure 16). Perthite phenocrysts were sub-rounded (Figure 14) to sub-angular (Figure 15, Figure 17). They were highly fractured. Some fractures were filled with an unknown phase, likely iron oxide. Qemscan identified the groundmass of a cluster of impact melt perthites to be high in augite as opposed to surrounding matrix. Impact melt clasts that contained these were frequently crosscut by cracks and filled in veins. Veins were crosscut by other phases, namely iron oxides and ilmenite (Figure 16).

Albite phenocrysts were fractured. Some cracks had been filled in. The glassy component in one of these cracks was sampled and determined to be a feldspar, but more sodic than the clast it was contained in (Figure 22). Clasts were sub-angular and angular. Some had embayed clast boundaries with concave indentations. Some displayed minor core to rim zoning (Ca to Na). Lamellar intergrowths of Na and Ca rich phases were present in some instances (Figure 19, Figure 23). Other phenocrysts were homogenous in composition (Figure 20, Figure 21 and Figure 22). These were angular, with their hexagonal shape remaining intact. One clast had the same composition as plagioclase sampled from the nearby groundmass (Figure 22). One of the phenocrysts sampled was unique, as it had both patchy and lamellar intergrowths of andesine and oligoclase (Figure 23).

The only *anorthite* to be sampled (more specifically, a labradorite) was contained in quench alongside a peridotite (Figure 24). It had a homogenous composition. Unlike the peridotite, the plagioclase phenocryst remained had angular edges well intact. Cracks were present but not filled in. However, it had a narrow metal oxide reaction rim along clast boundary.

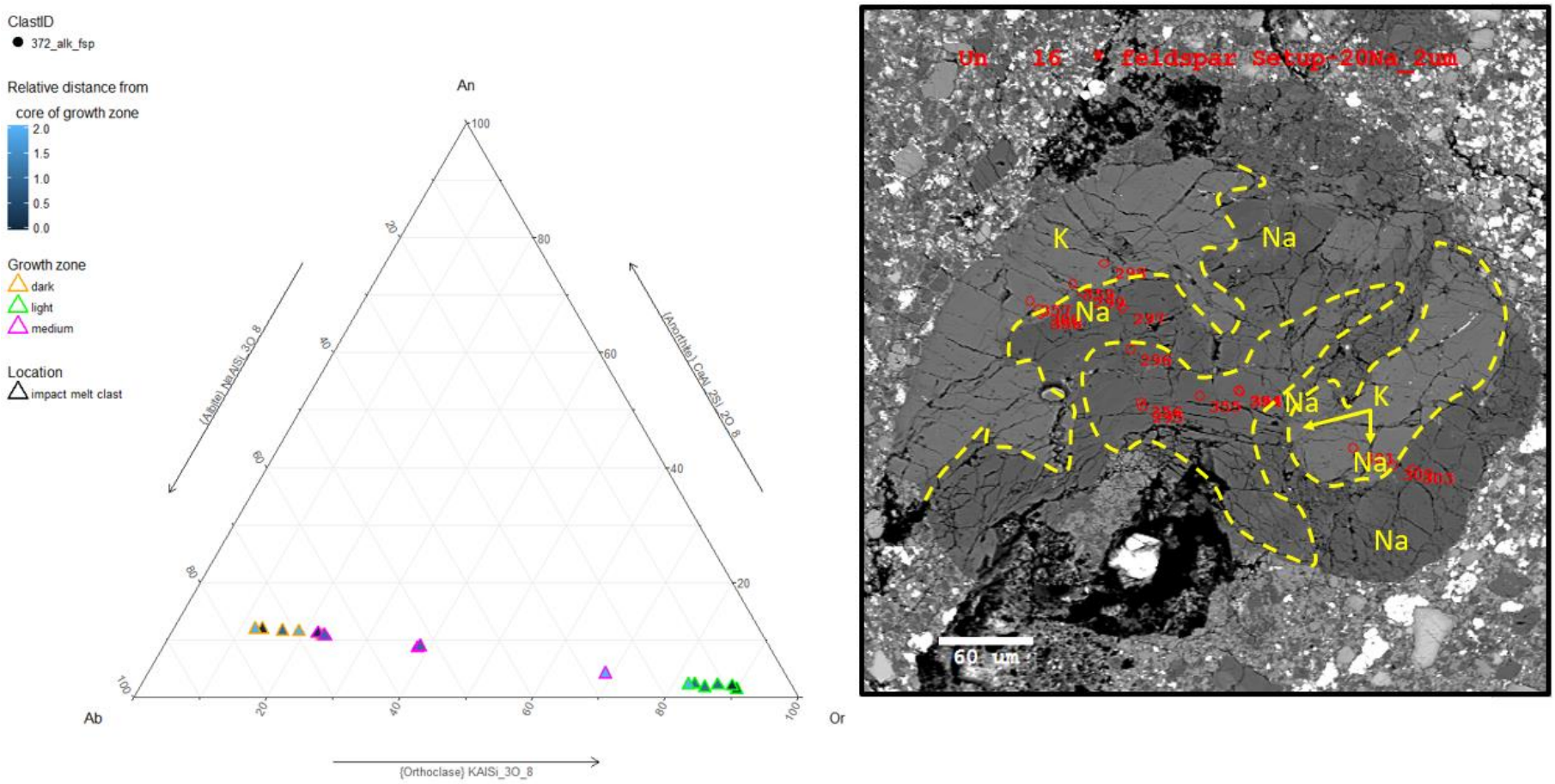

Figure 14: Feldspar composition of perthite phenocryst, based on normalized proportions of Na, Ca and K. Grid represents areas of stability for the separate feldspar components. Blue bar denotes relative distance from core of growth zone, with 0.0 (dark blue) representing the core, and 2.0 (light blue) representing the rim. Shape denotes clast location (matrix or impact melt clast). (Right) BSE image with electron microprobe sampling points (red) and zoning direction (yellow arrows). Note phenocrysts separated from clast by melt (dotted line).

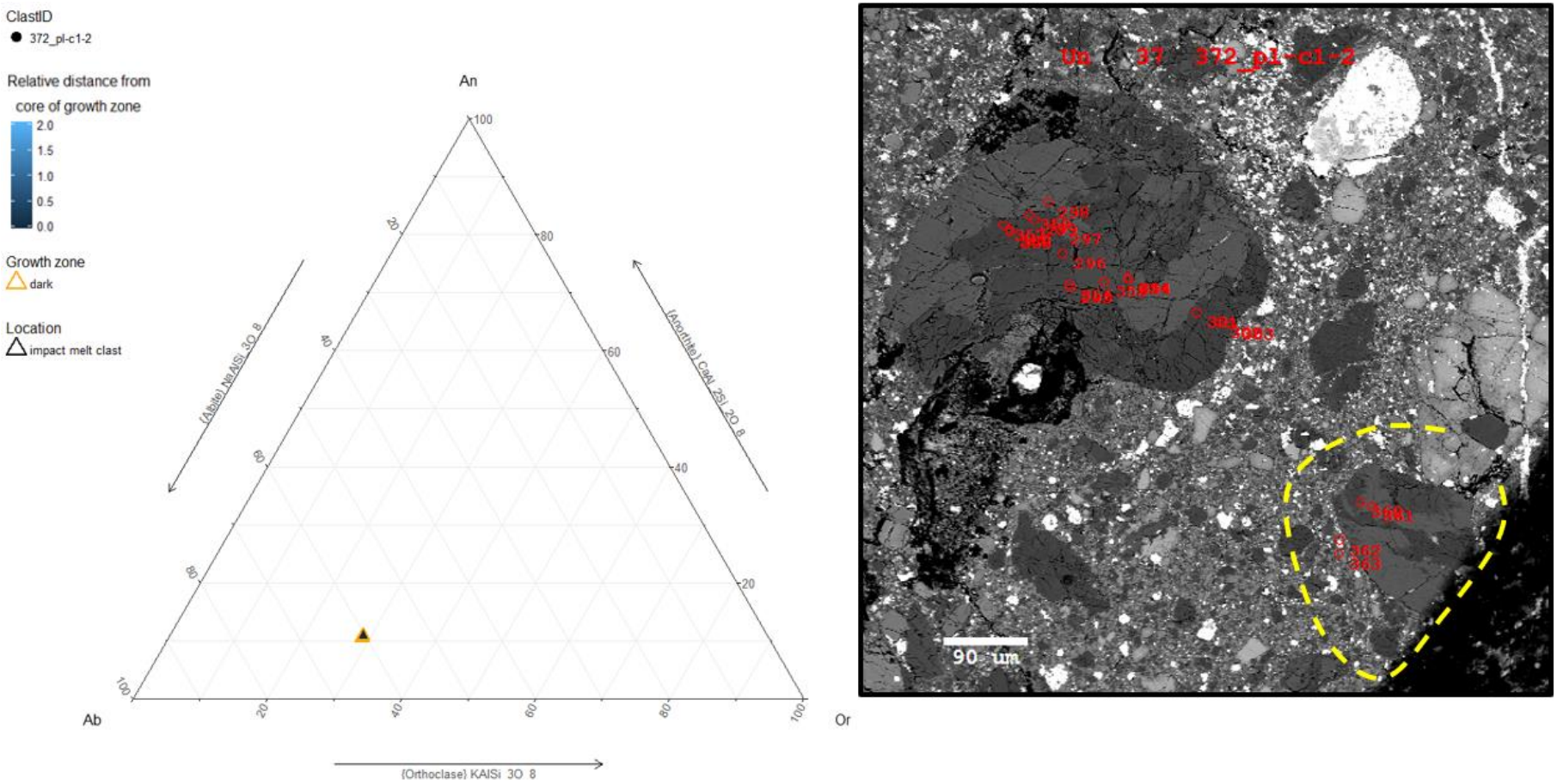

Figure 15: Feldspar composition of perthite phenocryst (clast in dotted yellow line), based on normalized proportions of Na, Ca and K. Grid represents areas of stability for the separate feldspar components. Blue bar denotes relative distance from core of growth zone, with 0.0 (dark blue) representing the core, and 2.0 (light blue) representing the rim. Shape denotes clast location (matrix or impact melt clast). (Right) BSE image with electron microprobe sampling points (red) and zoning direction (yellow arrows). Note phenocrysts separated from clast by melt (dotted line).

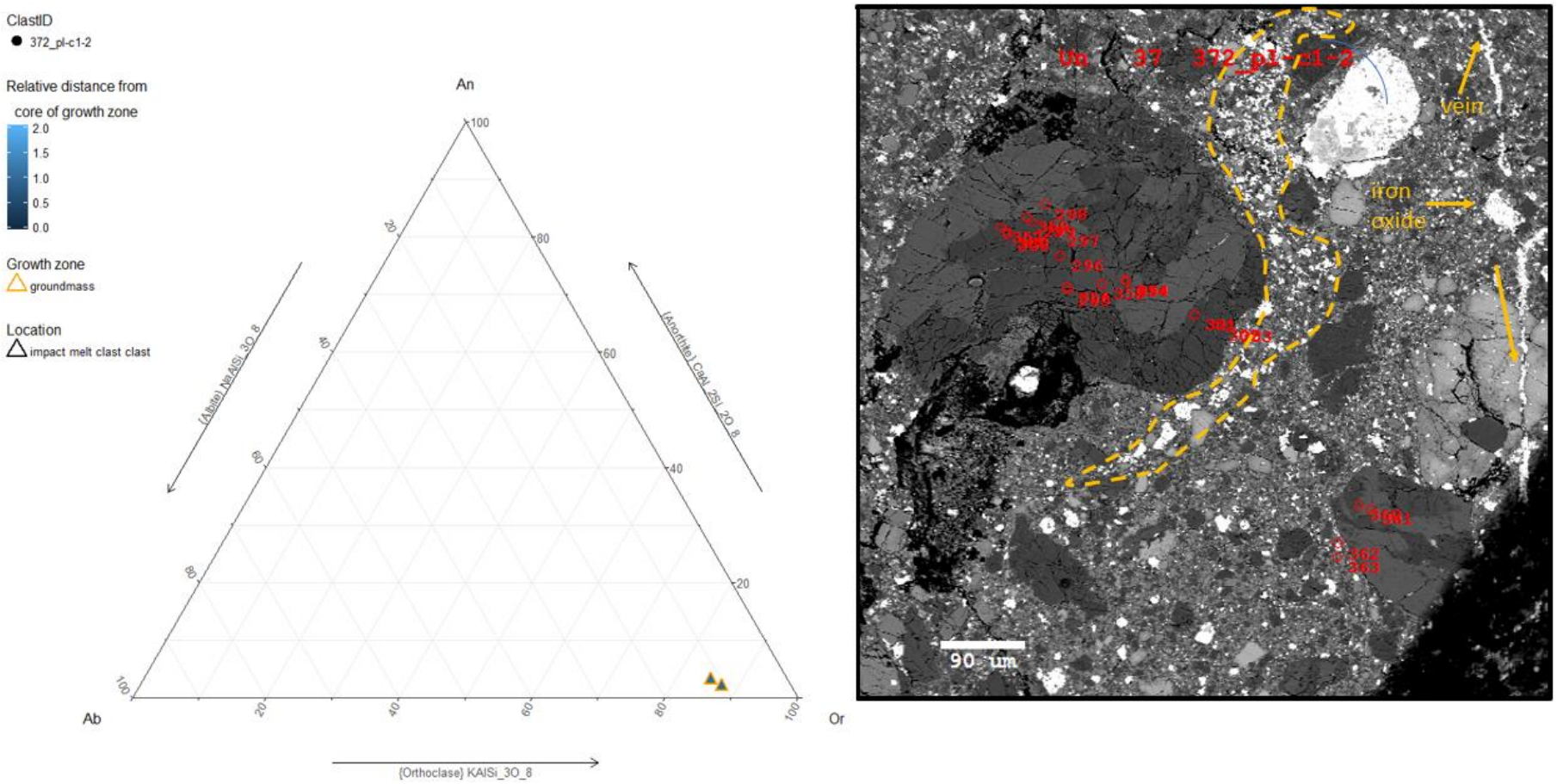

Figure 16: Feldspar composition of groundmass adjacent to perthite clast, based on normalized proportions of Na, Ca and K. Grid represents areas of stability for the separate feldspar components. Blue bar denotes relative distance from core of growth zone, with 0.0 (dark blue) representing the core, and 2.0 (light blue) representing the rim. Shape denotes clast location (matrix or impact melt clast). (Right) BSE image with electron microprobe sampling points (red) and zoning direction (yellow arrows). Note phenocrysts separated from clast by melt (dotted line). Note vein offset by iron oxide, and sinusoidal assemblage of iron oxides (dotted yellow line).

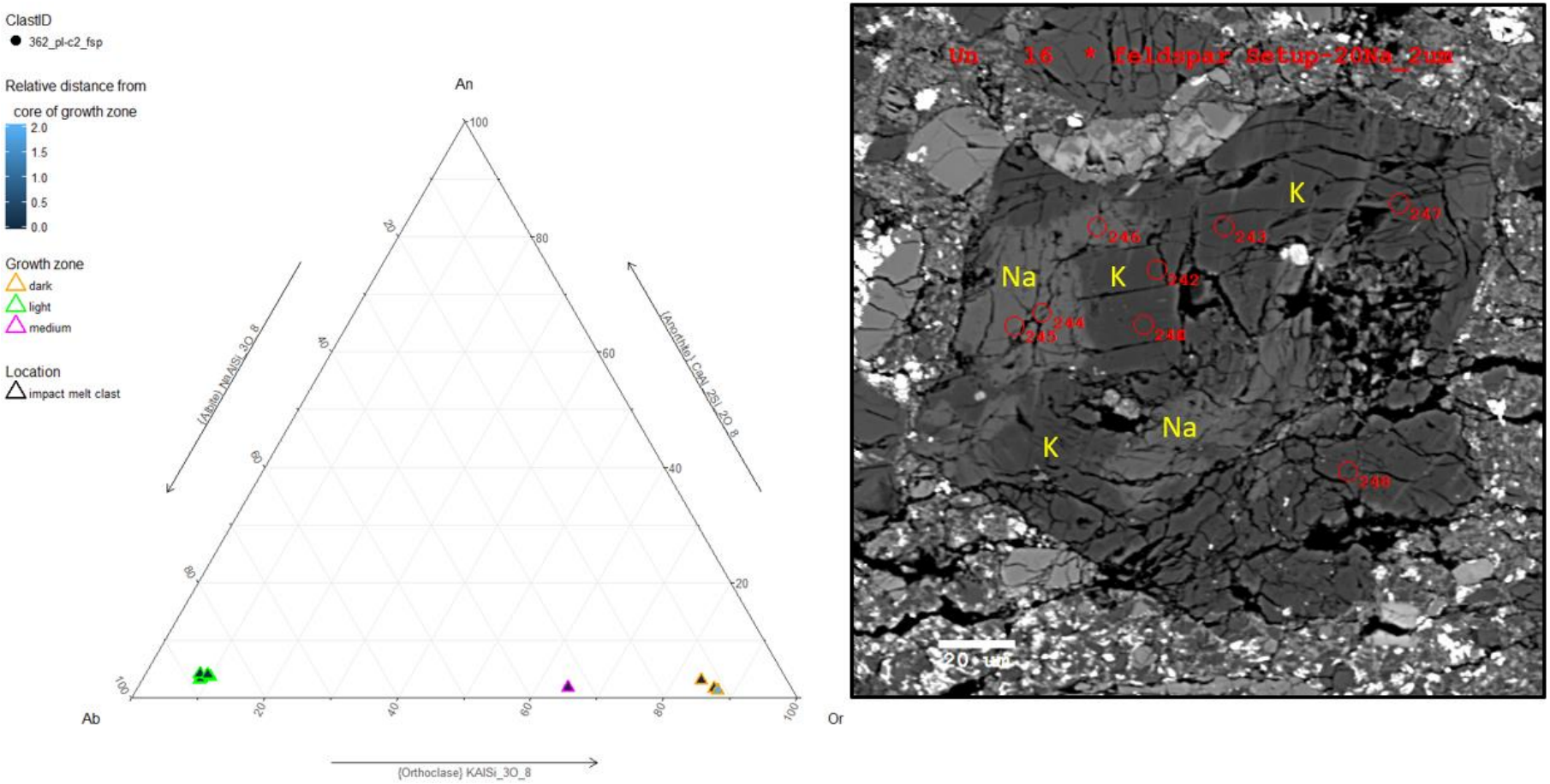

Figure 17: Feldspar composition of perthite phenocryst, based on normalized proportions of Na, Ca and K. Grid represents areas of stability for the separate feldspar components. Blue bar denotes relative distance from core of growth zone, with 0.0 (dark blue) representing the core, and 2.0 (light blue) representing the rim. Shape denotes clast location (matrix or impact melt clast). (Right) BSE image with electron microprobe sampling points (red) and zoning direction (yellow arrows). Note phenocrysts separated from clast by melt (dotted line).

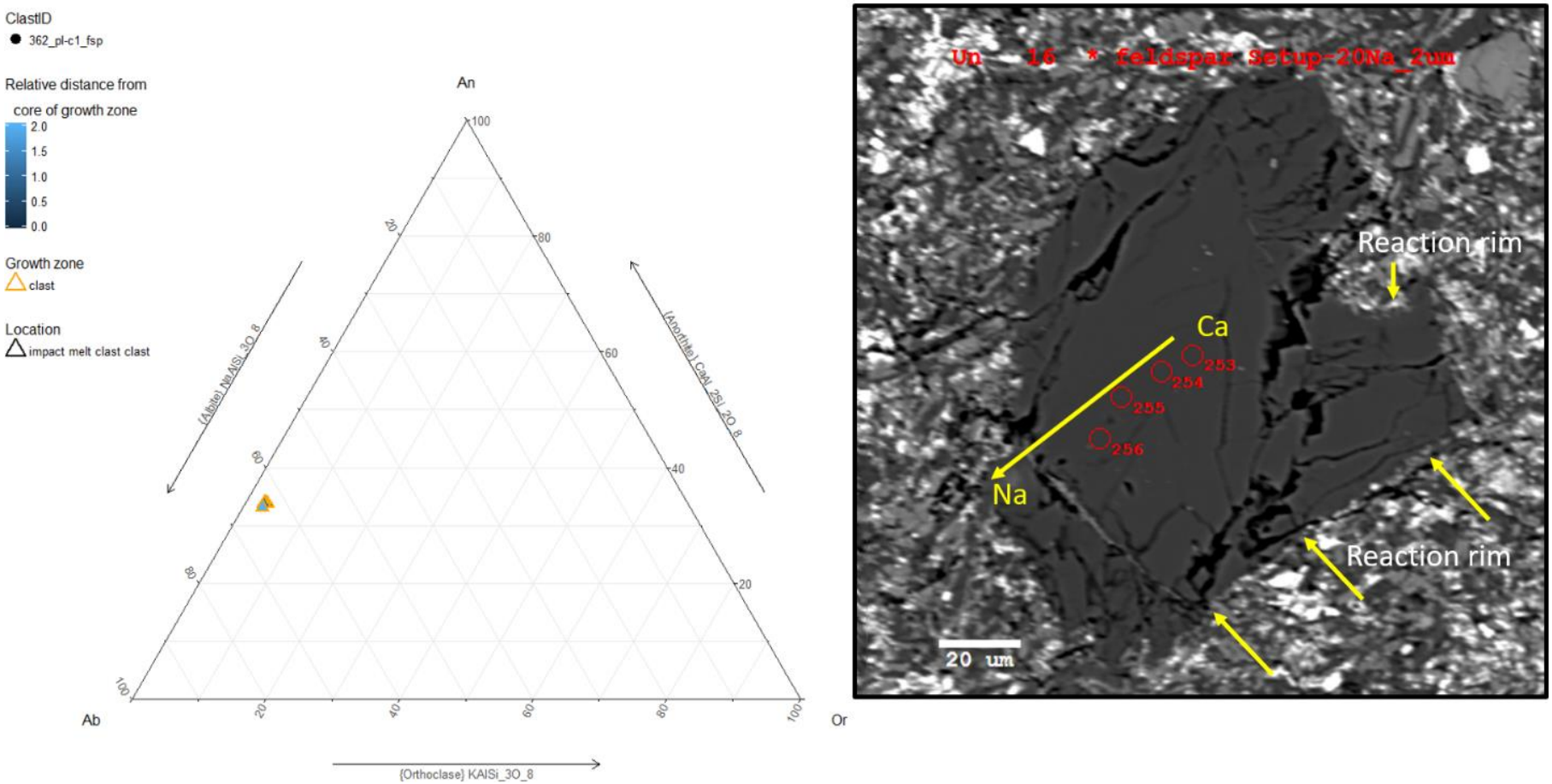

Figure 18: Feldspar composition of albite phenocryst, based on normalized proportions of Na, Ca and K. Grid represents areas of stability for the separate feldspar components. Blue bar denotes relative distance from core of growth zone, with 0.0 (dark blue) representing the core, and 2.0 (light blue) representing the rim. Shape denotes clast location (matrix or impact melt clast). (Right) BSE image with electron microprobe sampling points (red) and zoning direction (yellow arrows). Note phenocrysts separated from clast by melt (dotted line).

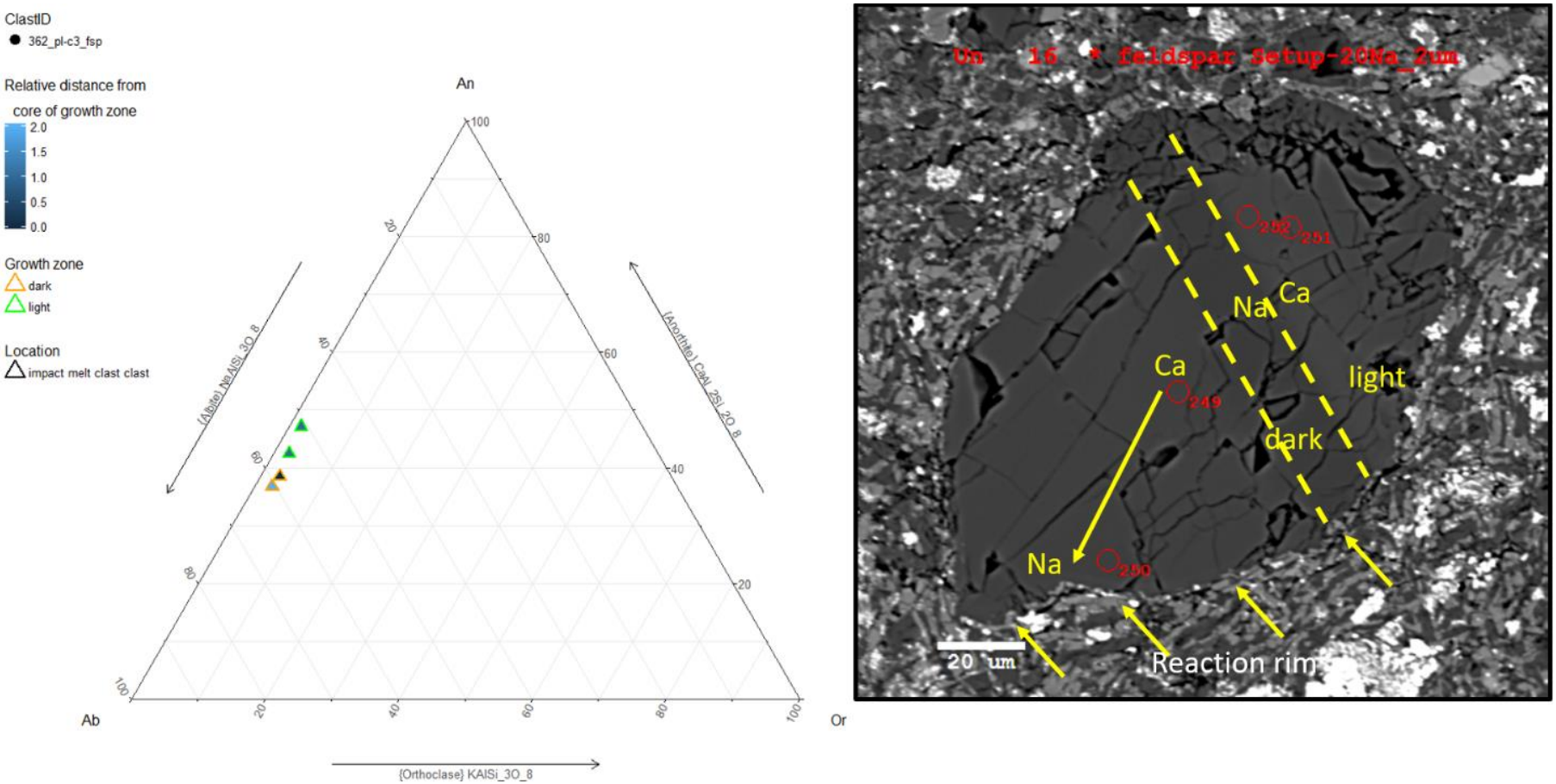

Figure 19: Feldspar composition of albite phenocryst, based on normalized proportions of Na, Ca and K. Grid represents areas of stability for the separate feldspar components. Blue bar denotes relative distance from core of growth zone, with 0.0 (dark blue) representing the core, and 2.0 (light blue) representing the rim. Shape denotes clast location (matrix or impact melt clast). (Right) BSE image with electron microprobe sampling points (red) and zoning direction (yellow arrows). Note phenocrysts separated from clast by melt (dotted line).

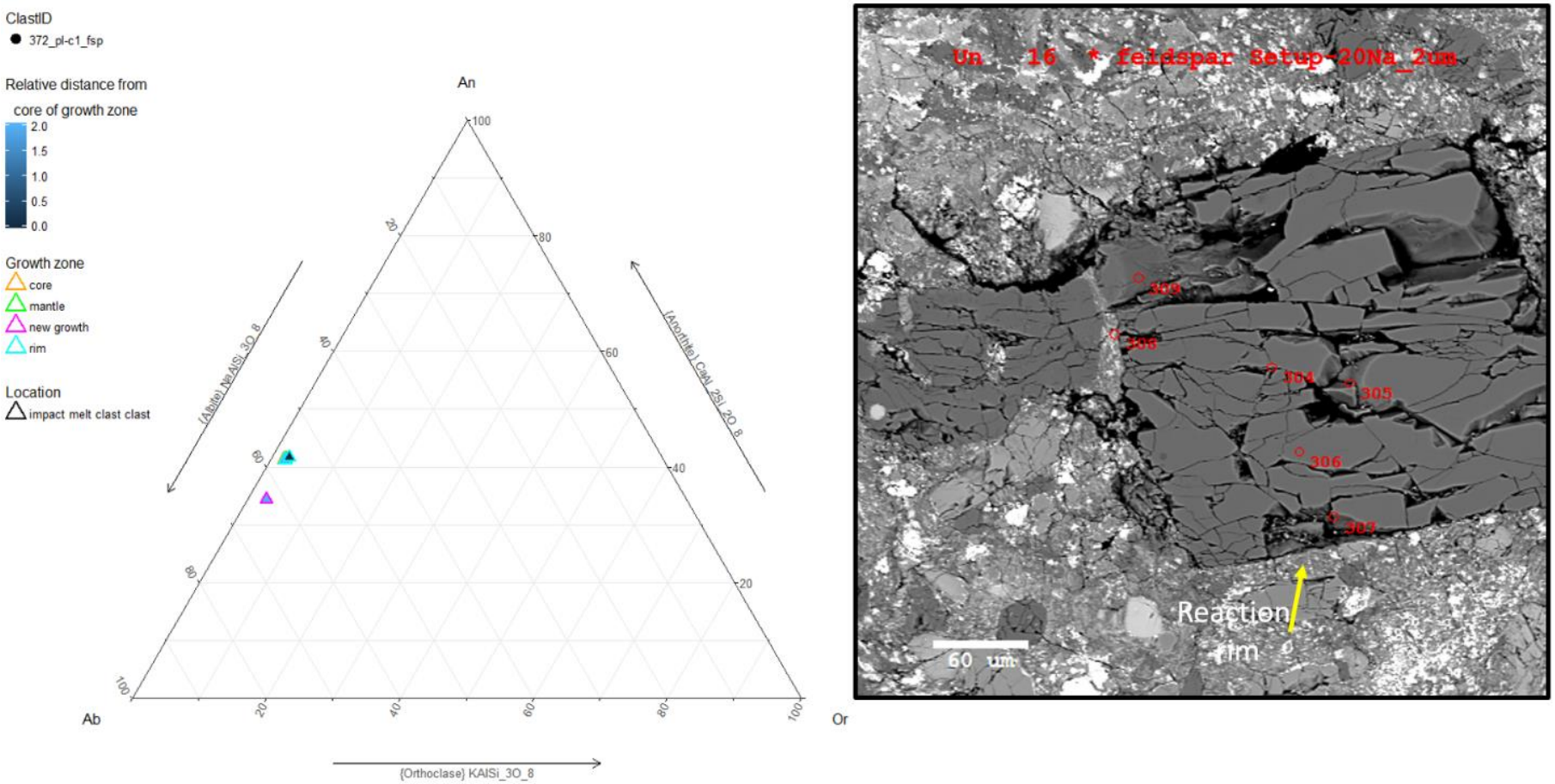

Figure 20: Feldspar composition of albite phenocryst, based on normalized proportions of Na, Ca and K. Grid represents areas of stability for the separate feldspar components. Blue bar denotes relative distance from core of growth zone, with 0.0 (dark blue) representing the core, and 2.0 (light blue) representing the rim. Shape denotes clast location (matrix or impact melt clast). (Right) BSE image with electron microprobe sampling points (red) and zoning direction (yellow arrows). Note phenocrysts separated from clast by melt (dotted line).

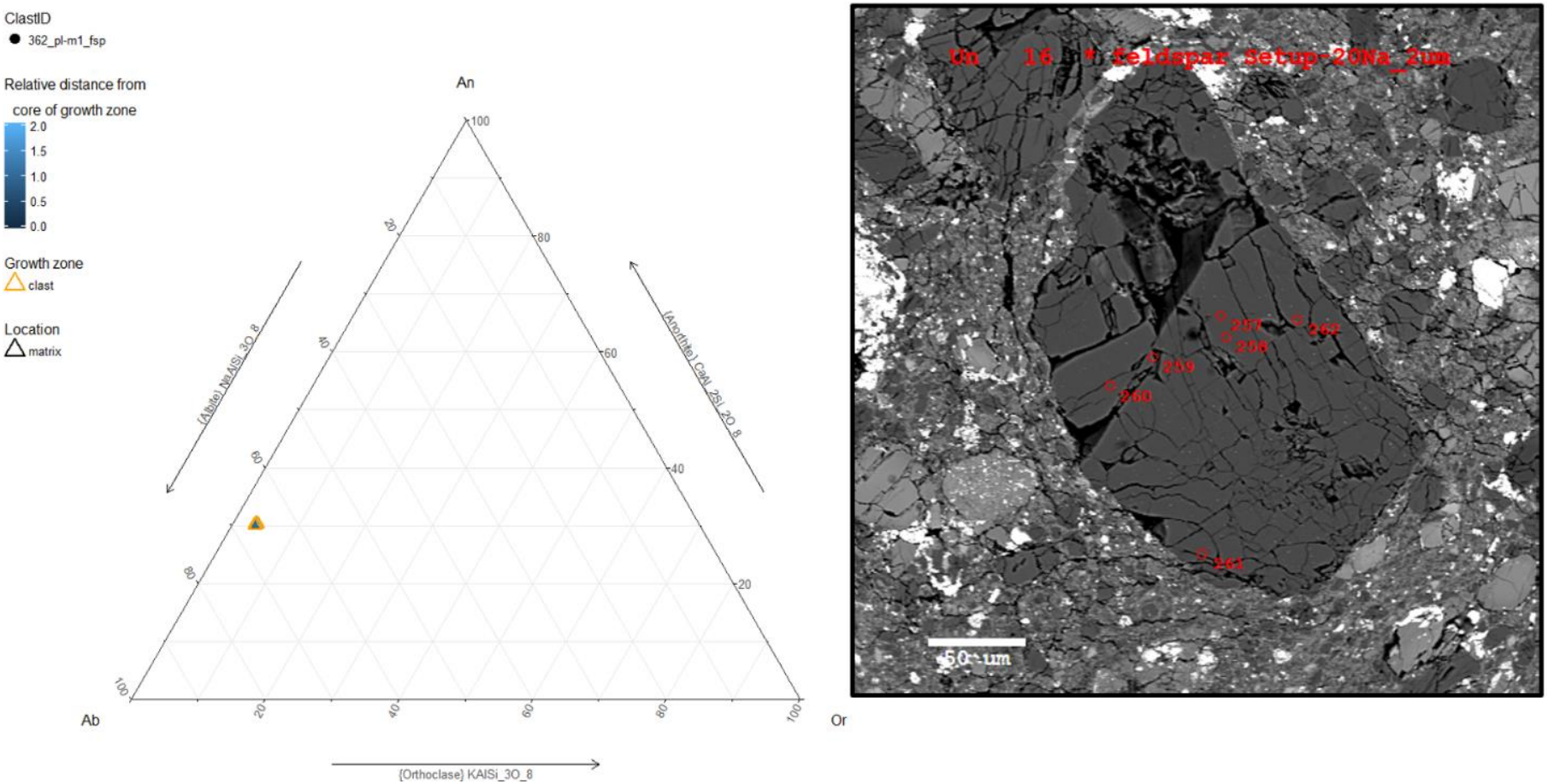

Figure 21: Feldspar composition of albite phenocryst, based on normalized proportions of Na, Ca and K. Grid represents areas of stability for the separate feldspar components. Blue bar denotes relative distance from core of growth zone, with 0.0 (dark blue) representing the core, and 2.0 (light blue) representing the rim. Shape denotes clast location (matrix or impact melt clast). (Right) BSE image with electron microprobe sampling points (red) and zoning direction (yellow arrows). Note phenocrysts separated from clast by melt (dotted line).

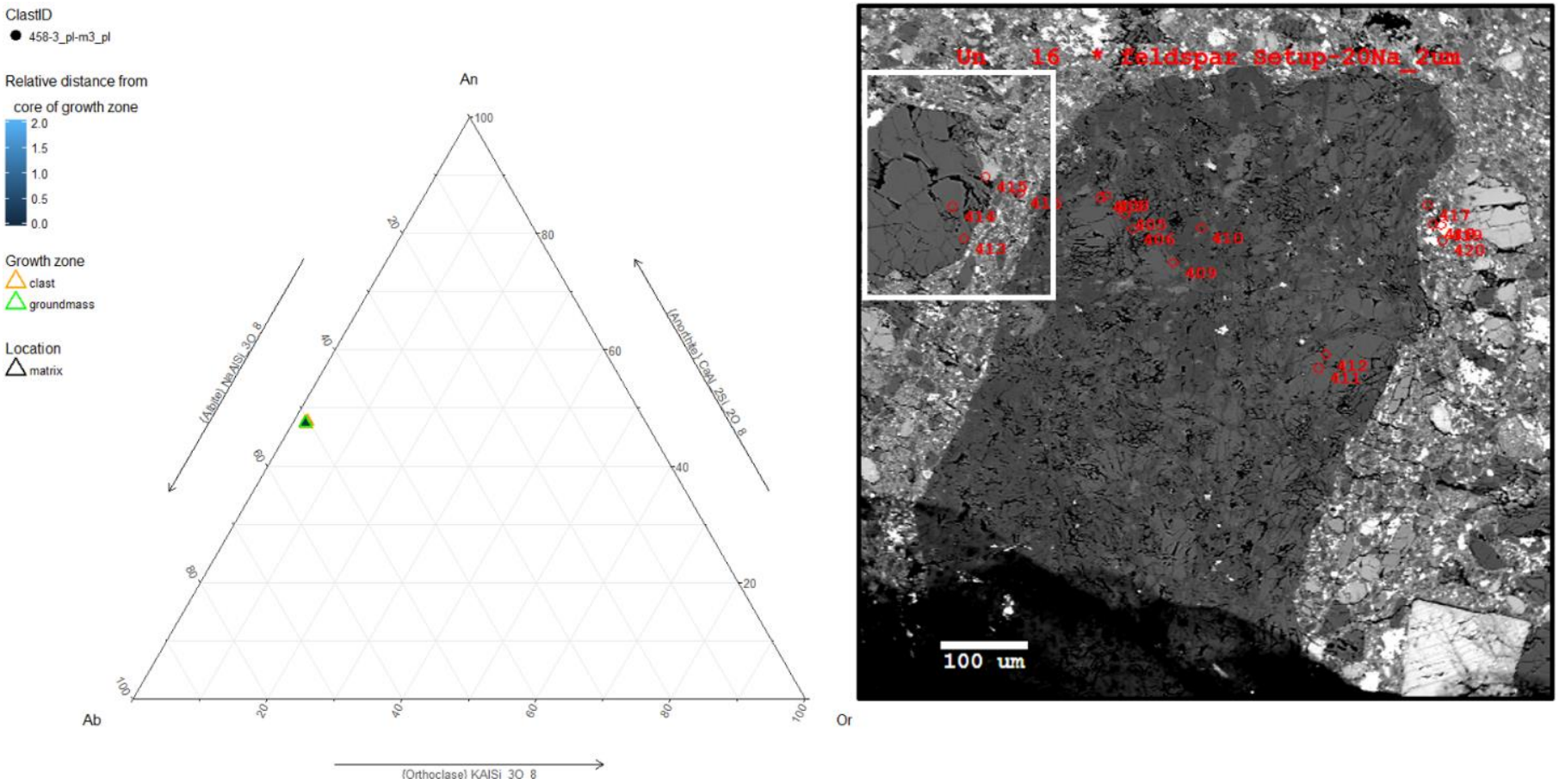

Figure 22: Feldspar composition of albite phenocryst (clast in white square), based on normalized proportions of Na, Ca and K. Grid represents areas of stability for the separate feldspar components. Blue bar denotes relative distance from core of growth zone, with 0.0 (dark blue) representing the core, and 2.0 (light blue) representing the rim. Shape denotes clast location (matrix or impact melt clast). (Right) BSE image with electron microprobe sampling points (red) and zoning direction (yellow arrows). Note phenocrysts separated from clast by melt (dotted line).

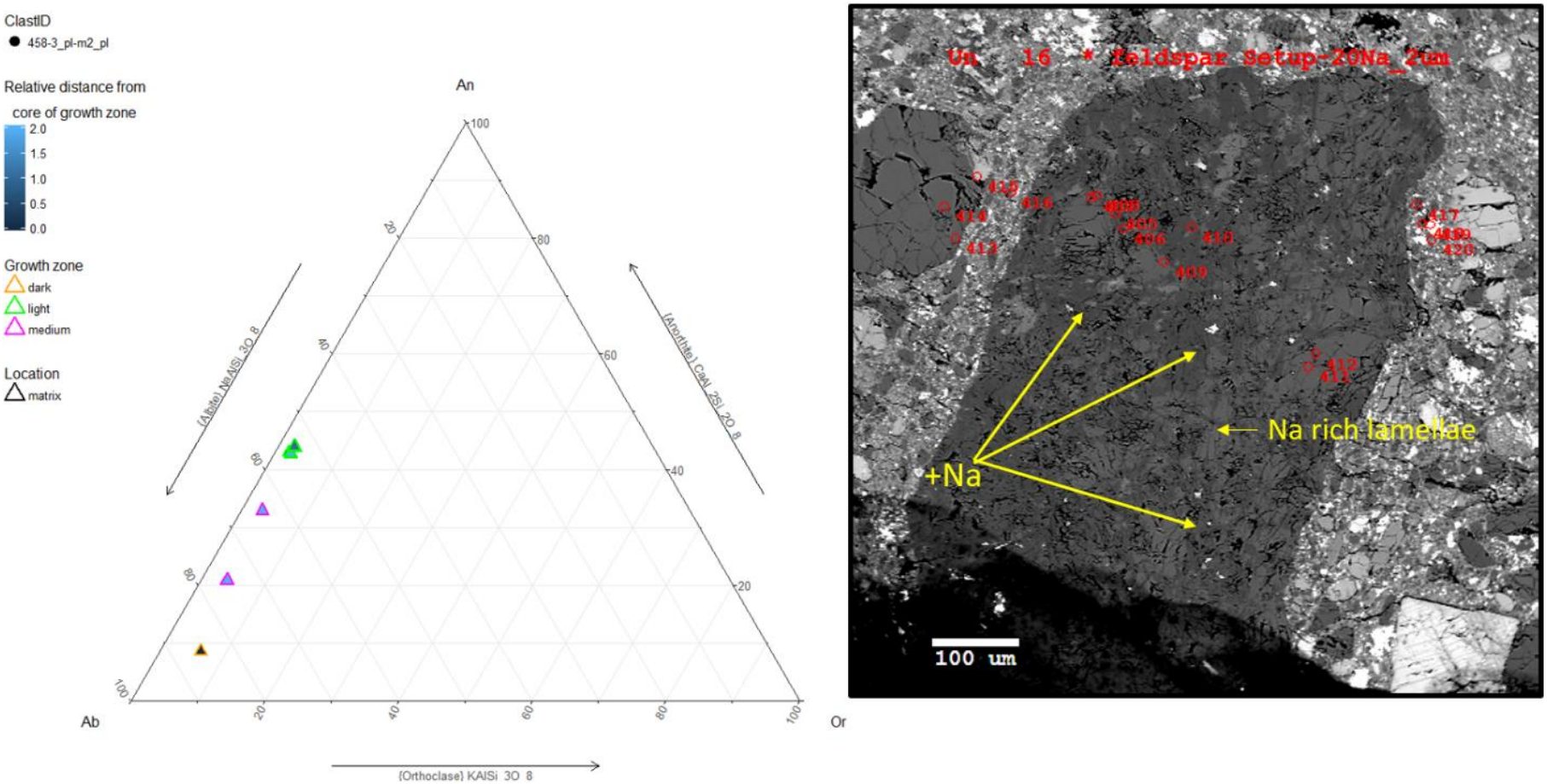

Figure 23: Feldspar composition of albite phenocryst, based on normalized proportions of Na, Ca and K. Grid represents areas of stability for the separate feldspar components. Blue bar denotes relative distance from core of growth zone, with 0.0 (dark blue) representing the core, and 2.0 (light blue) representing the rim. Shape denotes clast location (matrix or impact melt clast). (Right) BSE image with electron microprobe sampling points (red) and zoning direction (yellow arrows). Note phenocrysts separated from clast by melt (dotted line).

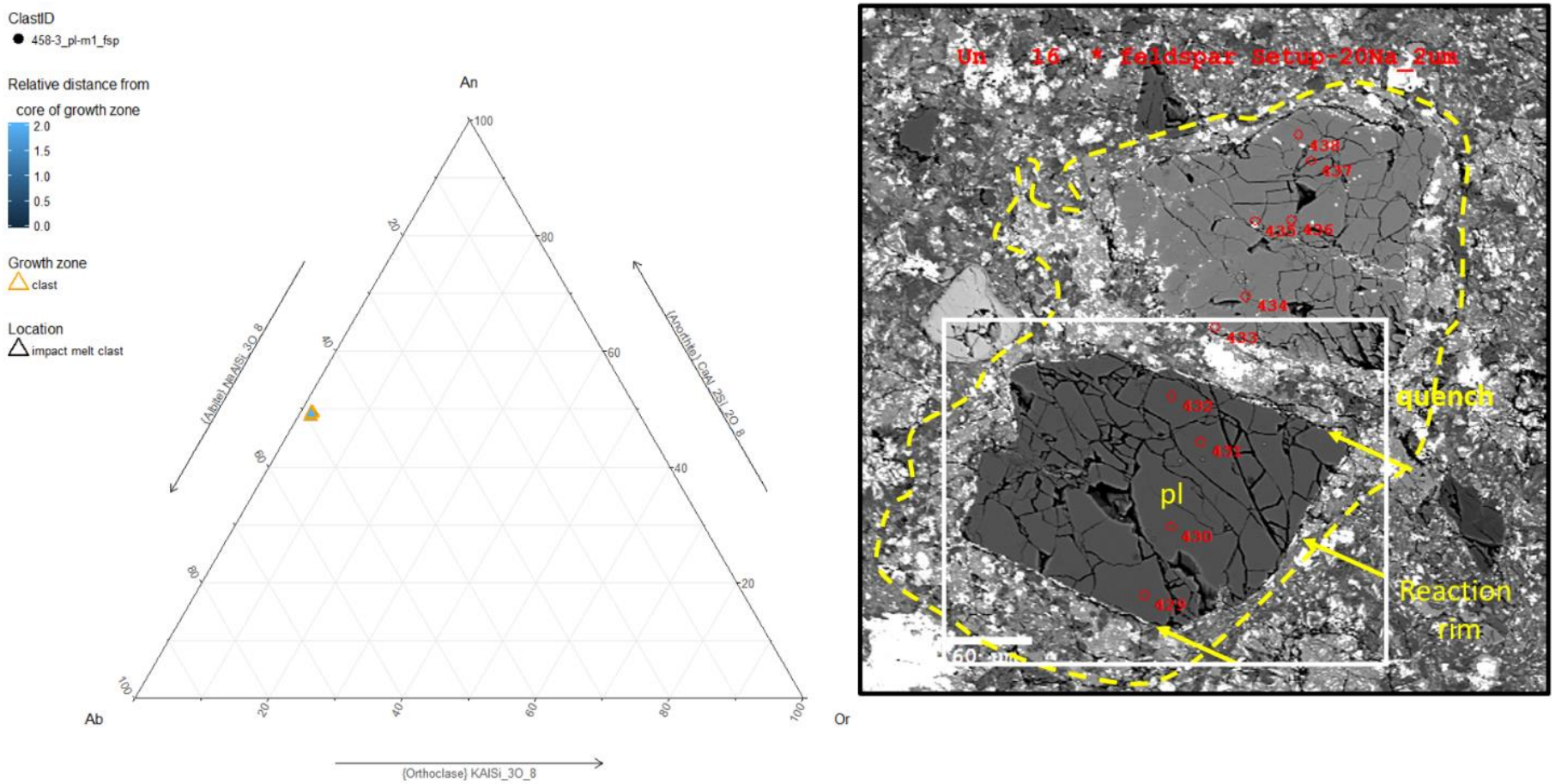

Figure 24: Feldspar composition of anorthite phenocryst (clast in white square), based on normalized proportions of Na, Ca and K. Grid represents areas of stability for the separate feldspar components. Blue bar denotes relative distance from core of growth zone, with 0.0 (dark blue) representing the core, and 2.0 (light blue) representing the rim. Shape denotes clast location (matrix or impact melt clast). (Right) BSE image with electron microprobe sampling points (red) and zoning direction (yellow arrows). Note phenocrysts separated from clast by melt (dotted line).

3.2 PYROXENE PHENOCRYSTS

Pyroxene phenocrysts in the matrix displayed a wide range of composition, ranging from high Ca augite to enstatite and ferrosilite. Composition was significantly more magnesic than ferric. Compositional variations were found in the form of intergrowths, patches or exsolution lamellae. Pyroxenes were grouped into sub-types based on their defining zoning patterns and composition. Six sub-types were observed (Table 6). Clasts containing lamellar intergrowths of three distinct components were identified. These were: intergrowths of pigeonite-augite, Mg-augite with Fe-richer augite, and augite-orthopyroxene.

Table 6: Pyroxene types with their defining characteristic composition and -textures, and zoning patterns (from core to rim of spherule) and associated samples.

Type	*Defining characteristics*	*Growth textures*	*Zoning in pyroxene*	*Representative sample(s)*
Lamellar intergrowth a	pigeonite-augite intergrowth	exsolution lamellae, patchy	exsolution lamellae (Mg - Fe, Ca) and core to rim (Fe to Ca)	362 px (m)4
b	low- and high Ca augite intergrowth	exsolution lamellae	exsolution lamellae (Mg - Fe), core to rim (Mg to Ca)	A u1 px, 372 pigeonite px (m)2, D px (m)1
c	augite-orthopyroxene intergrowth	exsolution lamellae, twinning	Fe - Ca; Mg - Fe	372 pigeonite px (m)1, 534 px (m)1
Patchy intergrowth	enstatite-ferrosilite intergrowth with some diopside	patchy, twinning	Mg - Fe; Mg, Fe - Ca	362 px (m)1
Enstatite	enstatite		none	362 px (m)6, 362 px (m)2, A fpx (m)1
Augite	augite		core to rim (Fe to Mg)	D u1

Pigeonite-augite intergrowths were represented by one sample (Figure 25). It was heavily fractured. Oxide inclusions crosscut fractures. Zoning occurred in the form of two-directional exsolution lamellae (Mg - Fe, Ca) and core to rim (Fe to Ca). Pigeonite was found in the core, and augite along the rim. This clast was angular. Remnants of monoclinic crystal face remained intact, with planes intersecting at ~120˚.

Augite phenocrysts with intergrowths of *low- and high Ca augite*, often had speckles of oxides along the lamellae (Figure 27, Figure 28). They exhibited core to rim zoning, where the core was enriched in Ca, relative to the clast rim. Clast boundaries were oriented at an angle of about 120˚-60˚ from lamellae, or 90˚. Fractures propagated parallel and perpendicular to lamellae. Clasts were angular, with well defined, straight clast boundaries. Reaction rims with oxides along clast boundary were present (Figure 27).

The third variation of lamellar intergrowths was characterised by *high-Ca augite* with exsolution lamellae of *ferrosilite* or *enstatite* (Figure 29, Figure 30). Clasts were moderately fractured. Some fractures occurred parallel to lamellae, others crosscut them at 120˚. Crystal faces were oriented at ~120˚ and 60˚ to each other. Melt around it was zoned by grainsize (small to large, away from clast). One clast displayed twinning, with twins intersecting at ~ 60˚ (Figure 30). Clasts were sub-angular and angular. Melt around clast was elastically deformed and zoned by grainsize (small to large, away from clast).

Enstatite with intergrowths of *ferrosilite* and *augite* were represented by one sample (Figure 31). It had twinning and additional compositional zoning with patchy areas of augite, enstatite and ferrosilite, and

contained scattered iron oxide inclusions. Equigranular gabbronorite, composed of plagioclase, pyroxene and iron oxides, was found in a ~100 µm area along the rim of the clast. The clast was sub-rounded. In the matrix adjacent to the clast, was a zone of equigranular plagioclase-pyroxene, that was enriched in metal-oxide phases relative to the rest of the matrix, and was zoned by grainsize (small to large, away from clast).

Enstatites in the matrix occurred as sub-angular clasts with well-defined clast boundaries. The compositional range of the phenocrysts was narrow (< 5% variation), one of the clasts exhibited core to rim zoning from Fe to Mg (Figure 32). Phenocrysts were heavily to moderately fractured, with fractures occurring primarily at 90˚ for one, and at ~120˚ and ~˚60 for the other clast. One of the phases contained a lath shaped inclusion, about 5 µm long, growing at the centre of the grain (Figure 33). Qemscan identified this as an unknown Fe-oxide phase. BSE images revealed compositional zoning and small to large grainsize sorting in the matrix surrounding the clasts. There were abundant Fe-oxides in the matrix surrounding the clast.

Augite phenocrysts were represented by one sample (Figure 34). Phenocrysts were lightly fractured. There was core to rim zoning (Fe to Mg). The representative sample contained scattered oxide inclusions that increased in quantity towards the rim. Clast edges were well defined, however, BSE images showed compositional zoning, and grainsize zoning (small to large, away from clast) in the matrix encapsulating the clast.

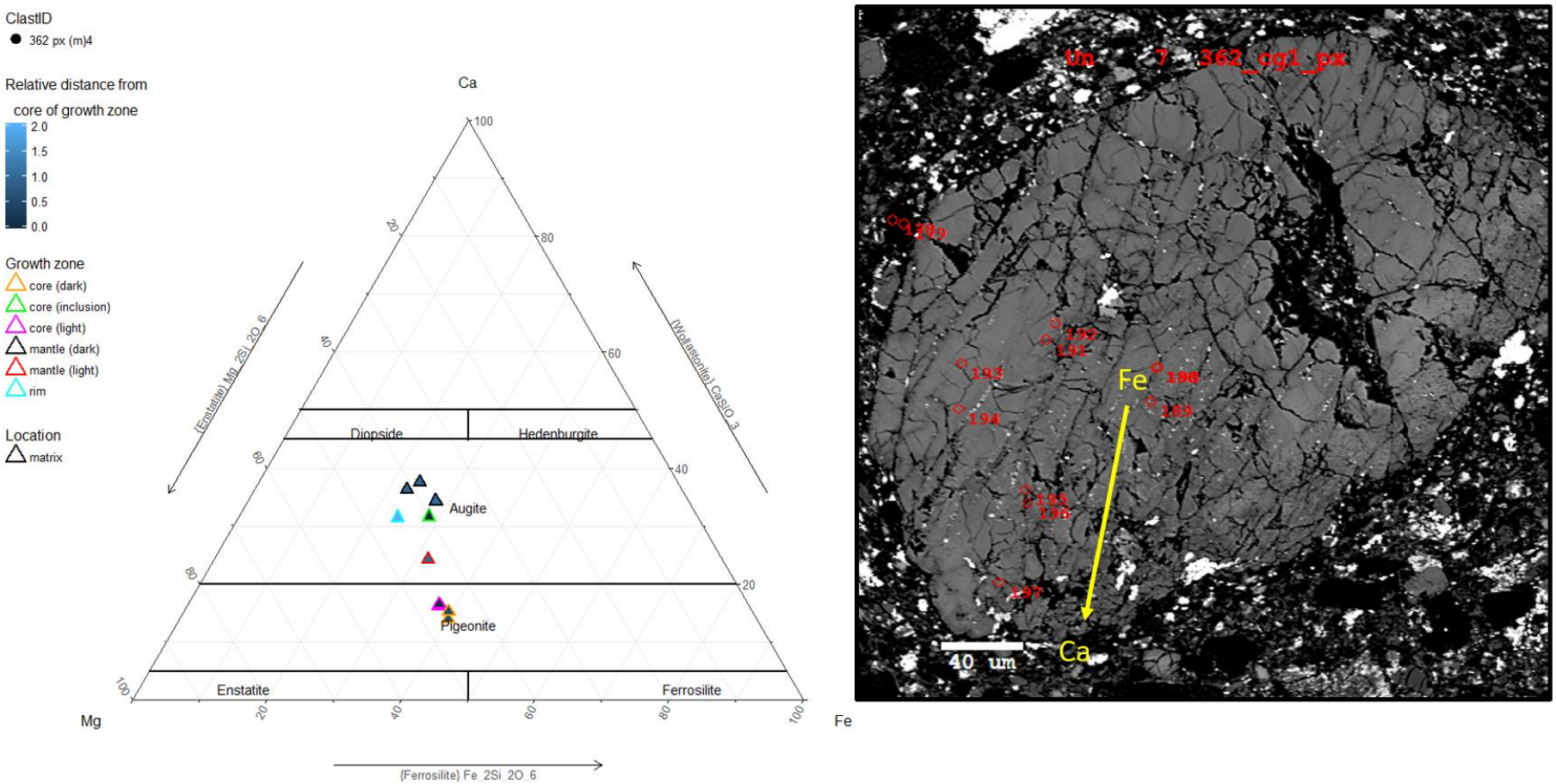

Figure 25: (Left) Pyroxene composition of phenocryst with lamellar intergrowth a (pigeonite-augite). Note lamellae in two directions, based on normalized proportions of Mg, Ca and Fe. Grid represents areas of stability for the separate pyroxene components. Blue bar denotes relative distance from core of growth zone, with 0.0 (dark blue) representing the core, and 2.0 (light blue) representing the rim. Shape denotes clast location (matrix or impact melt clast). (Right) BSE image with electron microprobe sampling points (red) and zoning direction (yellow arrow).

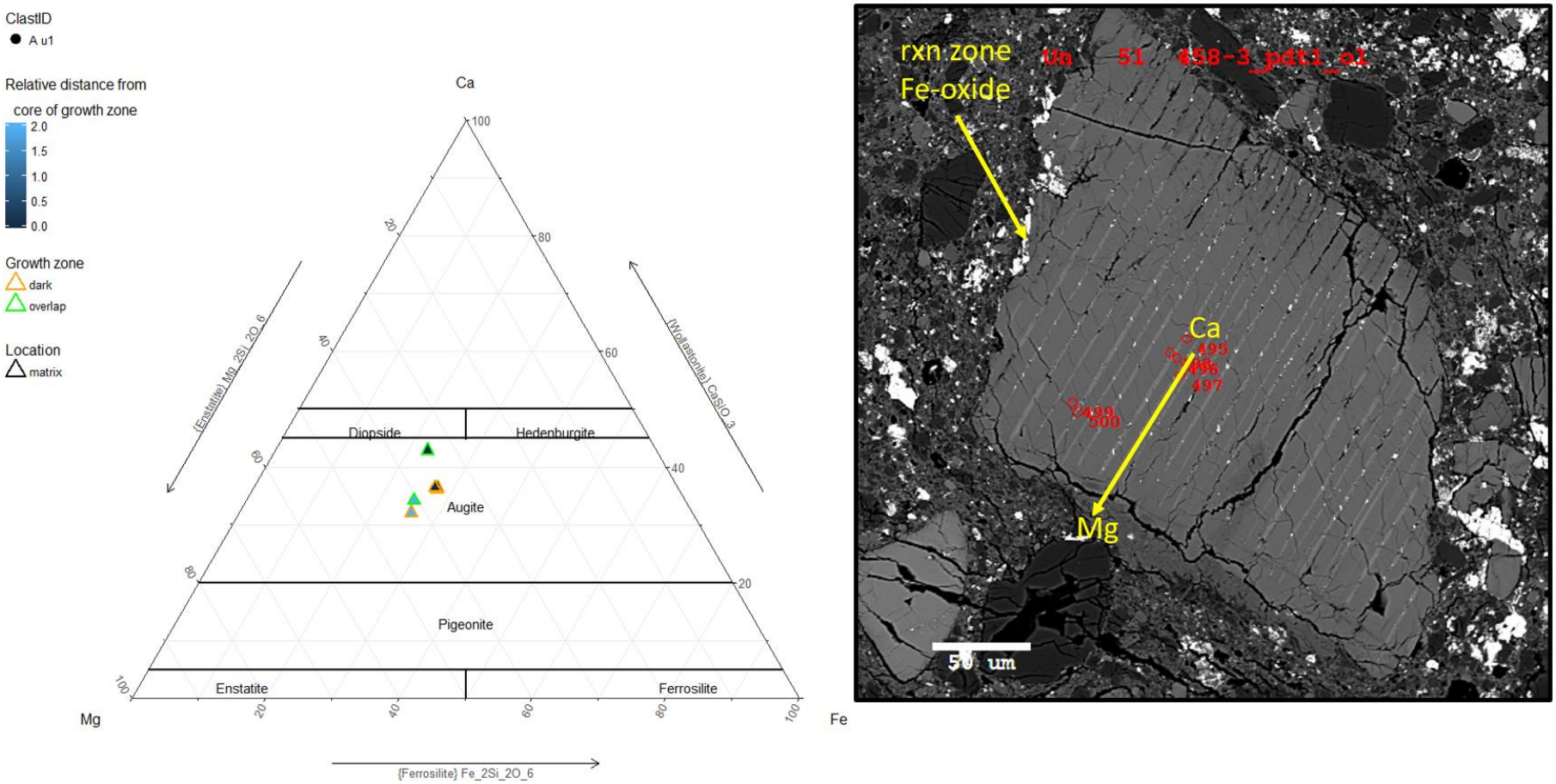

Figure 26: (Left) Pyroxene composition of phenocryst with lamellar intergrowth b (low- and high Ca augite), based on normalized proportions of Mg, Ca and Fe. Grid represents areas of stability for the separate pyroxene components. Blue bar denotes relative distance from core of growth zone, with 0.0 (dark blue) representing the core, and 2.0 (light blue) representing the rim. Shape denotes clast location (matrix or impact melt clast). (Right) BSE image with electron microprobe sampling points (red) and zoning direction (yellow arrow).

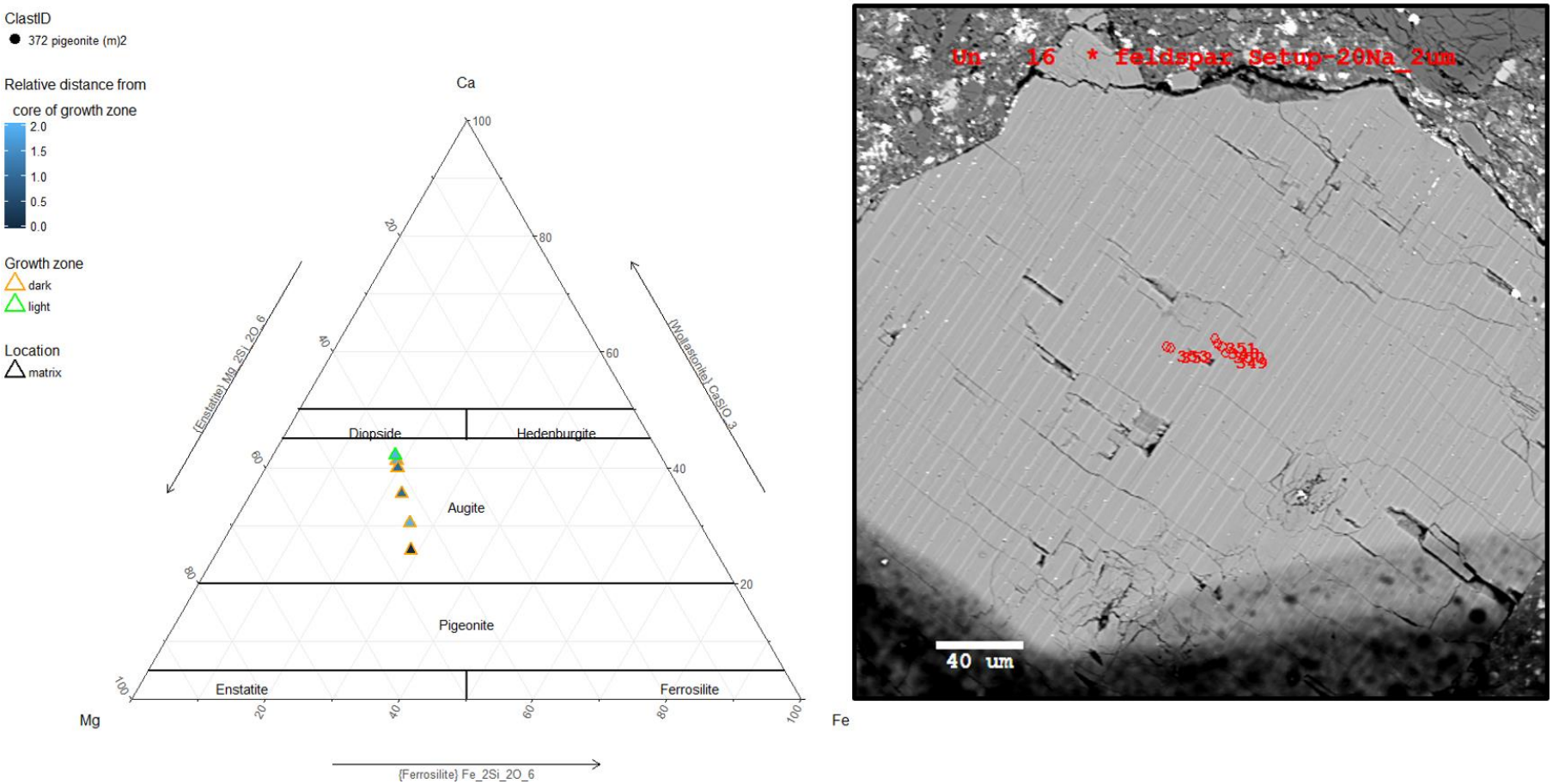

Figure 27: (Left) Pyroxene composition of phenocryst with lamellar intergrowth b (low- and high Ca augite), based on normalized proportions of Mg, Ca and Fe. Grid represents areas of stability for the separate pyroxene components. Blue bar denotes relative distance from core of growth zone, with 0.0 (dark blue) representing the core, and 2.0 (light blue) representing the rim. Shape denotes clast location (matrix or impact melt clast). (Right) BSE image with electron microprobe sampling points (red).

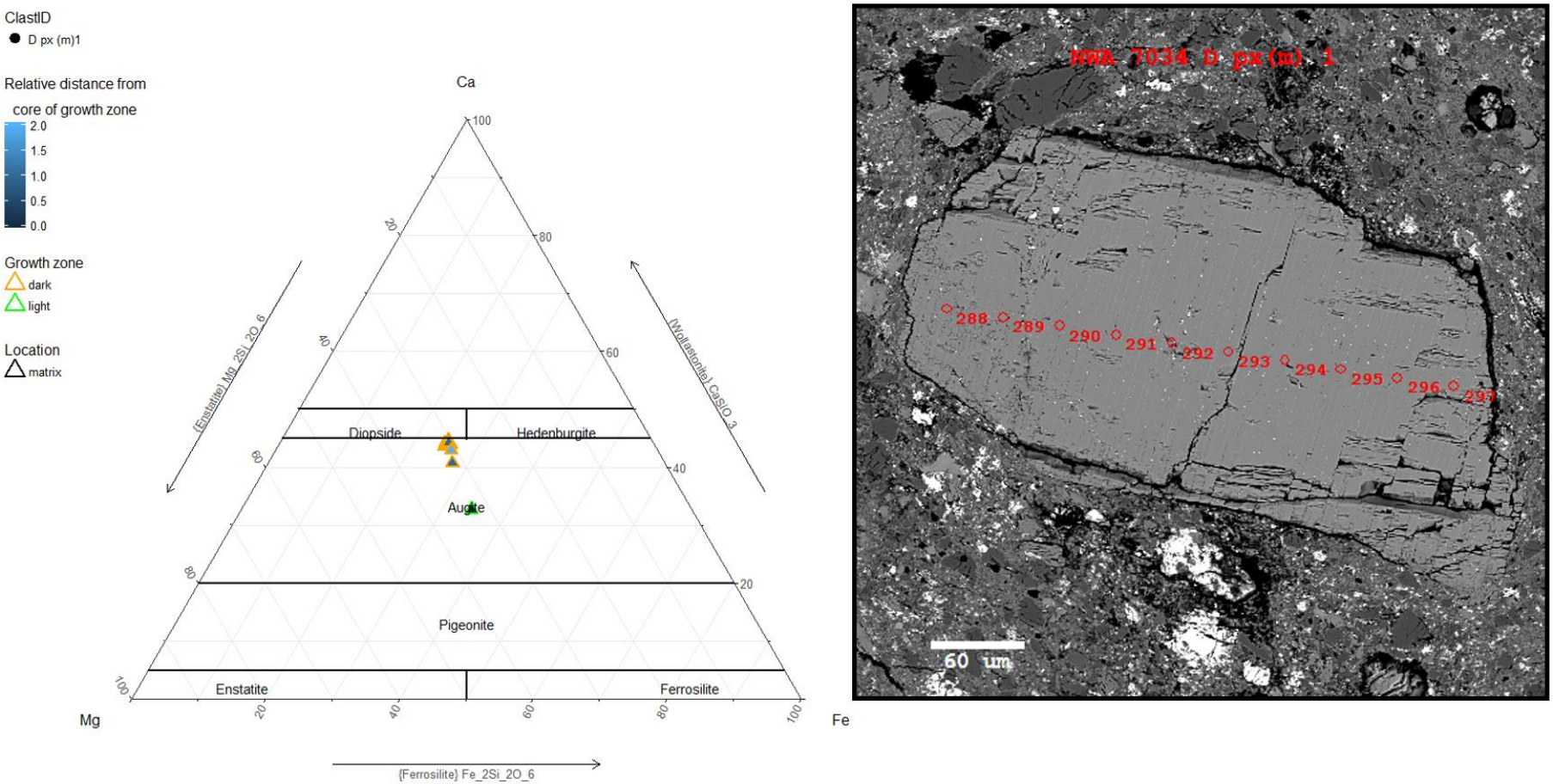

Figure 28: (Left) Pyroxene composition of phenocryst with lamellar intergrowth b (low- and high Ca augite), based on normalized proportions of Mg, Ca and Fe. Grid represents areas of stability for the separate pyroxene components. Blue bar denotes relative distance from core of growth zone, with 0.0 (dark blue) representing the core, and 2.0 (light blue) representing the rim. Shape denotes clast location (matrix or impact melt clast). (Right) BSE image with electron microprobe sampling points (red).

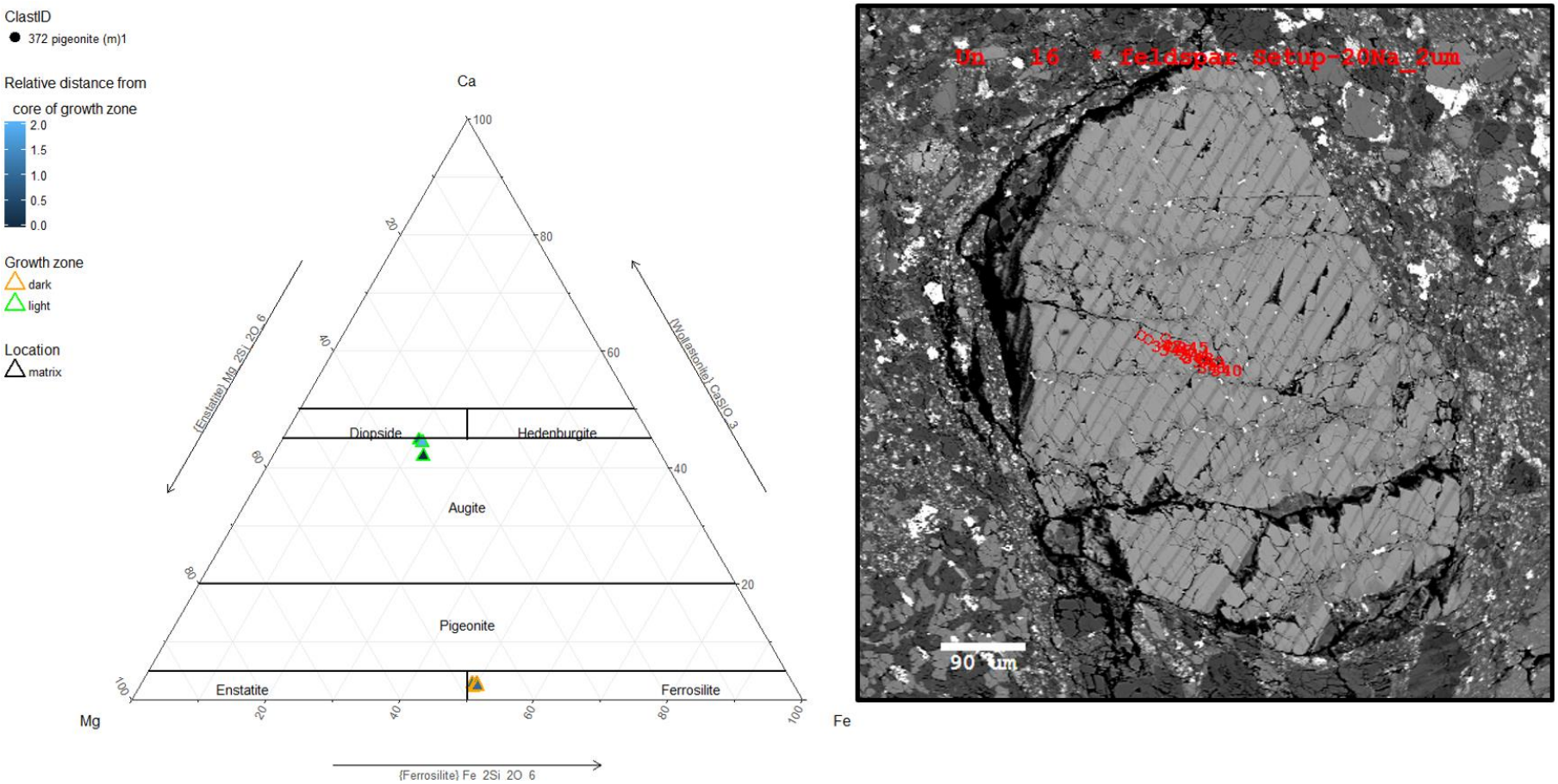

Figure 29: (Left) Pyroxene composition of phenocryst with lamellar intergrowth c (augite with orthopyroxene). Note two-directional lamellae. Based on normalized proportions of Mg, Ca and Fe. Grid represents areas of stability for the separate pyroxene components. Blue bar denotes relative distance from core of growth zone, with 0.0 (dark blue) representing the core, and 2.0 (light blue) representing the rim. Shape gives clast location (matrix or impact melt clast). (Right) BSE image with electron microprobe sampling points (red).

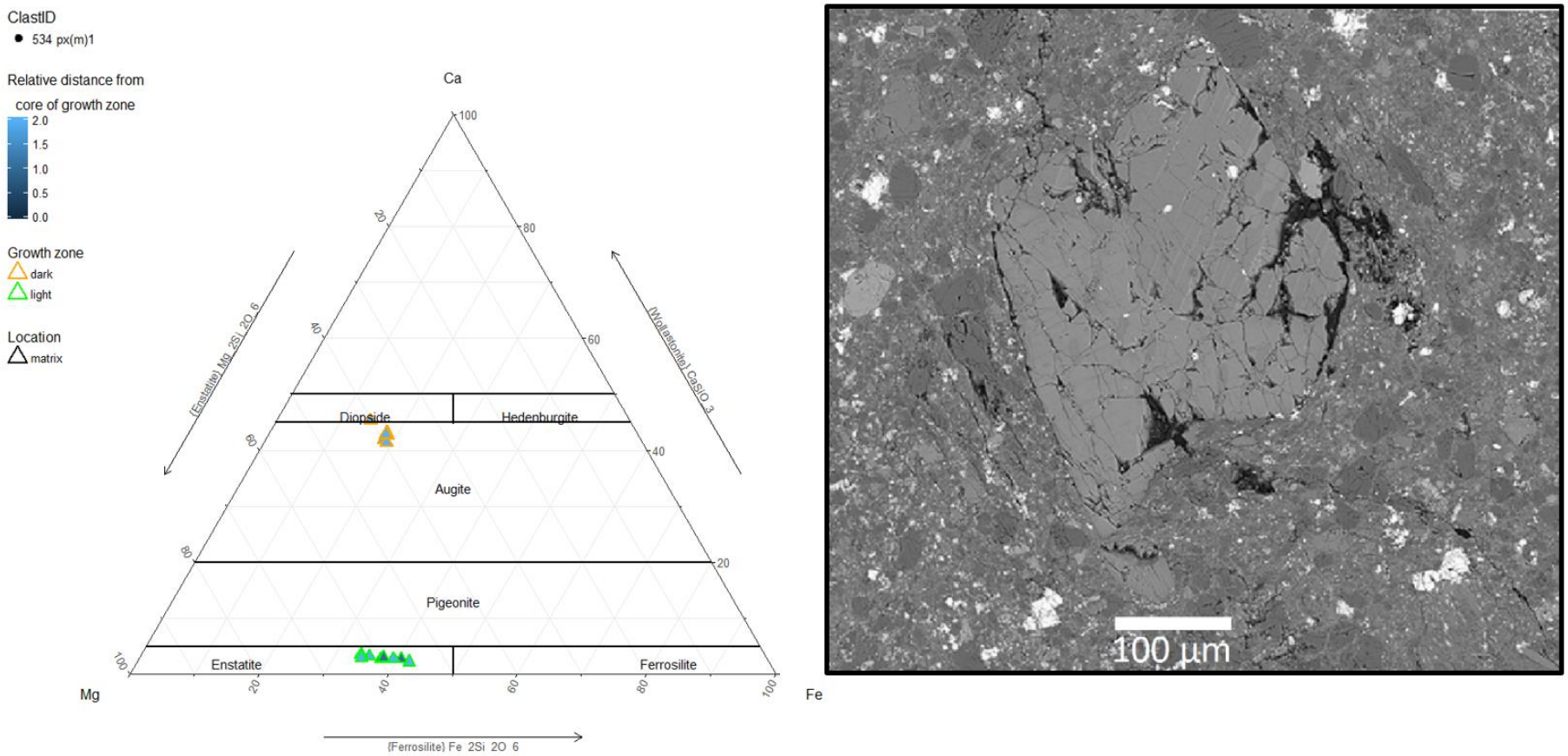

Figure 30: (Left) Pyroxene composition of phenocryst with lamellar intergrowth c (augite with ferrosilite). Note two-directional lamellae. Based on normalized proportions of Mg, Ca and Fe. Grid represents areas of stability for the separate pyroxene components. Blue bar denotes relative distance from core of growth zone, with 0.0 (dark blue) representing the core, and 2.0 (light blue) representing the rim. Shape denotes clast location (matrix or impact melt clast). (Right) BSE image.

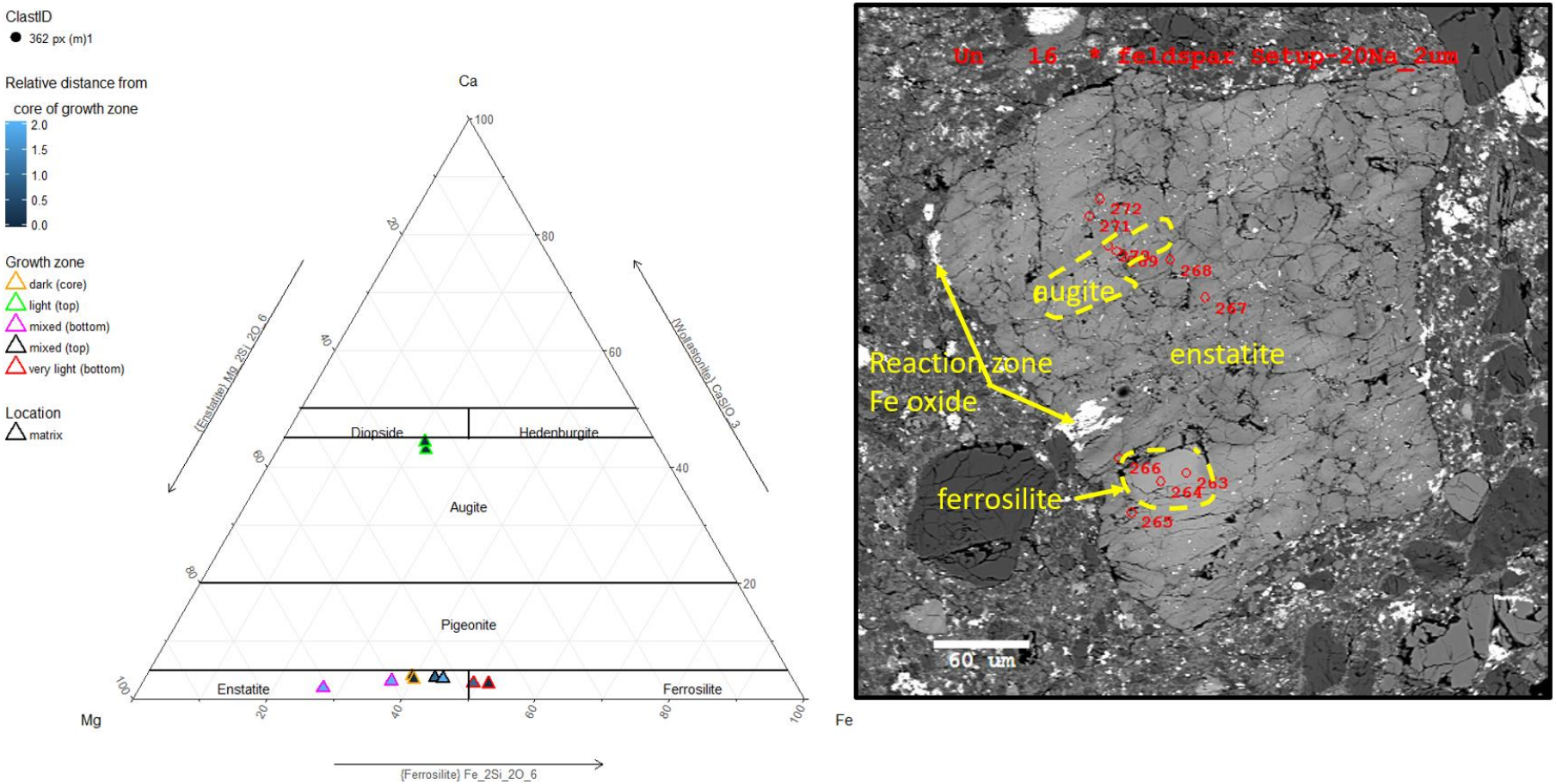

Figure 31: (Left) Pyroxene composition of enstatite with intergrowths of ferrosilite and augite, based on normalized proportions of Mg, Ca and Fe. Grid represents areas of stability for the separate pyroxene components. Blue bar denotes relative distance from core of growth zone, with 0.0 (dark blue) representing the core, and 2.0 (light blue) representing the rim. Shape denotes clast location (matrix or impact melt clast). (Right) BSE image with electron microprobe sampling points (red) and zoning direction (yellow arrow).

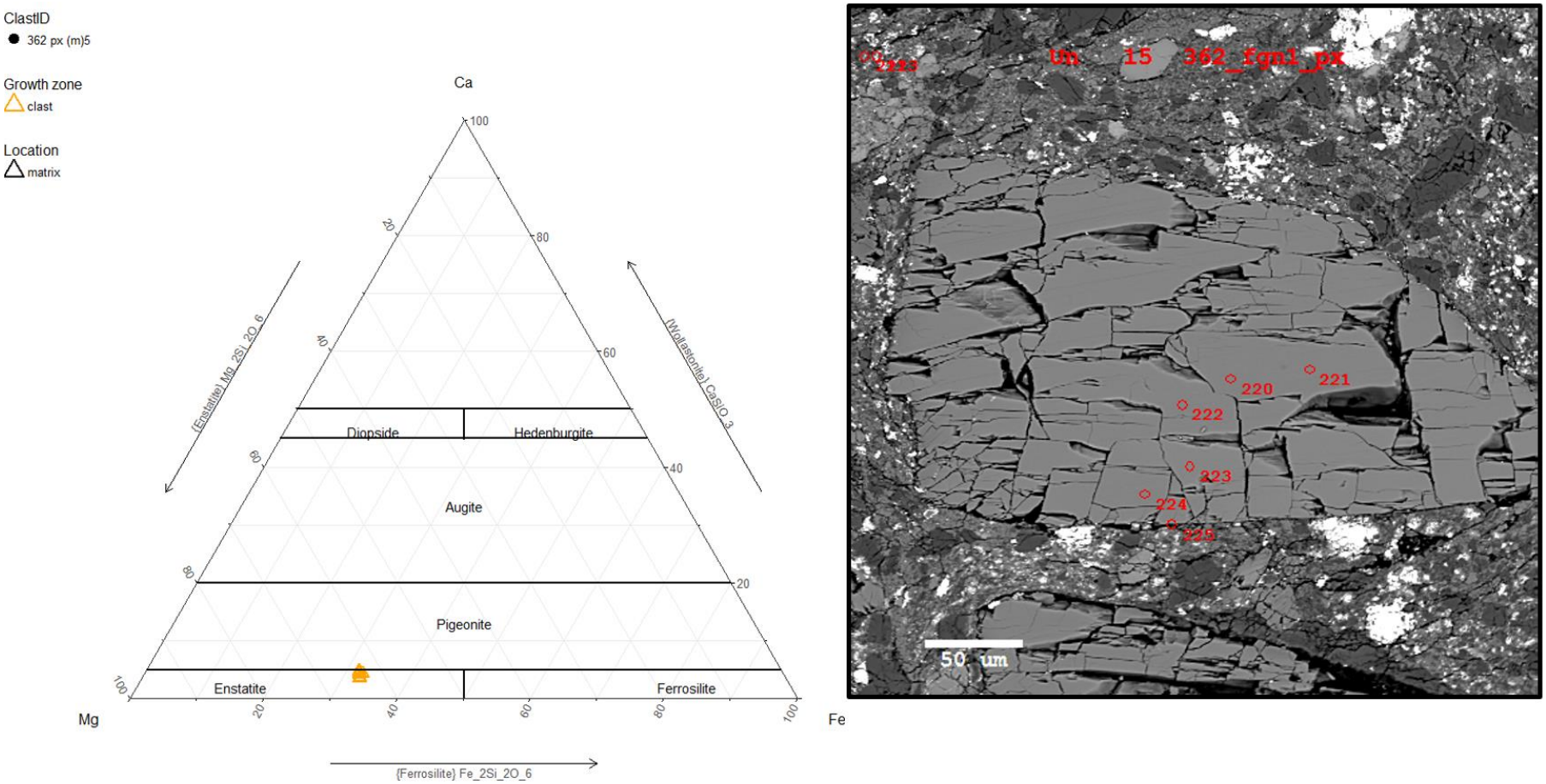

Figure 32: (Left) Pyroxene composition of enstatite phenocryst, based on normalized proportions of Mg, Ca and Fe. Grid represents areas of stability for the separate pyroxene components. Shape denotes clast location (matrix or impact melt clast). (Right) BSE image with electron microprobe sampling points (red).

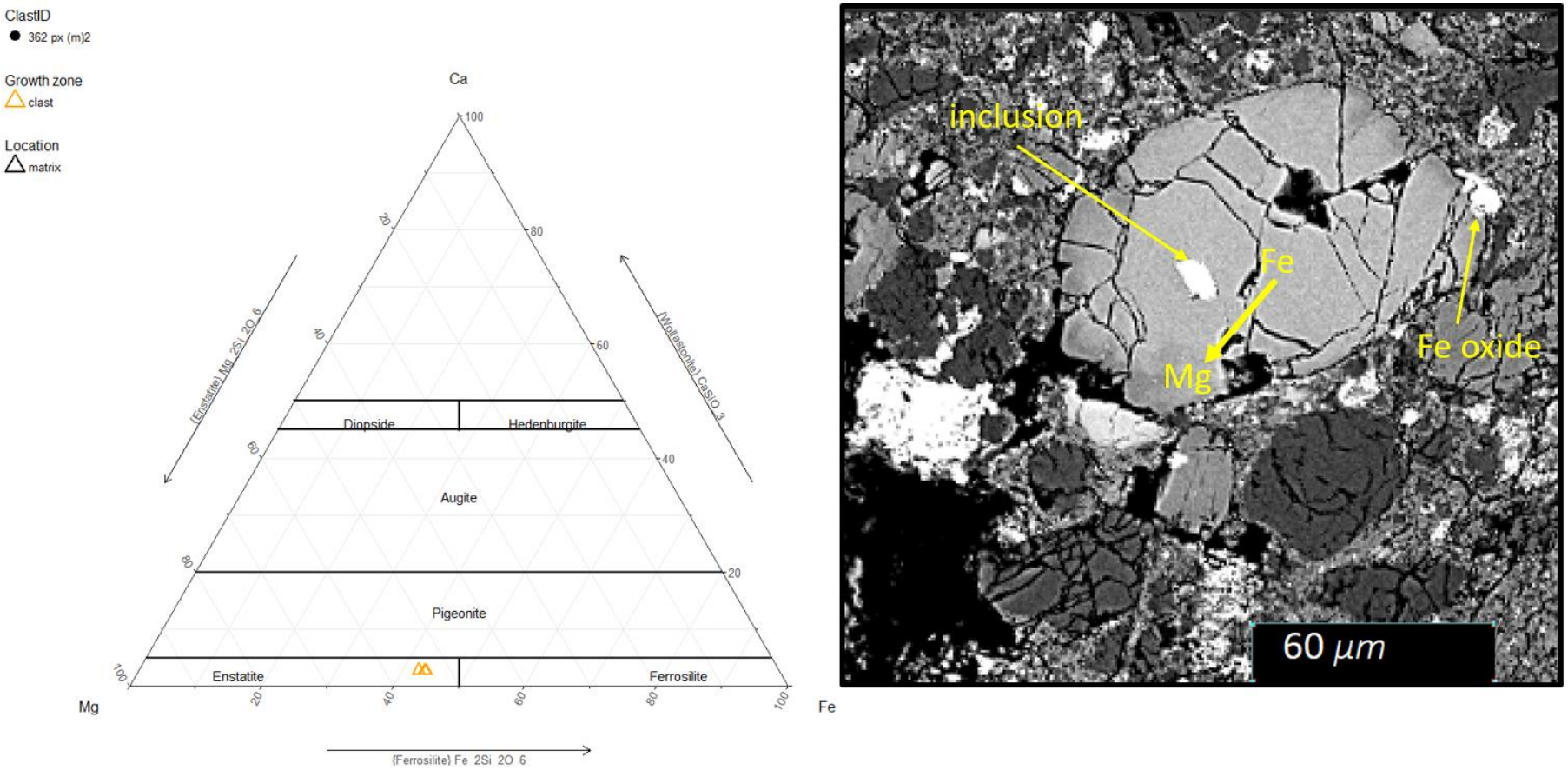

Figure 33: (Left) Pyroxene composition of enstatite phenocryst, based on normalized proportions of Mg, Ca and Fe. Grid represents areas of stability for the separate pyroxene components. Shape gives clast location (matrix or impact melt clast). (Right) BSE image with zoning direction (yellow arrow).

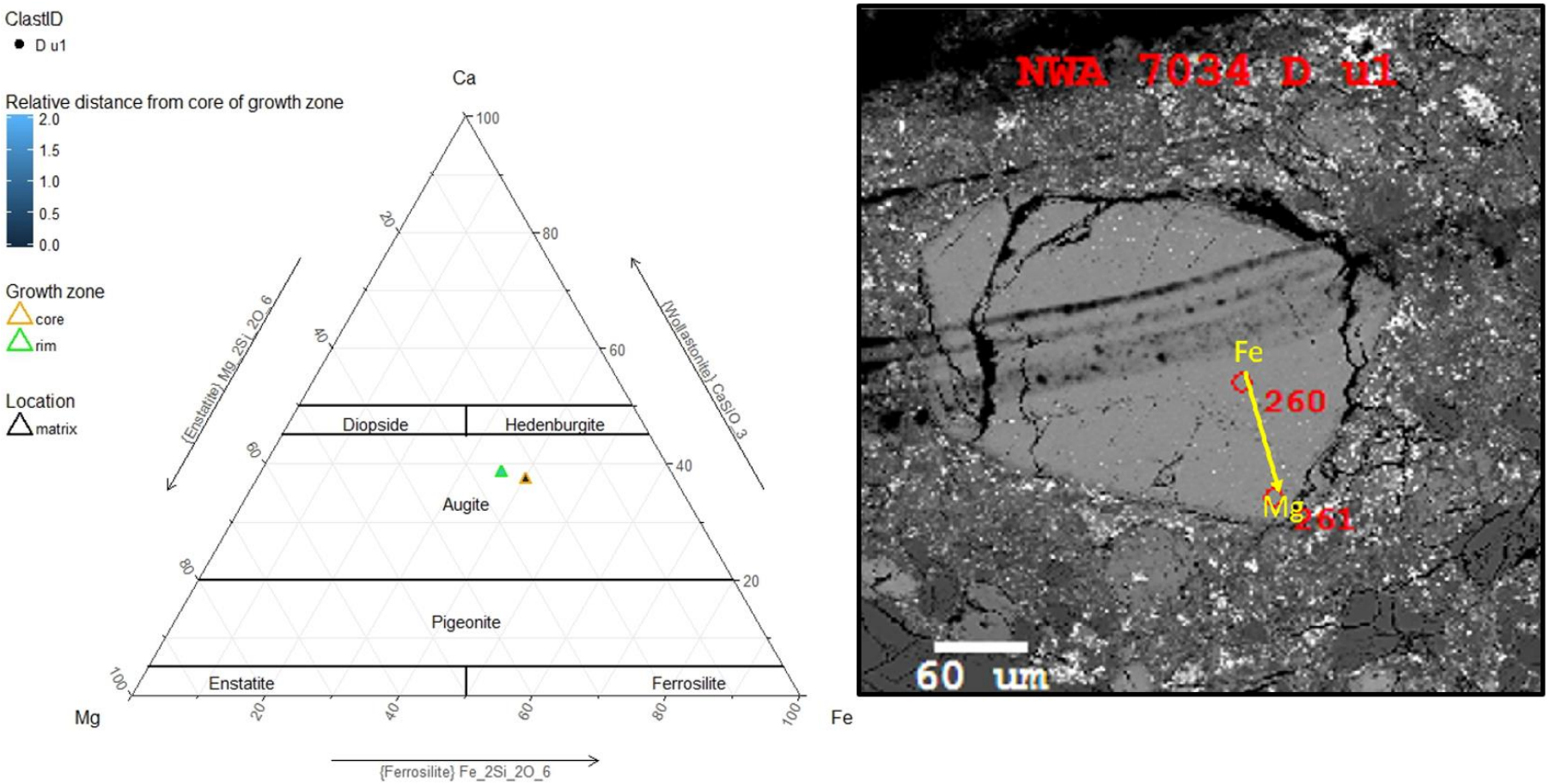

Figure 34: (Left) Pyroxene composition of augite phenocryst, based on normalized proportions of Mg, Ca and Fe. Grid represents areas of stability for the separate pyroxene components. Blue bar denotes relative distance from core of growth zone, with 0.0 (dark blue) representing the core, and 2.0 (light blue) representing the rim. Shape denotes clast location (matrix or impact melt clast). (Right) BSE image with electron microprobe sampling points (red) and zoning direction (yellow arrow).

Pyroxene phenocrysts found in impact melt clasts were distinguished from the matrix phenocrysts, as they denote an older age (Udry *et al.,* 2014). Three of these could successfully be sampled by microprobe. Two were sampled from mount D in close proximity to each other, the other from mount A. Pyroxenes were grouped into sub-types, based on their defining zoning patterns and composition. Two sub-types were observed: enstatite phenocryst and enstatite phenocryst with Mg-exsolution (Table 7).

Table 7: Pyroxene types with their defining characteristic composition and -textures, and zoning patterns (from core to rim of spherule) and associated samples.

Classification	*Defining characteristics*	*Growth textures*	*Zoning in pyroxene*	*Representative sample(s)*
Lamellar enstatite	Sub-angular phenocryst, lamellar intergrowth of Mg-rich phase	Exsolution lamellae, patchy, core to rim	exsolution lamellae (Mg-rich) and core to rim (Fe to Mg)	D px (c)1, D px (c)2
Enstatite	Sub-angular phenocryst	Core to rim	Core to rim (Mg to Fe)	A px (m)2

The clasts had a vaguely trapezoidal shape with well-defined edges and were classed as sub-angular to sub-rounded. Both were heavily fractured. In one of the clasts, microfractures intersected primarily at 90˚ to Mg-rich lamellae (Figure 35). In the other, fractures intersected at 90˚, and 120˚ and 60˚ angles (Figure 36). Electron microprobing determined that all three phenocrysts were Enstatites. They were compositionally close, all in the 32-40 % Fe, and 60-65 % Mg range, with low <5% Ca. Core to rim zoning was present in two of the clasts. For the clast from mount D, the core was enriched in Fe (5.5 ± 0.5 %) relative to the rim (Figure 36). Samples taken from the rim in both D clasts had similar Mg content (65.0 ± 0.5 %). The clast from mount A exhibited the opposite zoning pattern, where the core was enriched in Mg relative to the rim, which was higher in Fe (Figure 37). There was a Fe oxide inclusion at the centre of one of the clasts (Figure 36).

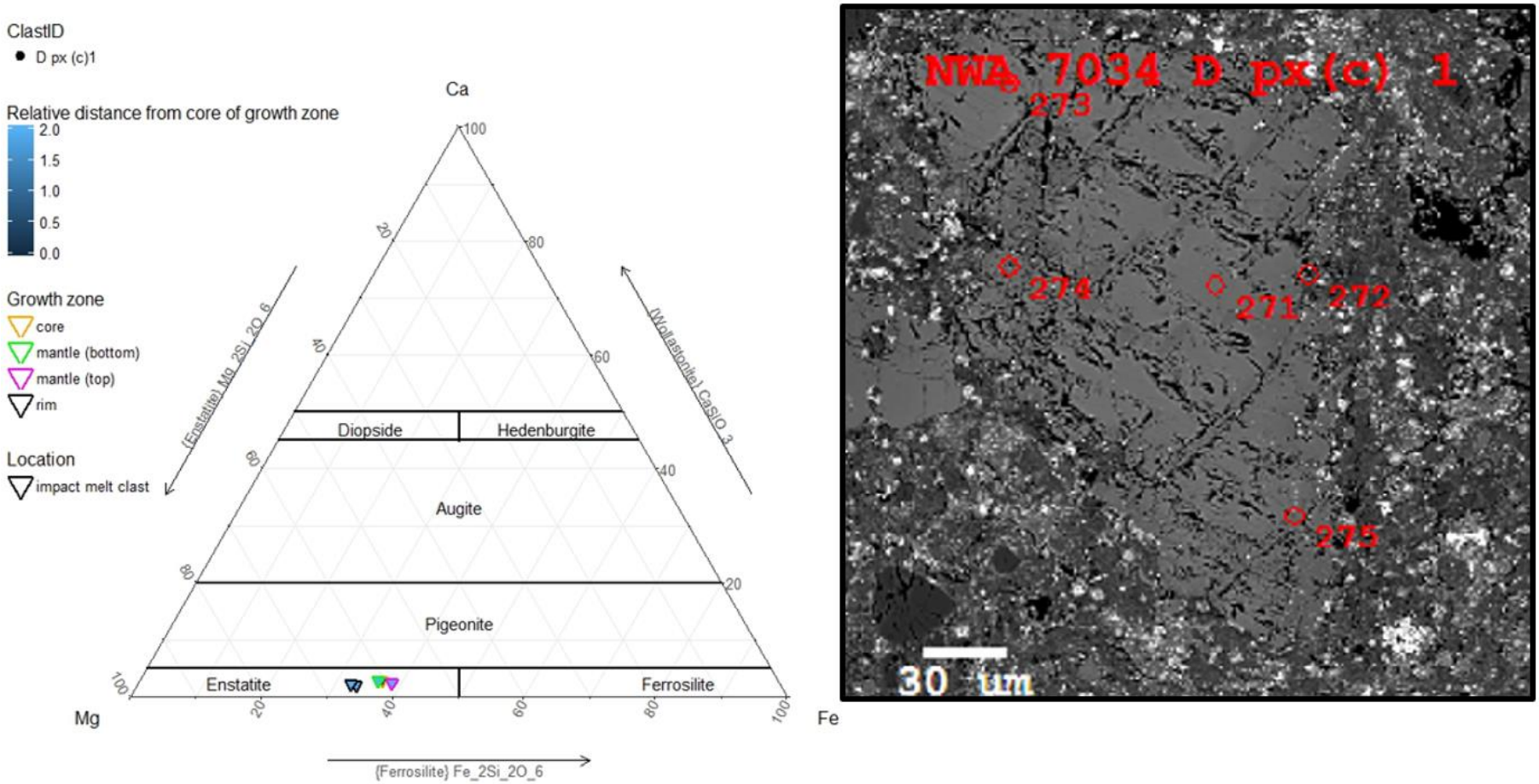

Figure 35: (Left) Pyroxene composition of lamellar enstatite phenocryst, based on normalized proportions of Mg, Ca and Fe. Grid represents areas of stability for the separate pyroxene components. Blue bar denotes relative distance from core of growth zone, with 0.0 (dark blue) representing the core, and 2.0 (light blue) representing the rim. Coloured outlines are used to give more detailed information about the sampling location within the clast. Shape denotes clast location (matrix or impact melt clast). (Right) BSE image with electron microprobe sampling points (red) and zoning direction (yellow arrow).

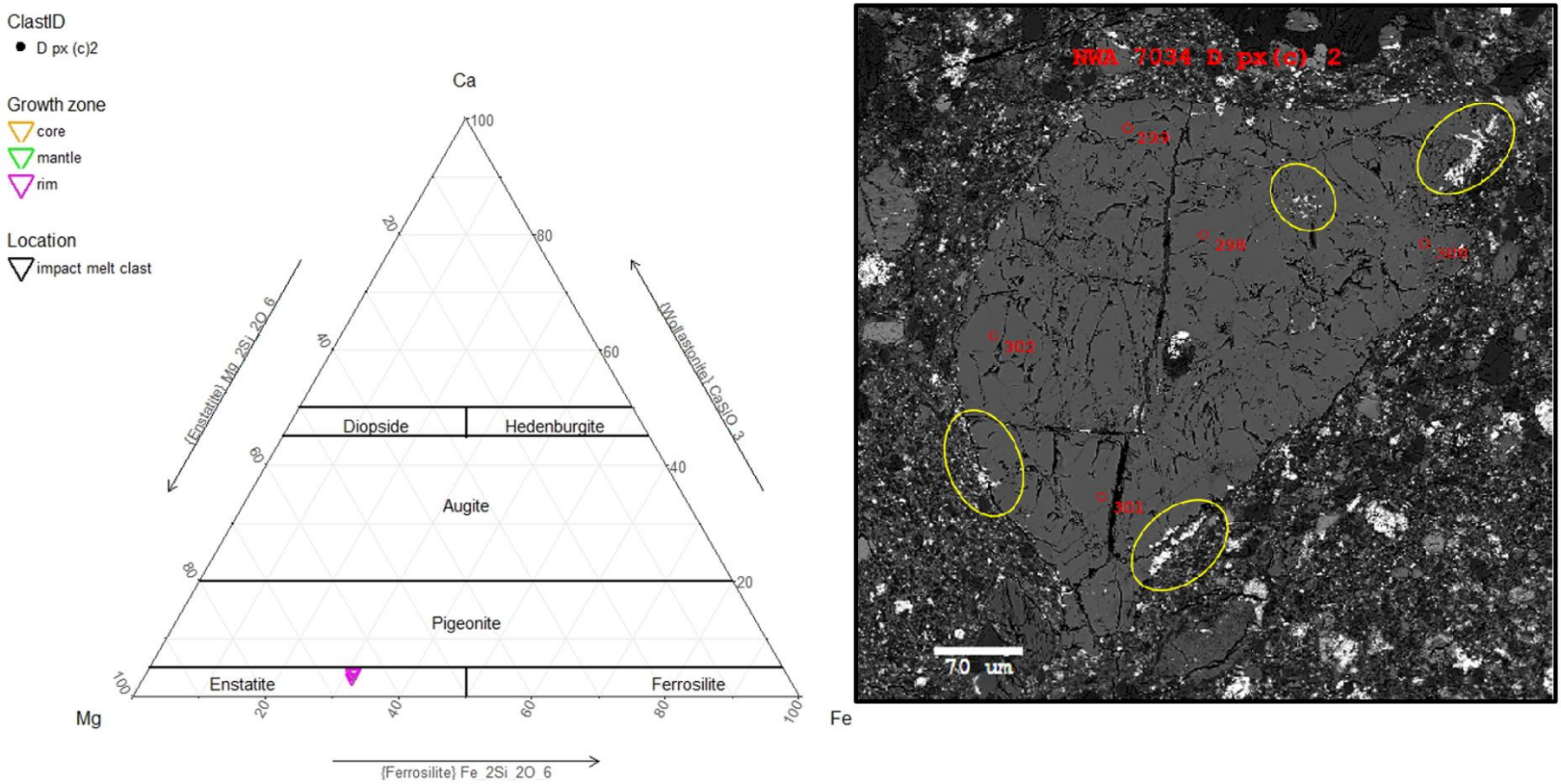

Figure 36: (Left) Pyroxene composition of lamellar enstatite phenocryst, based on normalized proportions of Mg, Ca and Fe. Grid represents areas of stability for the separate pyroxene components. Coloured outlines are used to give more detailed information about the sampling location within the clast. Shape denotes clast location (matrix or impact melt clast). (Right) BSE image with electron microprobe sampling points (red) and zoning direction (yellow arrow).

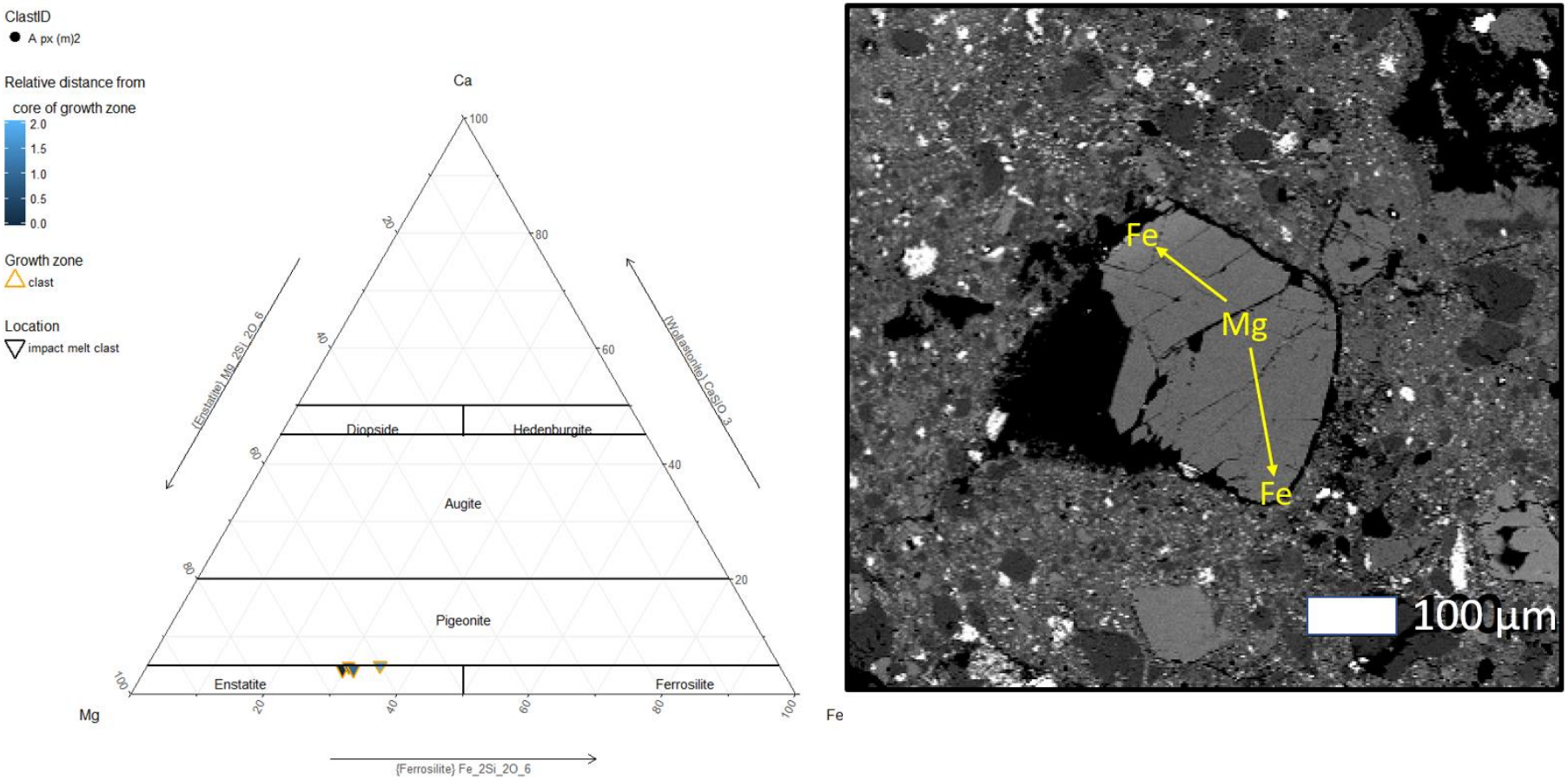

Figure 37: (Left) Pyroxene composition of enstatite phenocryst, based on normalized proportions of Mg, Ca and Fe. Grid represents areas of stability for the separate pyroxene components. Blue bar denotes relative distance from core of growth zone, with 0.0 (dark blue) representing the core, and 2.0 (light blue) representing the rim. Shape denotes clast location (matrix or impact melt clast). (Right) BSE image with zoning direction (yellow arrows).

3.3 GABBROIC CLASTS

Gabbroic clasts were grouped, based on their defining zoning patterns and composition. A norite-pyroxenite, gabbronorites, apatite-plagioclase(-ilmenite) clasts, and gabbros were identified. Table 8 lists the sub-types observed. Unlike for single mineral clasts, in-grain variation was for the most part negligible (<5%) in polymineralic clasts.

Table 8: gabbroic clast types with their defining characteristic composition and -textures, and zoning patterns (from core to rim of spherule) and associated samples.

Type		*Defining characteristics*	*Growth textures*	*Zoning in pyroxene*	*Zoning in plagioclase*	*Representative sample(s)*
Norite-pyroxenite		norite joint to orthopyroxenite at clearly defined boundary	equigranular grains of feldspar and enstatite in norite; feldspar embayed in pyroxene in pyroxenite	Highest in Mg near boundary, highest in K near clast rim; core to rim of grain (Fe to Mg)	highest in Ca near boundary, highest in K near clast rim; core to rim of grain (K to Na)	D N1
Gabbronorite	*a*	intergrowths of orthopyroxene (enstatite, pigeonite) and feldspar (albite)	equigranular, microcrystalline	core to rim (Mg to Fe; Fe to Mg; Mg, Fe to Ca)	core to rim (Na to Ca; Ca to K in B fg2 and 458-3 fg1)	A cg2, A fg1, B fg1, B fg2, D fg2, 362 fg1, 362 cg1, 372 cg1, 458-3 fg1,
	b	intergrowth of orthopyroxene and feldspar (very fine grained, average grain <10 µm)	porphyritic, cryptocrystalline, lath	within clast (Fe to Mg), core to rim of grain (Fe to Mg)	core to rim (Na to Ca)	A fg2
	c	lath grained intergrowth of orthopyroxene and feldspar (albite and orthoclase)	primarily lath, secondarily globular and/or equigranular	core to rim of clast (Fe to Mg; Ca to Mg)	traversing clast (Na to Ca); within lath grains (Na - K)	372 lg1
	d	intergrowth of pyroxene and feldspar	microcrystalline, rounded inclusions; twinning and lamellae in pyroxene	Lamellar, core to rim (Fe to Ca)	None	D cg 1
Apatite-plagioclase(-ilmenite)		intergrowth of apatite with feldspar and/or pyroxene, often contains ilmenite	lath or equigranular,	no pyroxene present	core to rim (Ca to Na), alkali feldspar around apatite/ilmenite	A ipc1, D pc1, 362 pc1
Gabbro	*a*	intergrowth of augite and alkali feldspar	patchy and lath grains; lamellae in feldspar	core to rim (Ca to Mg), lath grain (Ca to Fe), underlying	Na – K, lamellae (higher in Ca)	362 cg2

			to overlying (Fe to Mg)		
b	lath grained intergrowth of augite and plagioclase (andesine, labradorite)	lath and equigranular	core to rim of clast (Ca to Mg), core to rim of grain (Mg to Ca)	core to rim (Na to Ca)	D lg1
c	intergrowth of augite and albite (andesine, oligoclase)	equigranular, microcrystalline	Ca, Mg, Fe	core to rim (Ca to Na)	A cg1, 362 fg2
d	<20% pyroxene	euhedral andesine grain with augite growth along one corner	Ca - Mg	core to rim (Ca to Na)	372 vcg1

3.3.1 Norite-pyroxenite

This unique clast only appeared once in all the mounts analysed. It was contained in the matrix. Its proportions were ~ 700 µm x 1300 µm and it had a rounded shape. What was characteristic about it, was that it was a pyroxenite joint to norite along a clearly defined boundary. The norite section was made up of equigranular grains of feldspar (albite and orthoclase) and orthopyroxene (enstatite). In the norite section, feldspar grains were embayed in the pyroxene. Both plagioclase and alkali feldspar were identified. Feldspar was highest in Ca and Na near the norite-pyroxenite boundary, making it an andesine albite, and increased in K towards the rim of the clast, where the K-feldspar sanidine was identified. Both were present in both the norite and pyroxenite sections but alkali felspar was more common in norite and plagioclase more common in pyroxenite. There was minor zoning in feldspar grains, cores were higher in K, whilst the rim was higher in Na. The enstatite displayed clear compositional changes traversing from norite to pyroxenite within their respective sections, however, there was no compositional difference between the two (Figure 38). In the pyroxenite, the composition of enstatite was higher in Fe away from the norite-pyroxenite boundary and increasing in Mg towards it. Whilst in the norite section, the enstatite was highest in Fe near the boundary and increased in Mg away from it. The enstatite with the highest Fe concentration was found in the norite section, near the norite-pyroxenite boundary (Figure 39). Grains in the pyroxenite section had core to rim zoning from Fe to Mg, however no grain zoning trend could be observed in the norite section. Composition of both feldspars and pyroxenes were similar in norite and pyroxenite sections, instead zoning was observed traversing the clast from core to rim.

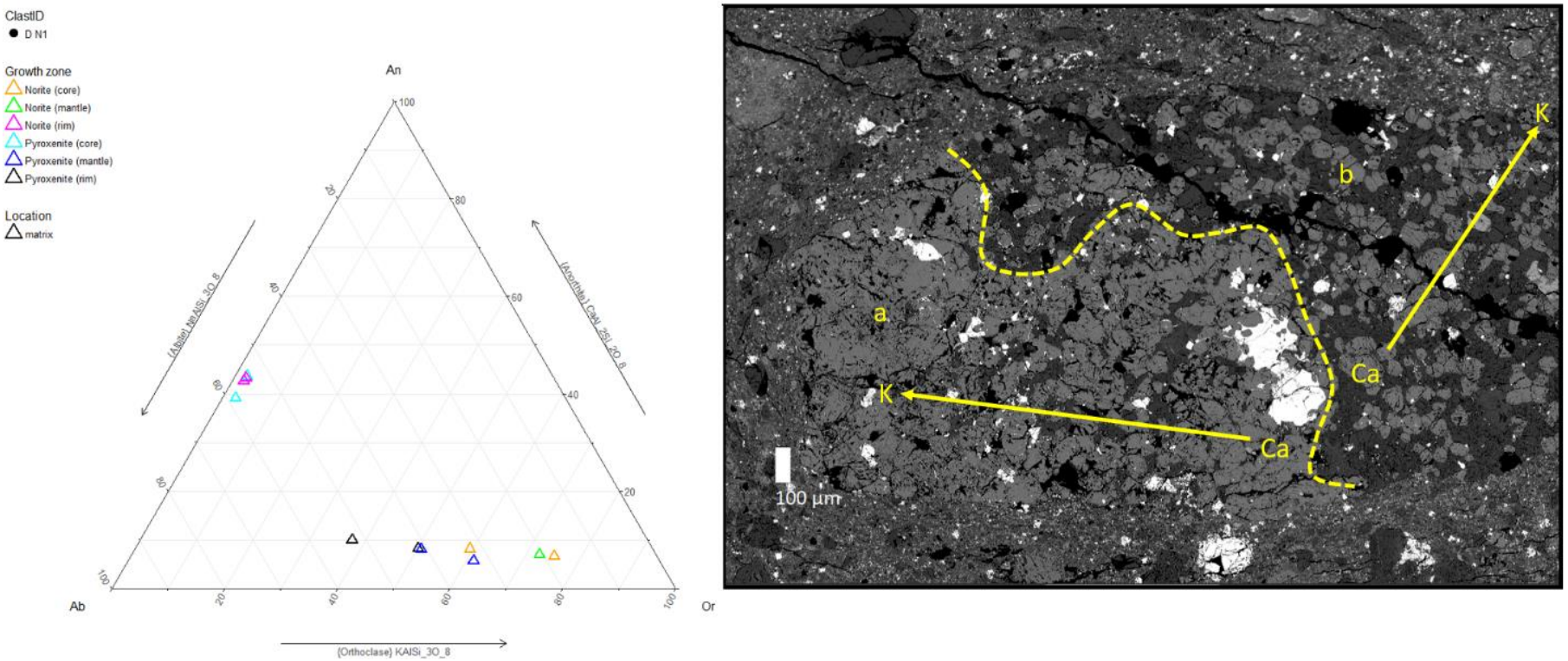

Figure 38: Composition of feldspar in norite-pyroxenite clast, based on normalized proportions of Na, Ca and K. Grid represents areas of stability for the separate feldspar components. Shape denotes clast location (matrix or impact melt clast). (Right) BSE image with zoning direction (yellow arrow). Dotted line represents boundary between pyroxenite (a) and norite (b).

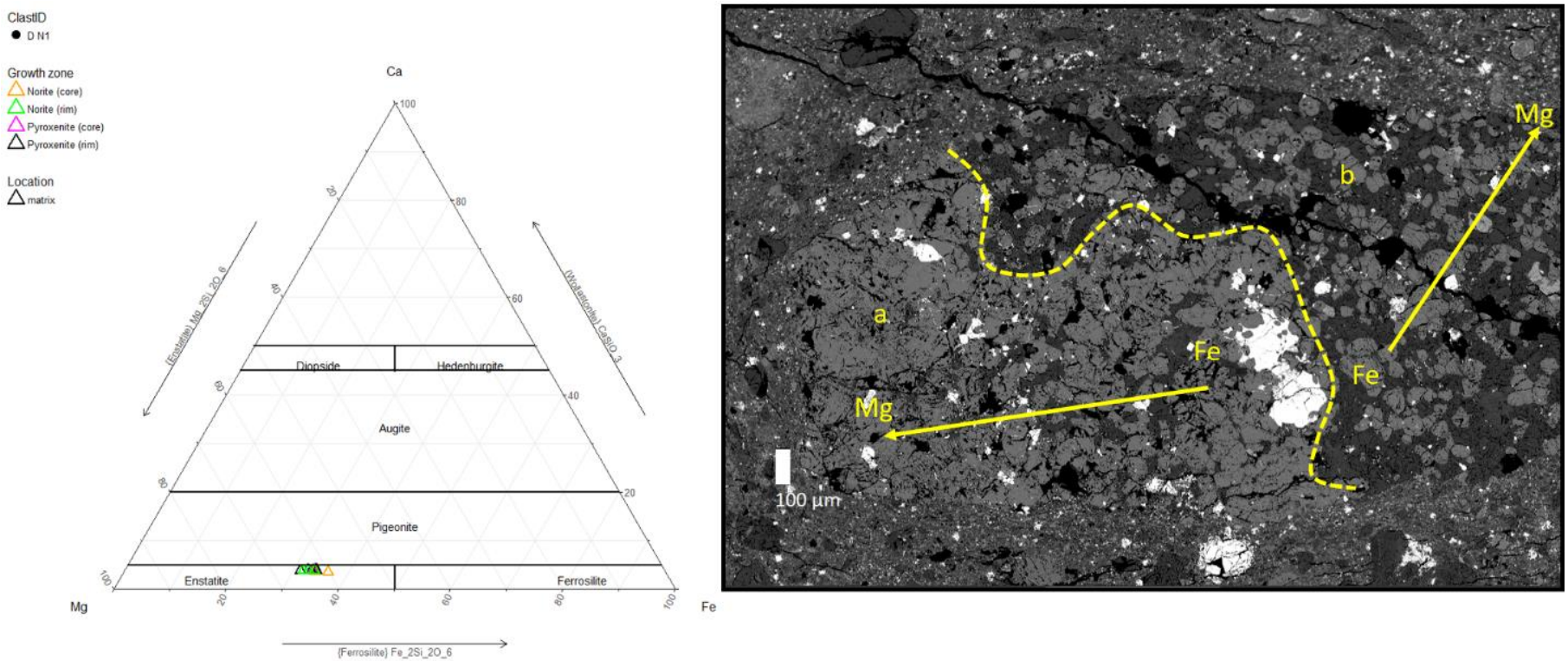

Figure 39: Pyroxene composition in norite-pyroxenite clast, based on normalized proportions of Mg, Ca and Fe. Grid represents areas of stability for the separate pyroxene components. Shape denotes clast location (matrix or impact melt clast). (Right) BSE image with zoning direction (yellow arrow). Dotted line represents boundary between pyroxenite (a) and norite (b).

3.3.2 Gabbronorite

All gabbronorites were defined by intergrowths of low Ca pyroxene and feldspar. Accessory Fe-oxides were common. *Gabbronorite a* was the most commonly found polymineralic clast type. It was characterised by equigranular intergrowth of feldspar and pyroxene at microcrystalline grainsize. Some clasts had accessory Fe-oxide, apatite, ilmenite. The plagioclase component was primarily andesine and oligoclase with core to rim zoning of Na to Ca. There was one instance of anorthoclase, in clast B fg2 (Figure 40). In-grain variation was negligible (<5%). Most of pyroxenes sampled were enstatites, some fell into the pigeonite range, and two were diopside and augite, in clasts that otherwise contained low Ca pyroxene. For most clasts, compositional range was larger in pyroxene than for plagioclase, with B fg2 having the widest. It was also the only clast with significant (>5%) in-grain compositional variation. There was no significant compositional difference between clasts from matrix and impact melt clasts. The plagioclase sampled from impact melt gabbronorite was andesine, with core to rim zoning from Na to Ca, same as in the matrix clasts. Pyroxene was composed of enstatite and diopside, in line with the matrix clasts. What made this clast special was that plagioclase, pyroxene and iron oxides were crosscut by a vein filled with an unknown mineral (Figure 41). This vein crosscut the clast and impact melt clast it was contained in, but not the matrix. The enstatite was compositionally zoned Mg to Fe and very low in Ca (<5%), however, the point sampled next to the vein had a more calcic component (54%) than all other sampling points.

Gabbronorite b was the second most common type of polymineralic clasts, it was characterised by its porphyritic texture and cryptocrystalline grainsize. While grainsize throughout most of the clast was averaging < 10 µm, some grains, particularly plagioclase and to a lesser extent pyroxene, had grown to be > 100 µm in size (Figure 42). These were often lath shaped. Gabbronorites of this type were found both the matrix and impact melt clasts. The pyroxene component was identified as enstatite, with minor (<5%) core to rim zoning in grains (Fe to Mg). There was not enough compositional variation (<10%) to claim zoning from core to rim of clast (Figure 43). Plagioclase had a larger compositional range, both labradorite and andesine were identified. However, only two sampling points yielded good totals, so it is impossible to make a statement about directional zoning within clasts of this type. The clast was rounded. The surrounding groundmass was porphyritic, cryptocrystalline and intergranular, making it hard to differentiate the clast from the groundmass.

Gabbronorite c had lath grains of plagioclase contained in anhedral pyroxene, with pyroxene lath grains of a different composition cross cutting both (Figure 45). There were poikilitic iron oxides scattered throughout. Pyroxene lath grains had a more ferric component, relative to the anhedral pyroxene. The anhedral pyroxene was strongly zoned, there was a 25% change in composition from core to rim (Ca to Mg; Figure 44). The plagioclase also had strong compositional variation, also, with lath grains varying in Na and K along the elongated plane, the highest K content was sampled at the clast rim. Additionally, plagioclase grains throughout the clast varied in composition. The sodic component was higher adjacent to the pyroxene. Clasts had elongated shapes with uneven clast boundaries. Clasts of similar composition were found in the nearby matrix.

Gabbronorite d was made of lamellar pyroxene (enstatite and pigeonite) that was twinned at 120˚. The twins had slightly different Ca and Fe compositions (Figure 47). There was plagioclase (sanidine) along the rim of the pyroxene and in the core, which exhibited no compositional zoning (Figure 46). Rounded and angular xenoliths of pyroxene were contained in plagioclase and pyroxene. Some plagioclase phenocrysts were separated from the clast by melt.

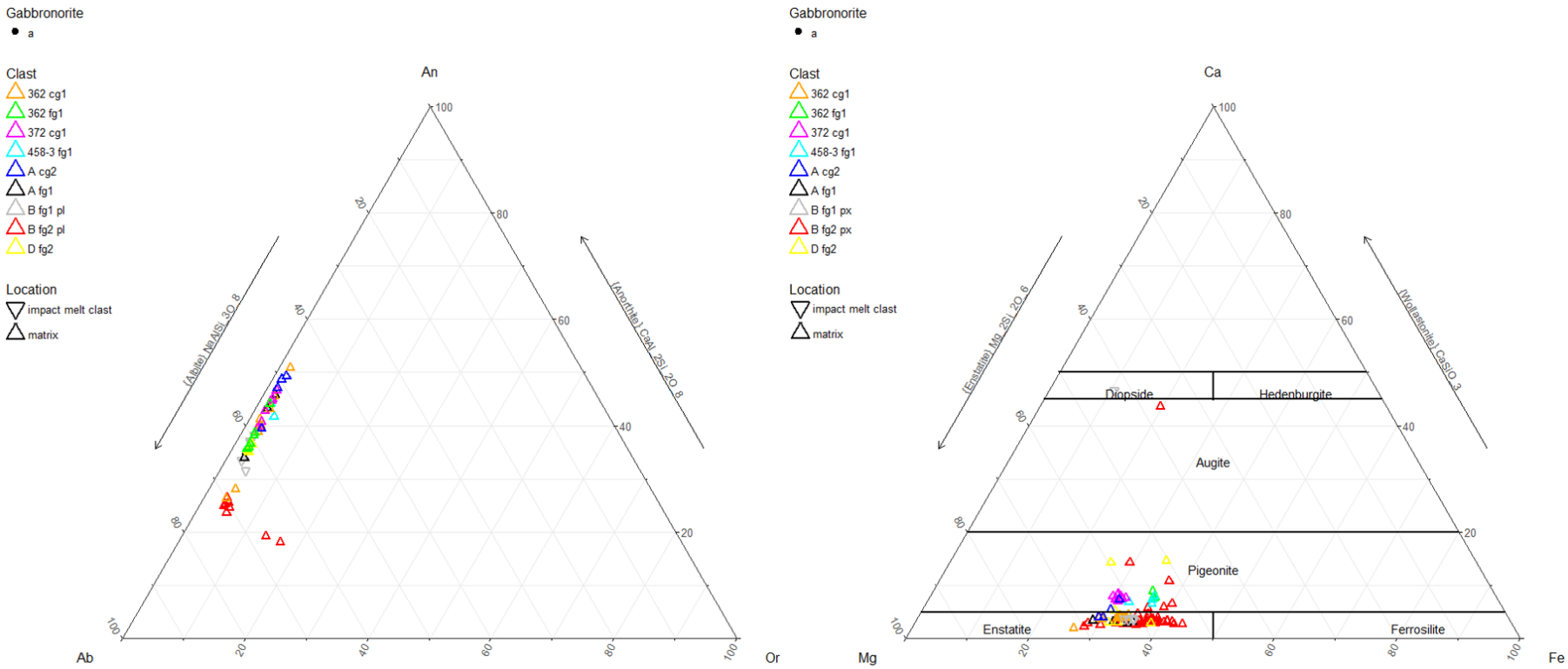

Figure 40: Composition of feldspars (left) and pyroxene (right), based on normalized proportions of Na, Ca, K (left), and Mg, Ca, Fe (right) in gabbronorite a clasts. Grid represents areas of stability for the separate pyroxene components. Shape denotes clast location (matrix or impact melt clast). Shape denotes clast location (matrix or impact melt clast).

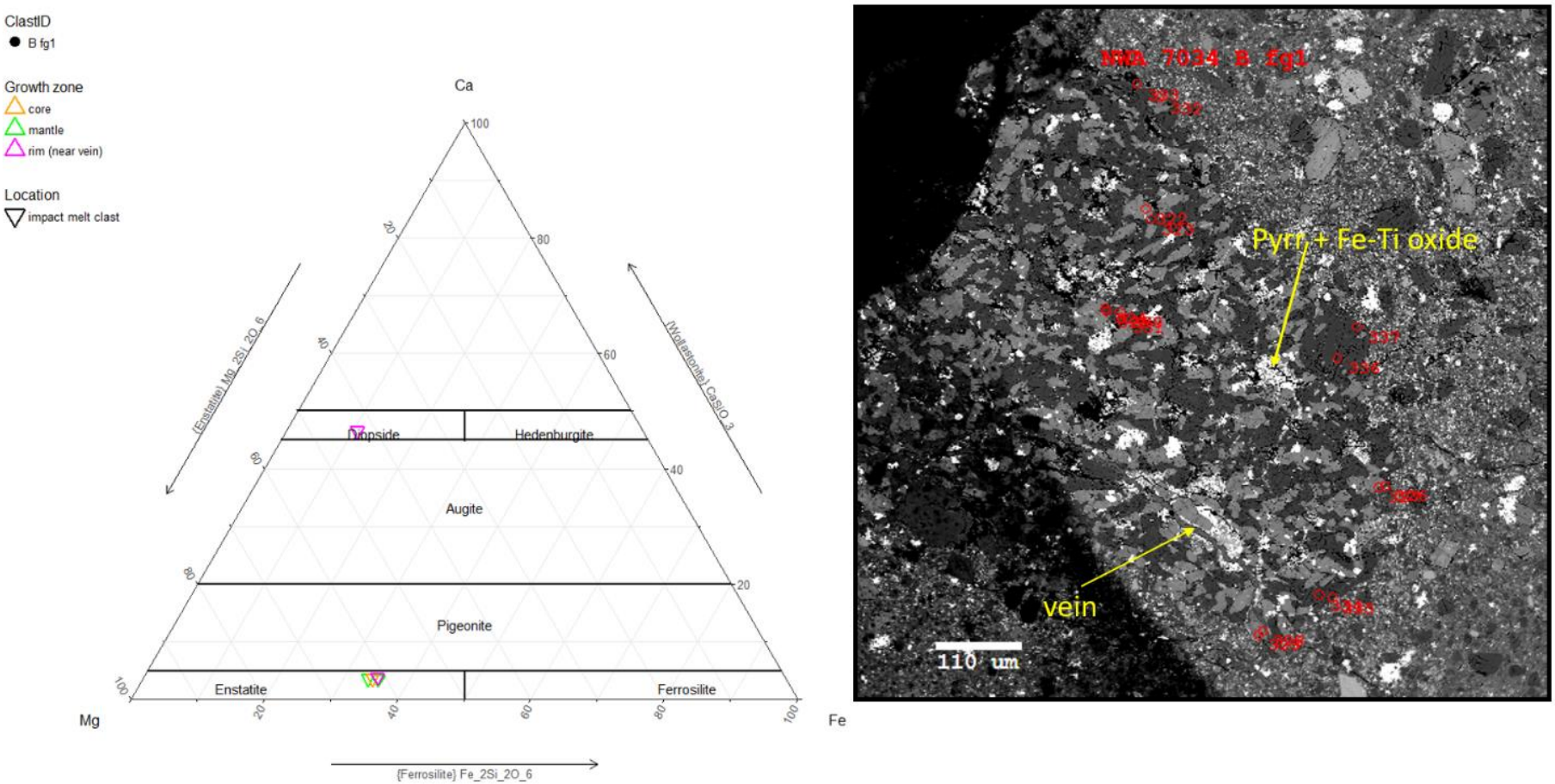

Figure 41: Pyroxene composition in gabbronorite a clast, based on normalized proportions of Mg, Ca and Fe. Grid represents areas of stability for the separate pyroxene components. Shape denotes clast location (matrix or impact melt clast). (Right) BSE image with electron microprobe sampling points (red) and zoning direction (yellow arrow). Note prominent vein crosscutting clast and surrounding impact melt clast.

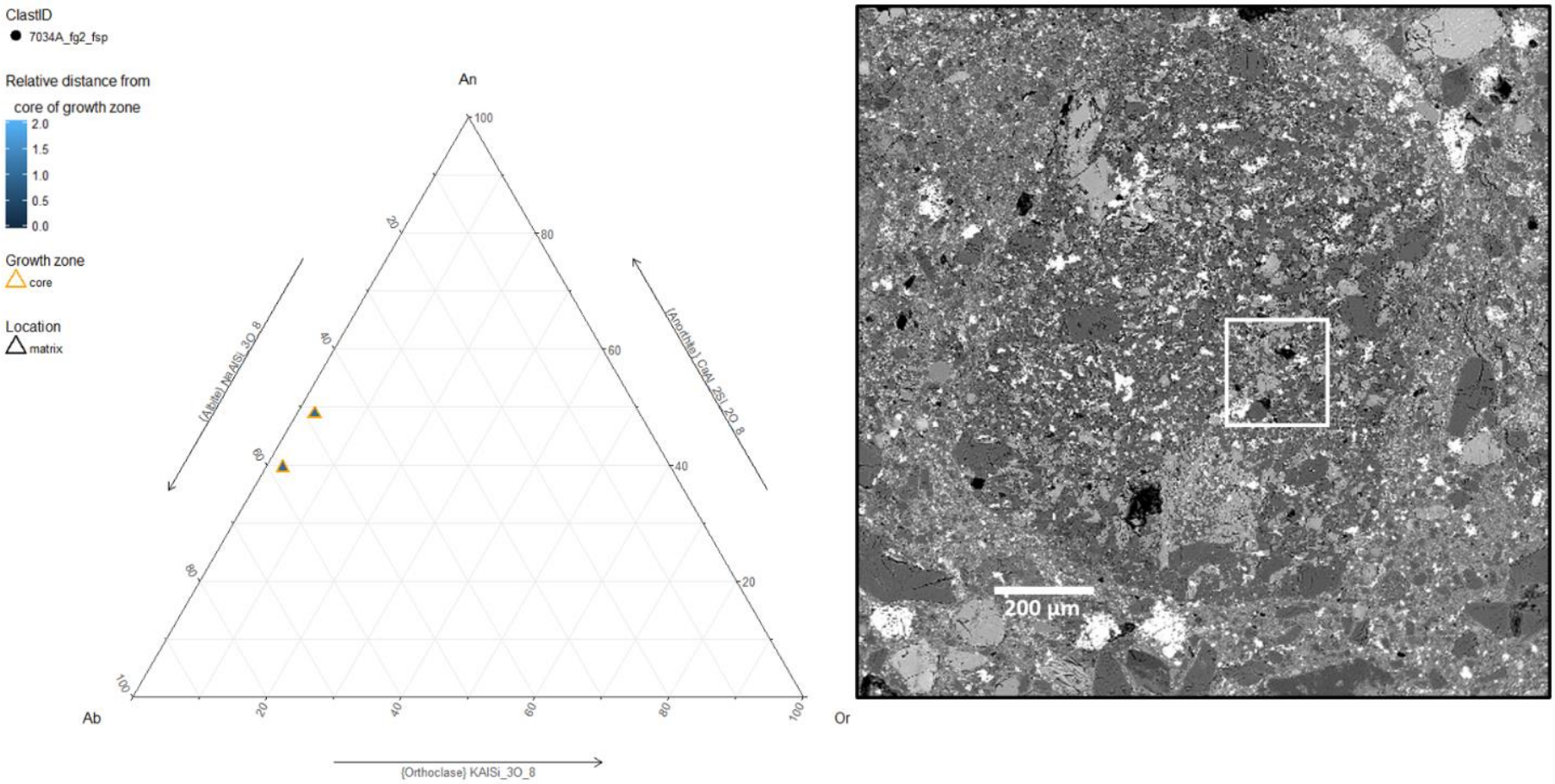

Figure 42: Feldspar composition of gabbronorite a clast, based on normalized proportions of Na, Ca and K. Grid represents areas of stability for the separate feldspar components. Blue bar denotes relative distance from core of growth zone, with 0.0 (dark blue) representing the core, and 2.0 (light blue) representing the rim. Shape denotes clast location (matrix or impact melt clast). (Right) BSE image with zoning direction (yellow arrow). Sampling area in white square.

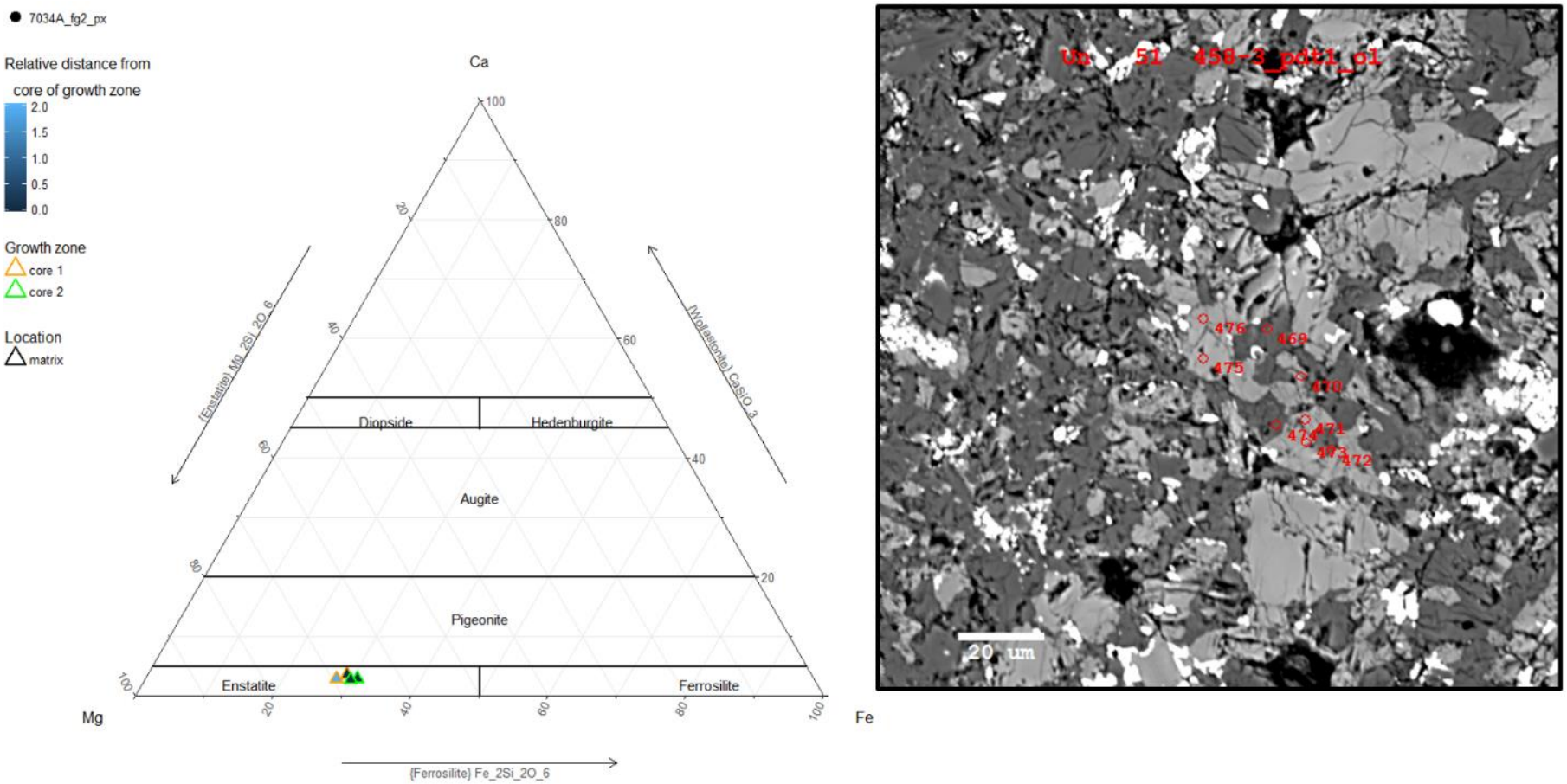

Figure 43: Pyroxene composition in gabbronorite b clast, based on normalized proportions of Mg, Ca and Fe. Grid represents areas of stability for the separate pyroxene components. Blue bar denotes relative distance from core of growth zone, with 0.0 (dark blue) representing the core, and 2.0 (light blue) representing the rim. Shape denotes clast location (matrix or impact melt clast). (Right) BSE image with electron microprobe sampling points (red) and zoning direction (yellow arrow). Note prominent vein crosscutting clast and surrounding impact melt clast.

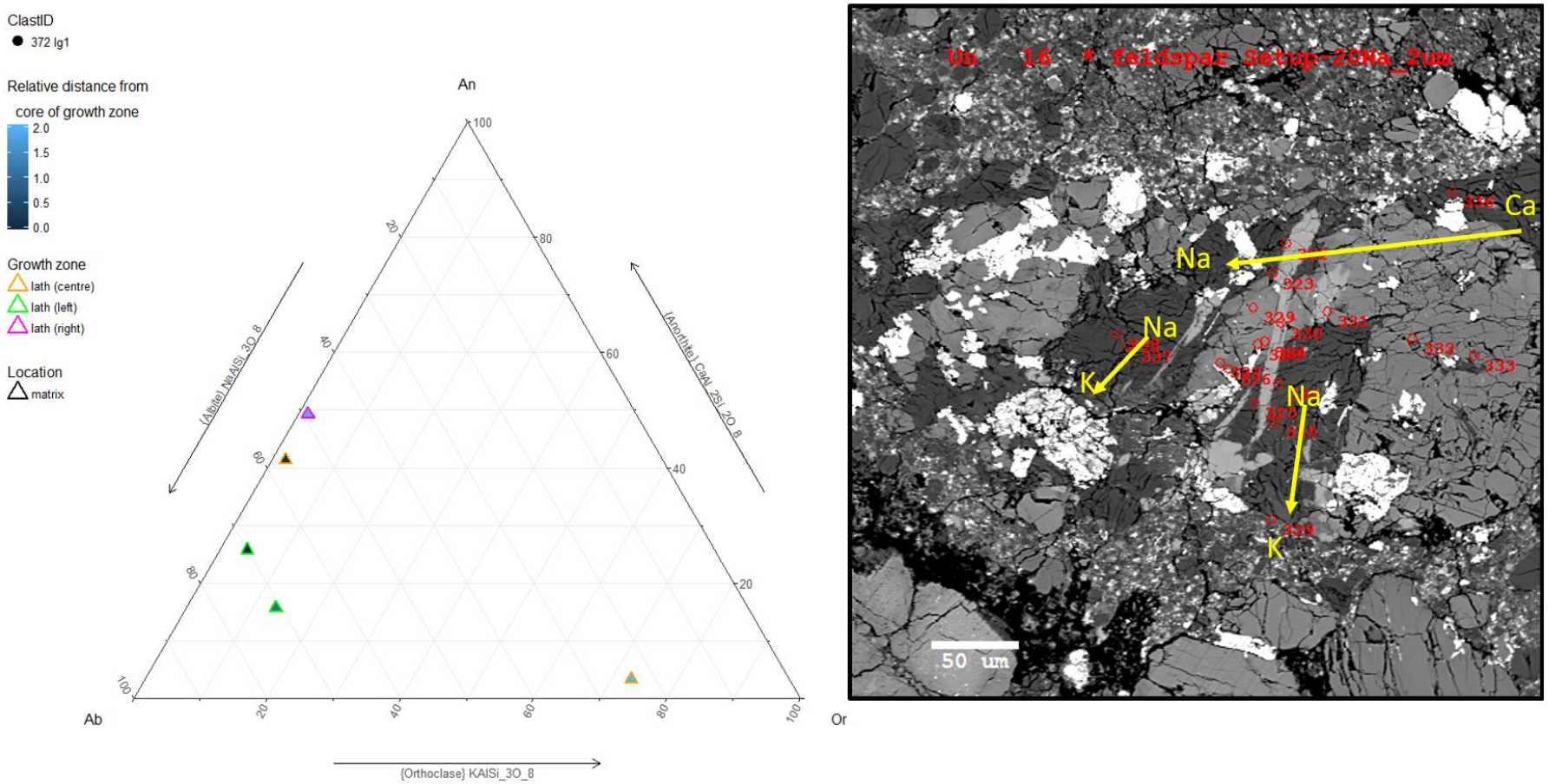

Figure 44: Feldspar composition of gabbronorite c clast, based on normalized proportions of Na, Ca and K. Grid represents areas of stability for the separate feldspar components. Blue bar denotes relative distance from core of growth zone, with 0.0 (dark blue) representing the core, and 2.0 (light blue) the rim. Shape denotes clast location (matrix or impact melt clast). (Right) BSE image with electron microprobe sampling points (red) and zoning direction (yellow arrows).

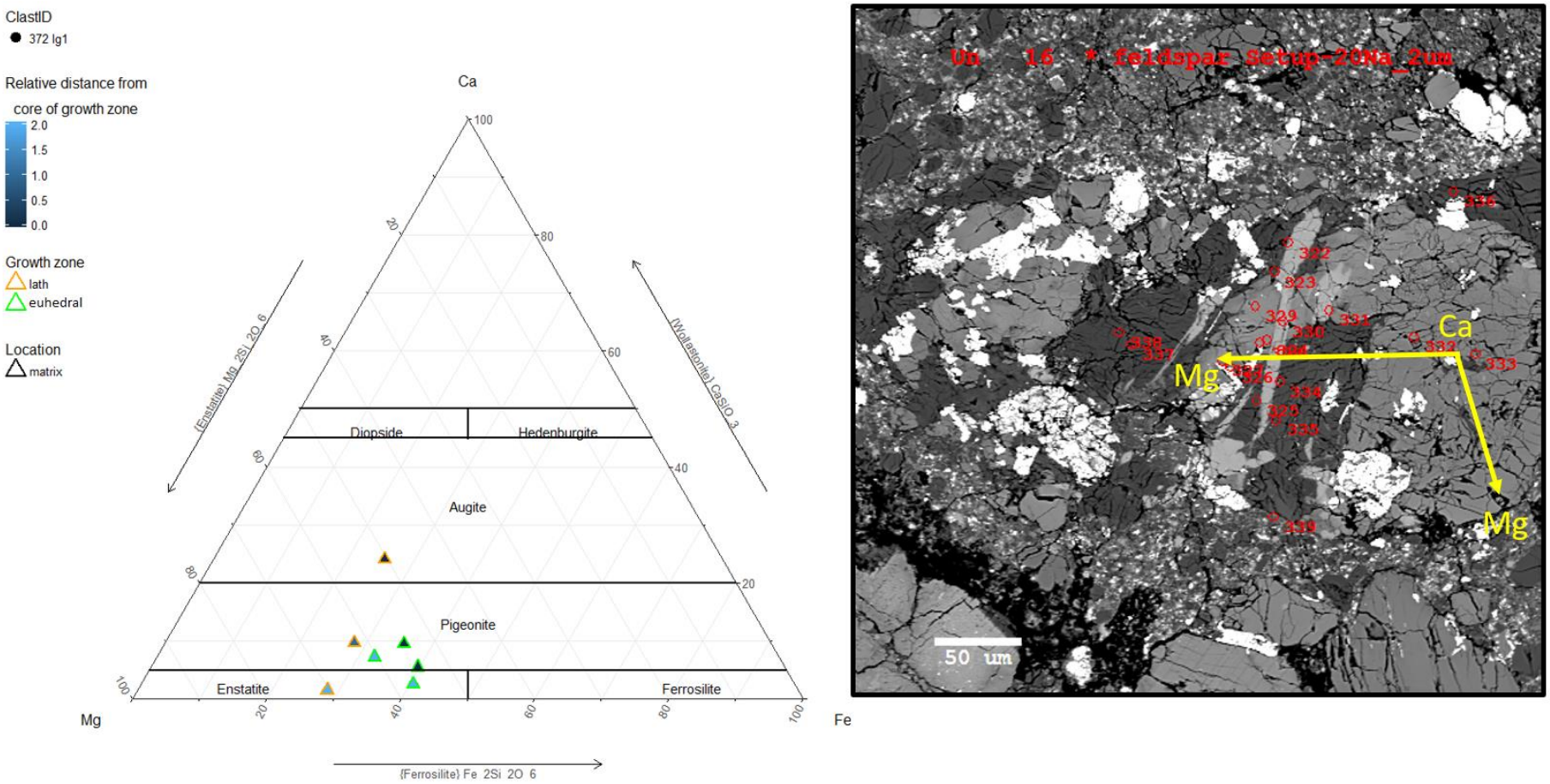

Figure 45: Pyroxene composition in gabbronorite c clast, based on normalized proportions of Mg, Ca and Fe. Grid represents areas of stability for the separate pyroxene components. Blue bar denotes relative distance from core of growth zone, with 0.0 (dark blue) representing the core, and 2.0 (light blue) representing the rim. Shape denotes clast location (matrix or impact melt clast). (Right) BSE image with electron microprobe sampling points (red) and zoning direction (yellow arrow). Note prominent vein crosscutting clast and surrounding impact melt clast.

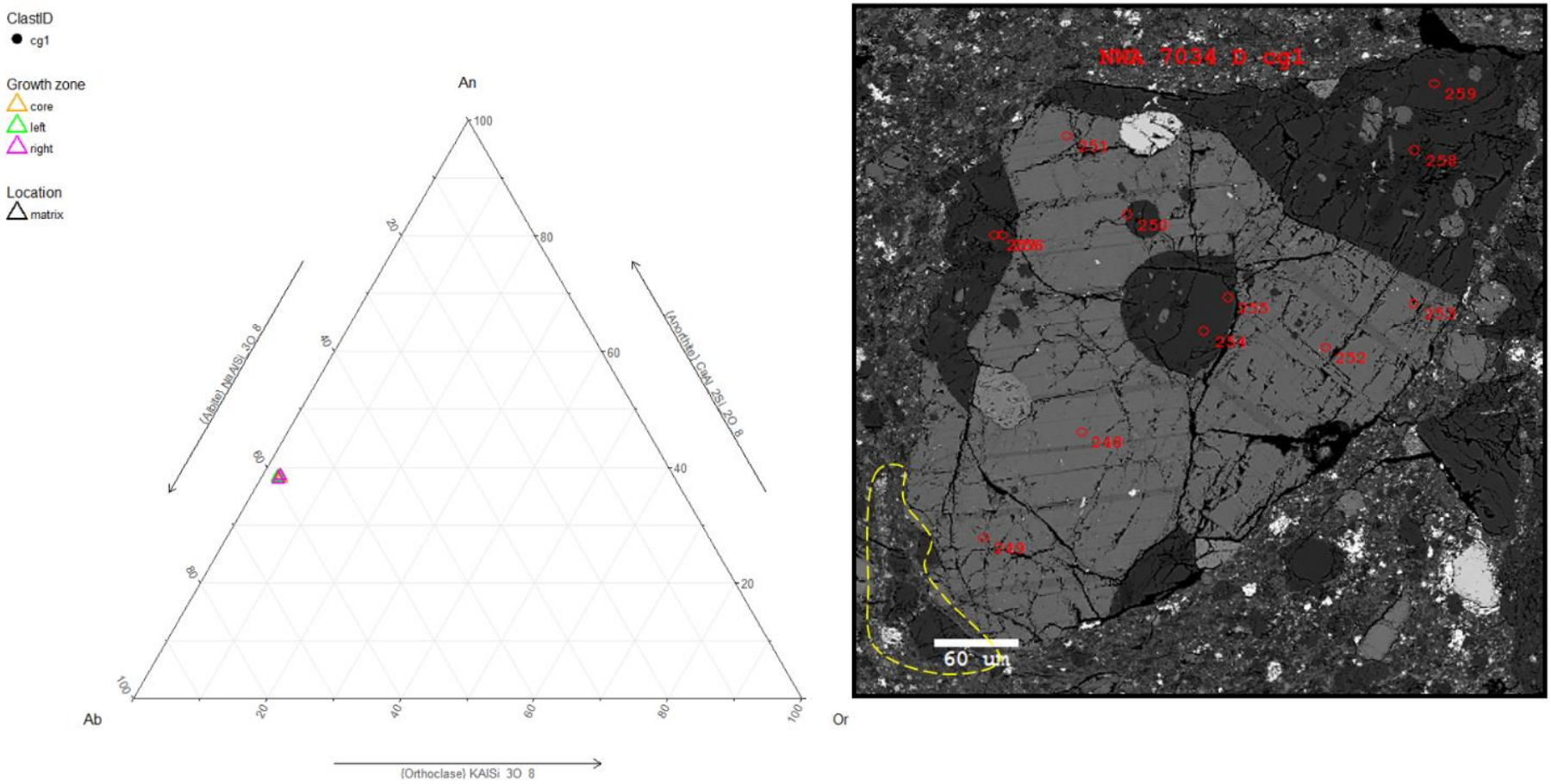

Figure 46: Feldspar composition of gabbronorite d clast, based on normalized proportions of Na, Ca and K. Grid represents areas of stability for the separate feldspar components. Shape denotes clast location (matrix or impact melt clast). (Right) BSE image with electron microprobe sampling points (red) and zoning direction (yellow arrows). Note phenocrysts separated from clast by melt (dotted line)

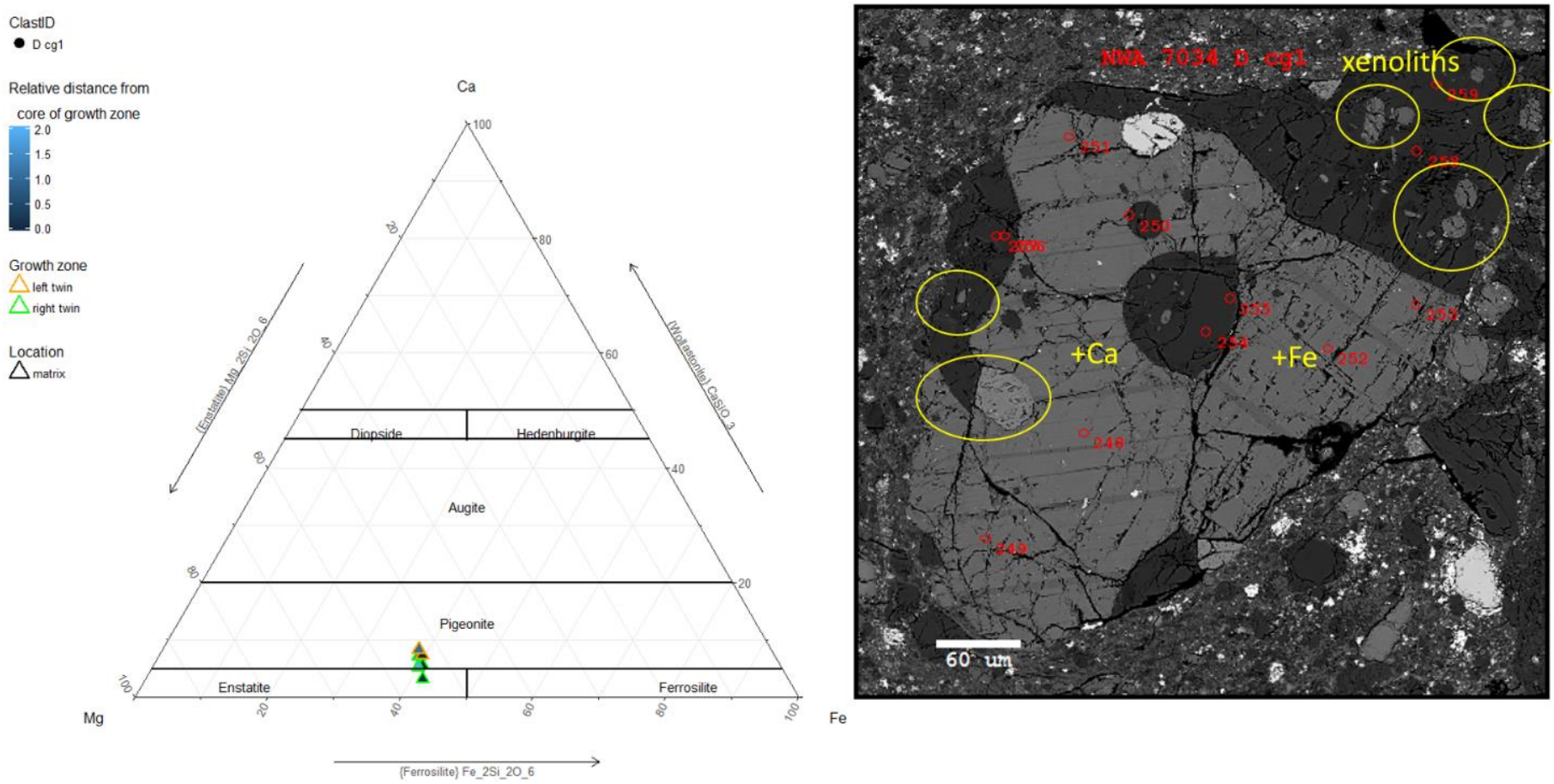

Figure 47: Pyroxene composition in gabbronorite d clast, based on normalized proportions of Mg, Ca and Fe. Grid represents areas of stability for the separate pyroxene components. Blue bar denotes relative distance from core of growth zone, with 0.0 (dark blue) representing the core, and 2.0 (light blue) representing the rim. Shape denotes clast location (matrix or impact melt clast). (Right) BSE image with electron microprobe sampling points (red) and zoning direction (yellow arrow). Note prominent vein crosscutting clast and surrounding impact melt clast.

3.3.3 Apatite-plagioclase(-ilmenite)

Apatite-plagioclase clasts were common throughout the mounts sampled. Often, they contained intergrowths of ilmenites and/or pyrrhotites. They were generally rounded, some had grains growing in equigranular shapes (Figure 48) others in lath shapes (Figure 49). Plagioclase (andesine) exhibited core to rim zoning (Ca to Na). Qemscan identified alkali feldspar growing near apatites. It was common for these clasts to be heavily fractured or have bent lath grains. Feldspar lath grains superimposed apatite growths. According to Qemscan, the clast rim commonly contained pyroxene or Mg-phyllosilicates. These were notably smaller grained (<1 μm) than the remaining grains in the clast (often a few 100s μm long). Aside from these zones, clasts had well defined concave and convex boundaries. Some apatites had perfect crystal faces.

Feldspars were similar in size, composition (andesines and alkali feldspars), zoning pattern (Na to Ca from core to rim of clast) and grain shape (lath) to those found in ilmenite-plagioclase clasts that lacked apatite (Figure 50). For these, a groundmass sample was taken via electron microprobe, which showed the groundmass as having the same composition (andesine) as the feldspars in the clast itself. Qemscan identified alkali feldspar near the ilmenite growth. Ilmenite had Fe-oxides and Fe-Ti oxides along the rim near the melt and was superimposed by plagioclase lath grains.

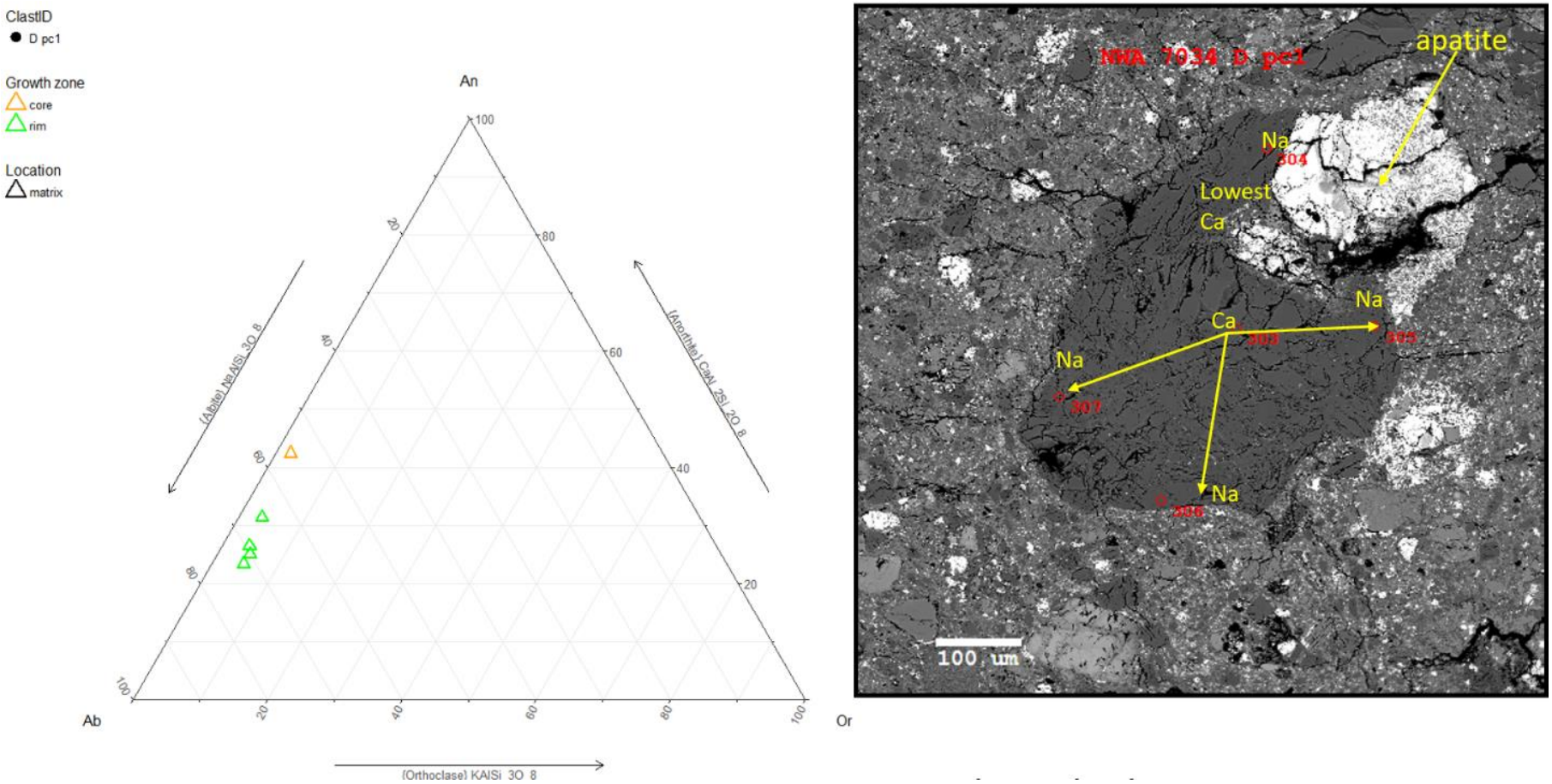

Figure 48: Feldspar composition of apatite-plagioclase clast, based on normalized proportions of Na, Ca and K. Grid represents areas of stability for the separate feldspar components. Shape denotes clast location (matrix or impact melt clast). (Right) BSE image with electron microprobe sampling points (red) and zoning direction (yellow arrows). Note phenocrysts separated from clast by melt (dotted line).

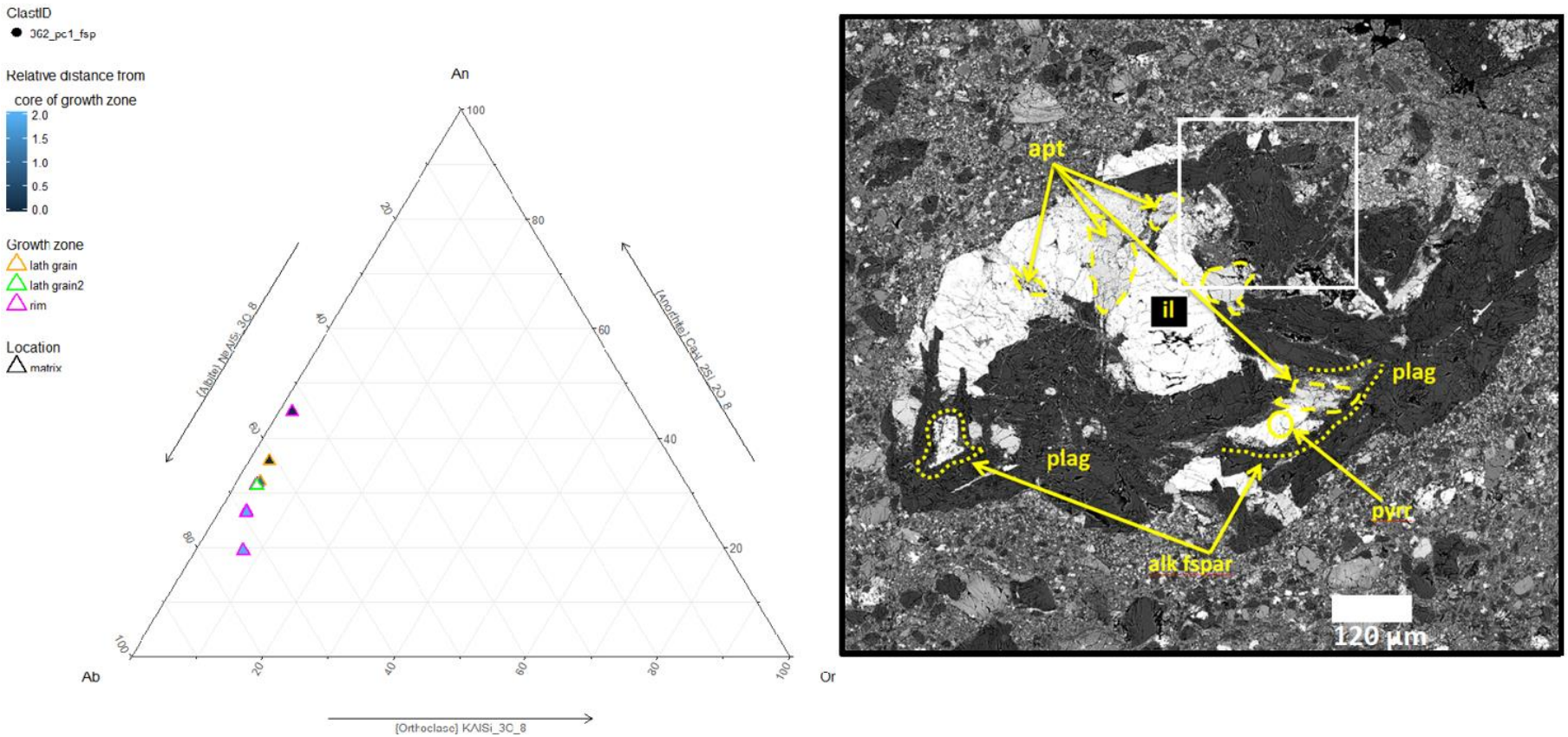

Figure 49: Feldspar composition of apatite-ilmenite-plagioclase clast (sample area in white square), based on normalized proportions of Na, Ca and K. Grid represents areas of stability for the separate feldspar components. Blue bar denotes relative distance from core of growth zone, with 0.0 (dark blue) representing the core, and 2.0 (light blue) representing the rim. Shape denotes clast location (matrix or impact melt clast). (Right) BSE image with electron microprobe sampling points (red) and zoning direction (yellow arrows). Note phenocrysts separated from clast by melt (dotted line).

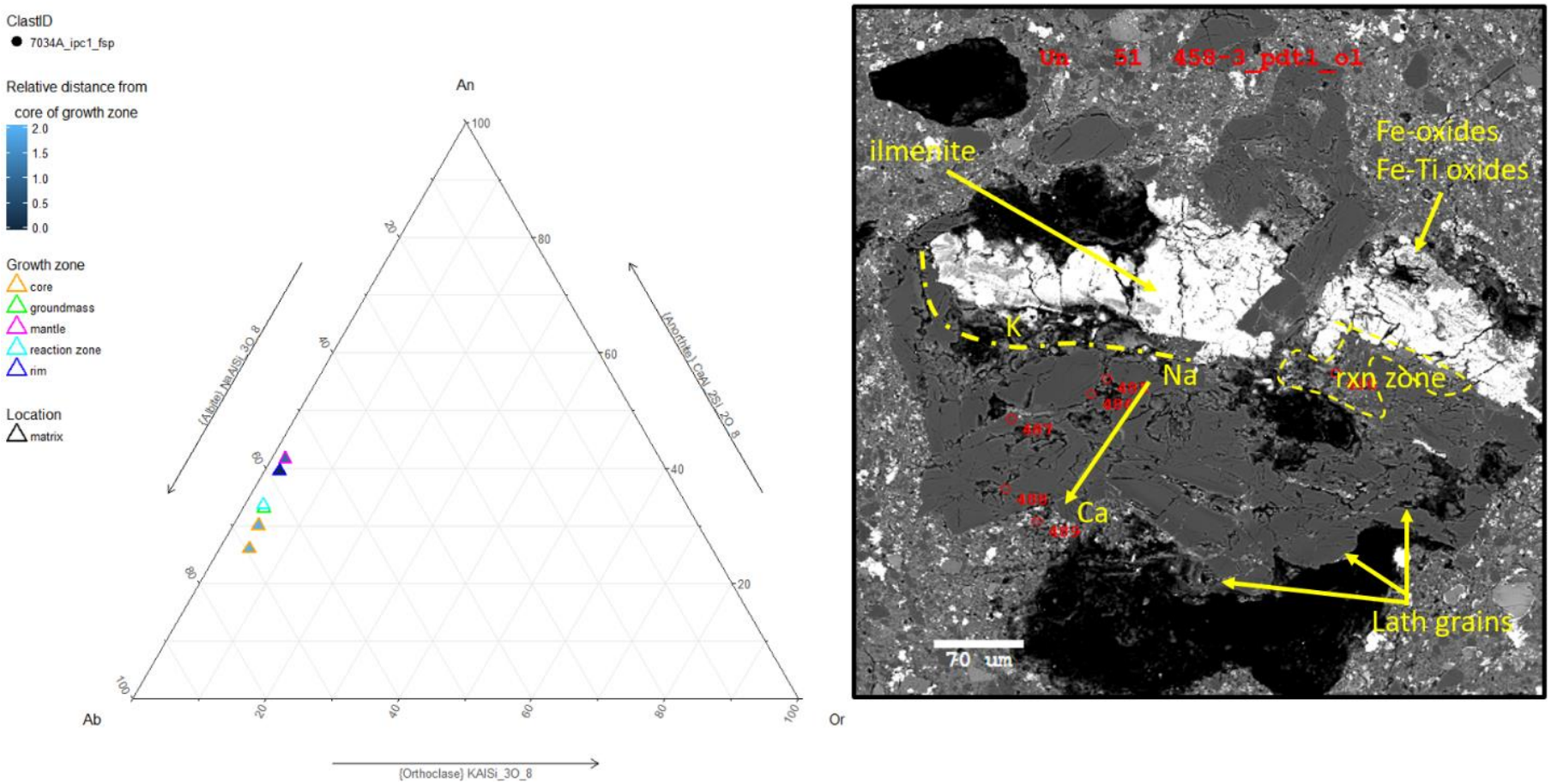

Figure 50: Feldspar composition of apatite-ilmenite-plagioclase clast, based on normalized proportions of Na, Ca and K. Grid represents areas of stability for the separate feldspar components. Blue bar denotes relative distance from core of growth zone, with 0.0 (dark blue) representing the core, and 2.0 (light blue) representing the rim. Shape denotes clast location (matrix or impact melt clast). (Right) BSE image with electron microprobe sampling points (red) and zoning direction (yellow arrows). Note phenocrysts separated from clast by melt (dotted line).

3.3.4 Gabbro

All gabbros were defined by intergrowths of primarily high Ca pyroxene and feldspar, with minor Fe-oxides. Some clasts had accessory Fe-oxide, apatite, ilmenite. Pyroxenes fell in the diopside and augite range (Figure 55). Of all gabbros, type *gabbro a* had the lowest Ca component for both feldspar and pyroxene. They had anhedral alkali feldspar contained in augite, with some euhedral grains contained in the feldspar. The alkali feldspar was zoned from core to rim (Na to K) and had lamellar intergrowths of a phase higher in Ca. The euhedral lath grains of pyroxene were higher in Fe and lower in Mg than the rounded grains. Pyroxene was zoned core to rim. (Ca to Mg; Figure 51). There was a corona of finer grained feldspar and pyroxene along the clast boundary. The composition of the feldspar in the clast was different from the surrounding matrix groundmass, which was made up of plagioclase.

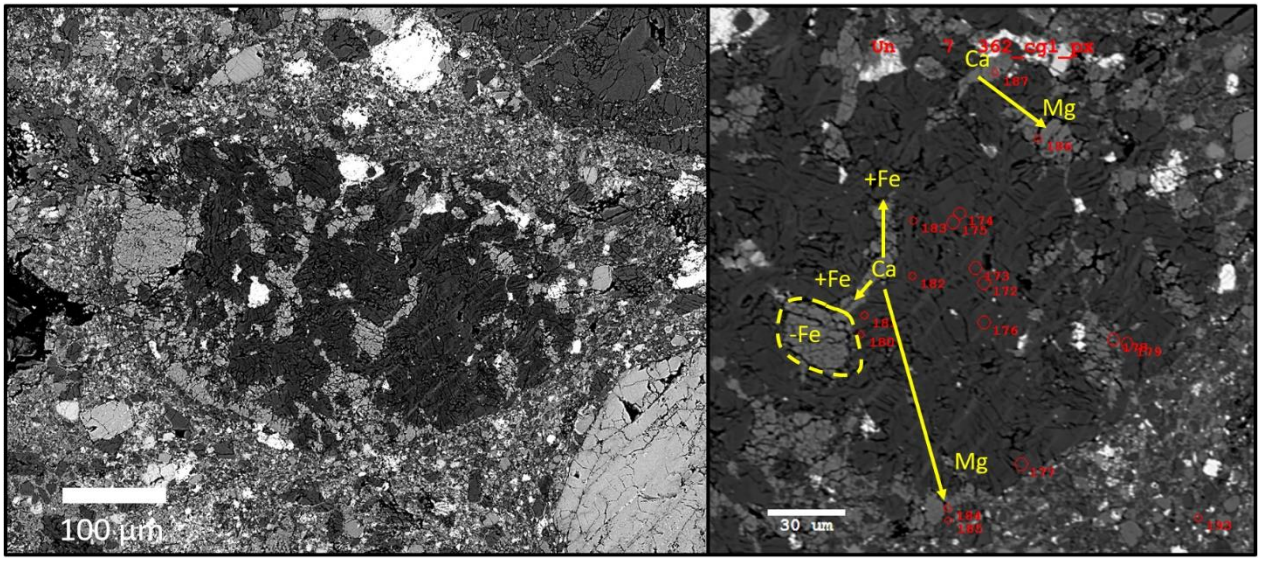

Figure 51: BSE of gabbro a (362 cg2) with electron microprobe sampling points (red). Note zoning patterns in pyroxene (yellow) and lamellae in feldspar.

Gabbro b defined a group of in which randomly arranged euhedral lath grains of plagioclase (100 µm to 200 µm long) were interspersed among anhedral augite. The plagioclase component was classified as andesine. Gabbro b had similar zoning patterns to lath grained *gabbronorite c* and the other gabbro types, with core to rim (Ca to Na) zoning in plagioclase, and core to rim (Ca, Fe to Mg) zoning in pyroxene (Figure 52). Clasts had a rounded shape. The probed sample was from the matrix, but this clast type was also present in impact melt clasts.

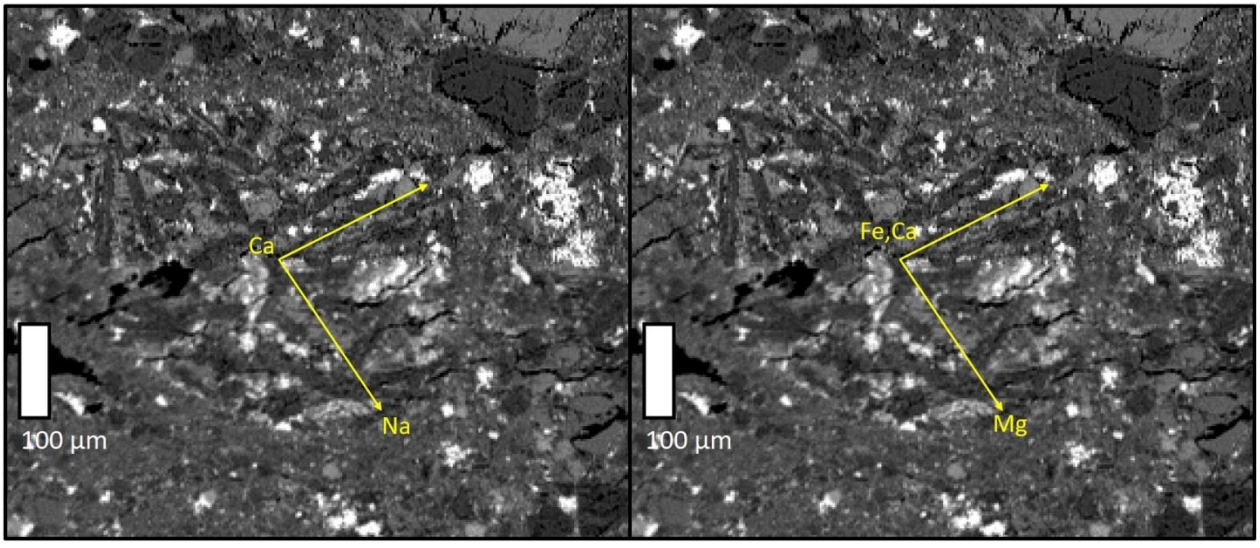

Figure 52: BSE images of gabbro b (D lg1) showing zoning patterns in plagioclase (left) and pyroxene (right).

Type *gabbro c* describes clasts of equigranular, microcrystalline texture with intergrowths of augite and albite (andesine, oligoclase). There was compositional variation in augite grains, but no directional component could be identified. The albites however were clearly zoned, with grains in the core being higher in Ca, and ones along the rim higher in Na. Both a matrix and impact melt clast were probed. Plagioclase composition overlapped, however the impact clast sample had a wider range, however the pyroxene grown in the matrix sample was higher in Fe (Figure 55). Both contained accessory iron oxides at equigranular size. Average grainsize was larger for the matrix clast. Furthermore, the clast grown in the matrix was angular in shape and the one from the impact melt rounded. The clast sampled from the impact melt was contained in a felty plagioclase-pyroxene groundmass and had poorly defined clast boundaries and melt intrusion (Figure 53).

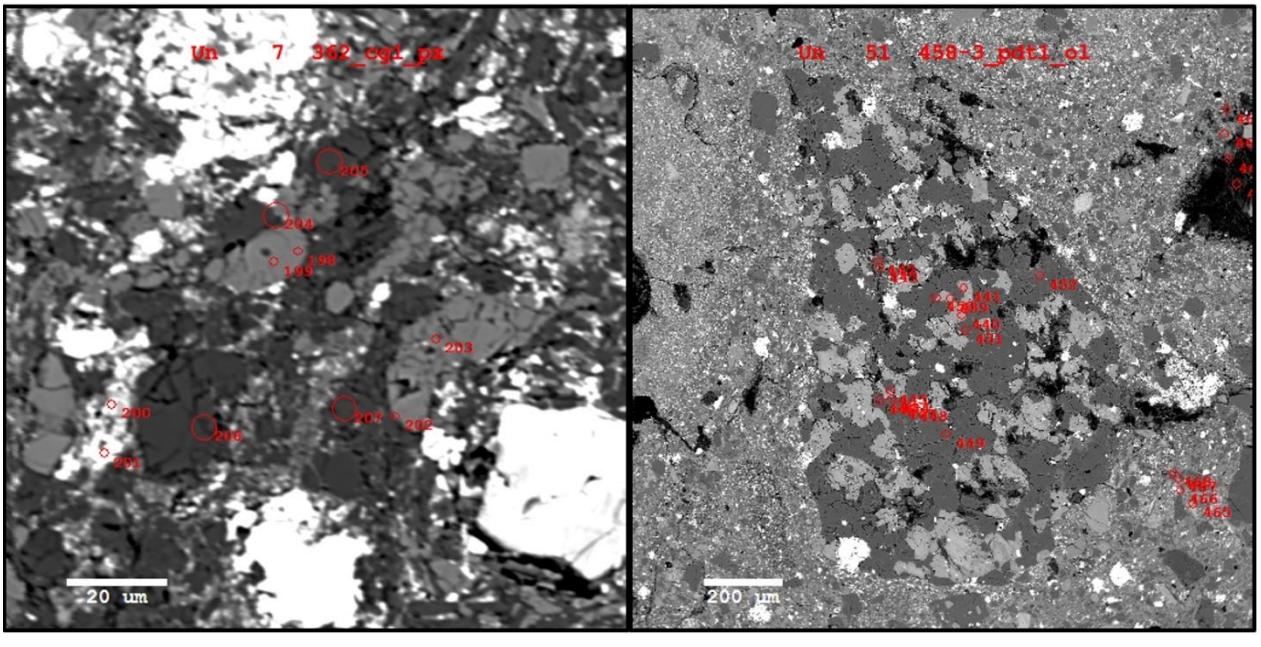

Figure 53: BSE images of gabbro c, with electron microprobe sampling points (red). Impact melt clast (left) and matrix clast (right).

Type *Gabbro d* was characterised by high plagioclase (>80%) and low pyroxene (<20%) composition. Clast of this type were found throughout the matrix. The representative sample was made up of a relatively large (~ 600 µm x 800 µm), singular, euhedral andesine grain, with growth of augite along one corner and in the core (Figure 54). The augite was strongly zoned (Ca – Mg), through no clear directional compositional pattern could be identified. The andesine grain was zoned from core to rim (Ca to Na).

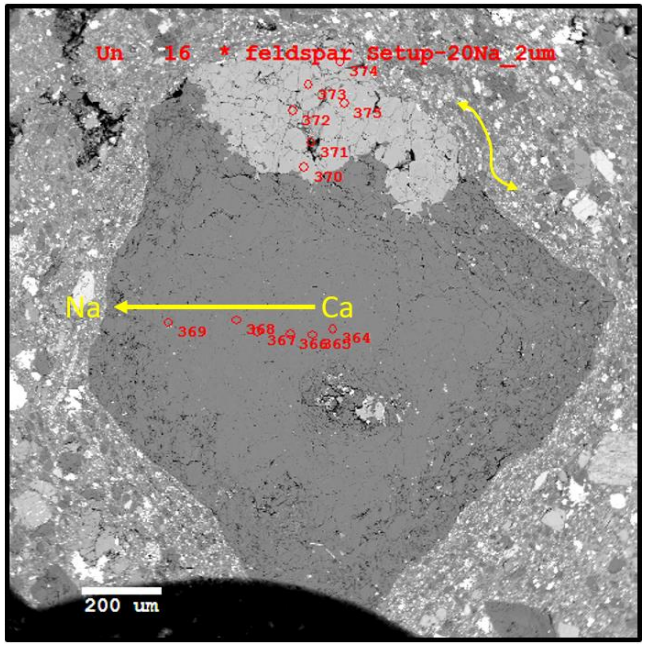

Figure 54: BSE image of gabbro d (372 vcg1) with electron microprobe sampling points (red). Note zoning pattern of plagioclase and flow texture of matrix (yellow arrow).

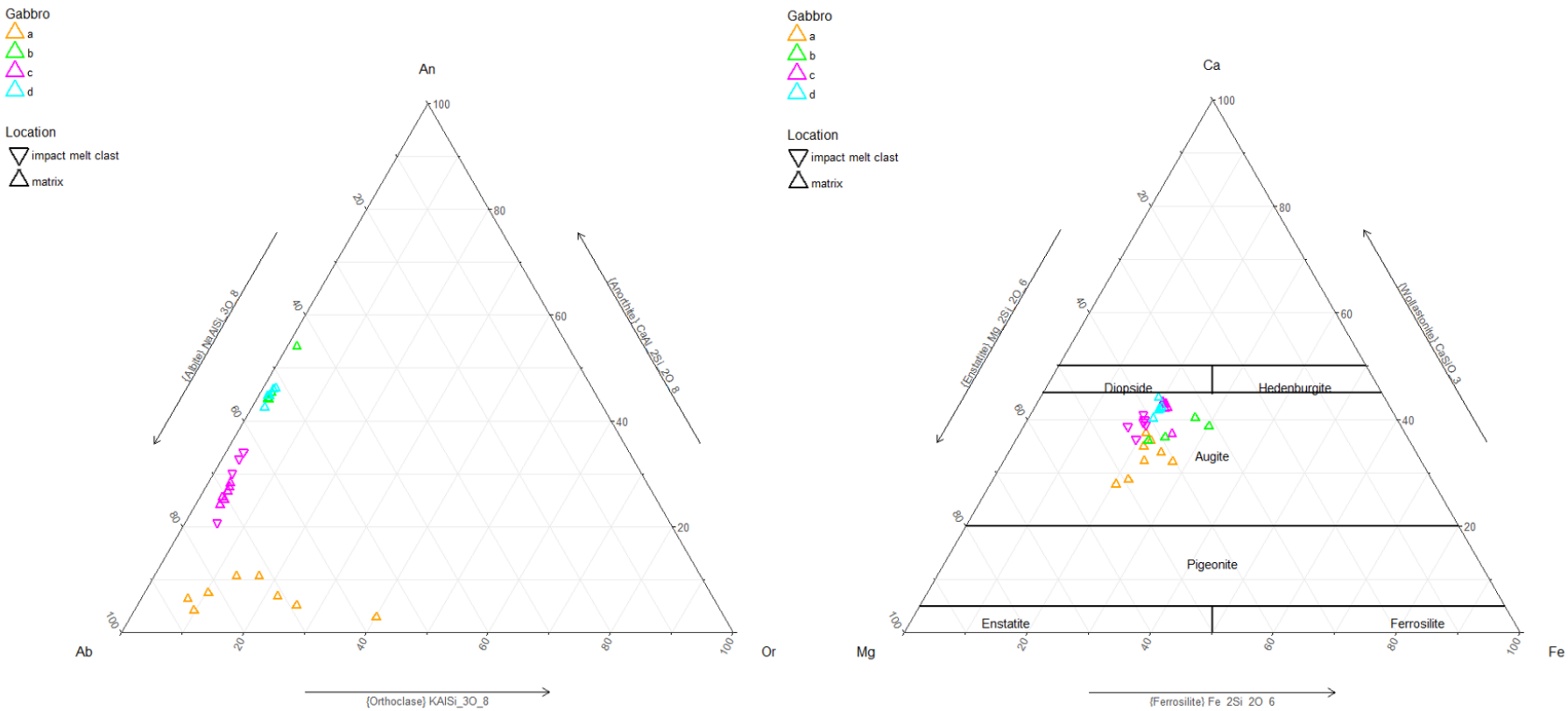

Figure 55: Composition of feldspars (left) and pyroxenes (right) in gabbros according to gabbro type, based on normalized proportions of Na, Ca, K (left), and Mg, Ca, Fe (right). Grid represents areas of stability for the separate pyroxene components. Shape denotes clast location (matrix or impact melt clast).

3.4 PERIDOTITES

Only one peridotite could be successfully microprobed, the rest yielded bad totals. Therefore, there is not enough information to make general assumptions about peridotites in NWA 7034. This one sample had pyroxenes high in Mg (77 ± 1 %) with some Fe (21 ± 1 %), and a near absence of Ca (<2% = 1.5 ± 0.1 %, Figure 56). All were in the enstatite range. Zoning was minimal and occurred in the Mg-Fe direction. The highest Fe phase was found in the reaction zone, while all other sampling points overlapped in composition. BSE images of peridotite clasts showed them to be heavily fractured, with melt intruding into some of the fractures. The majority of the crystal faces had clearly defined, angular outlines, but some sides of the clast were more rounded, with reactions occurring at the clast boundary, with high Fe phases that occurred in a speckled pattern or embayed boundary. Some clasts appeared to have been partially resorbed by the melt (see thin dotted line, Figure 56). The surrounding groundmass had a quench texture.

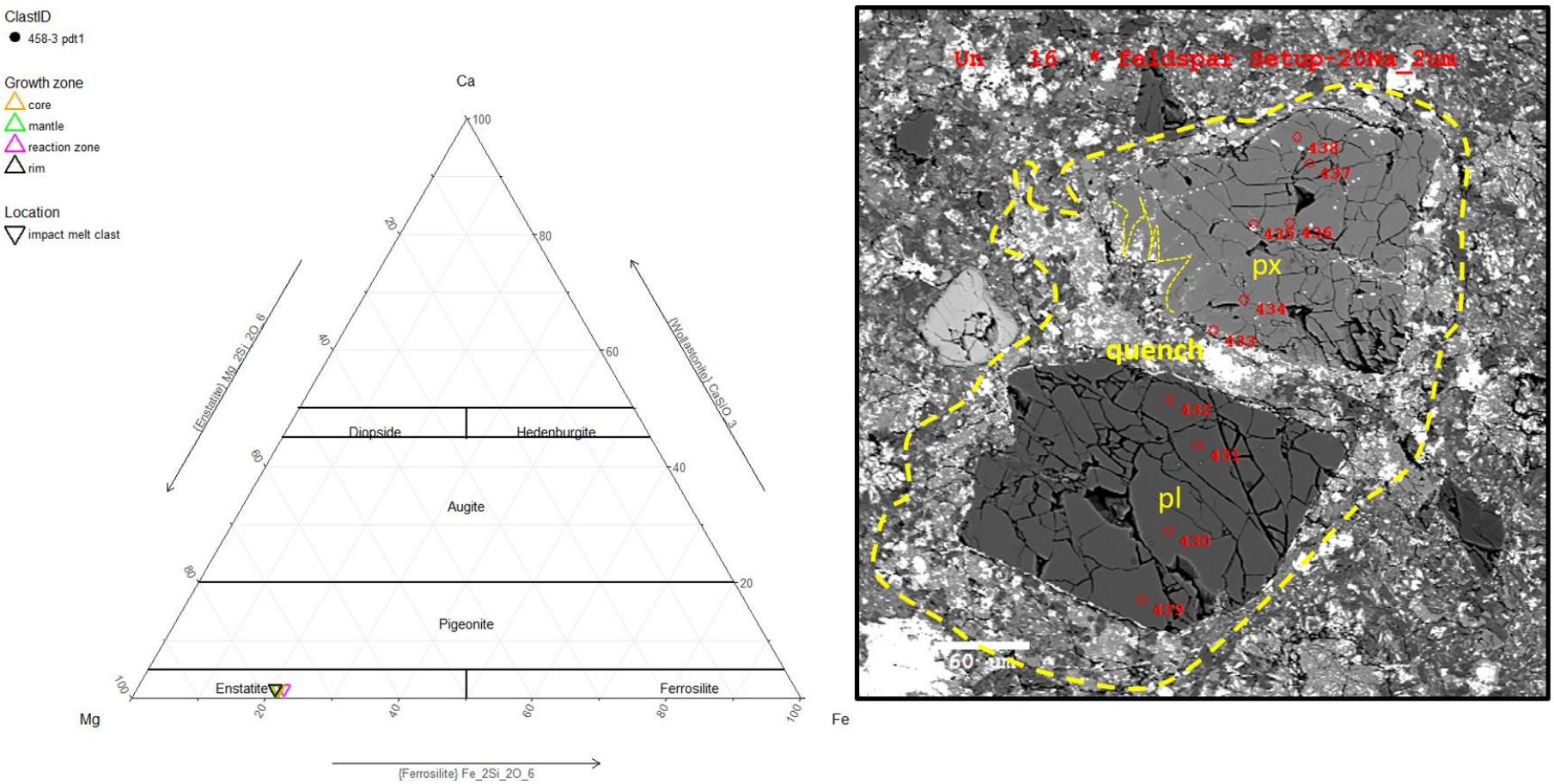

Figure 56: (Left) Pyroxene composition of peridotite phenocryst, based on normalized proportions of Mg, Ca and Fe. Grid represents areas of stability for the separate pyroxene components. Blue bar denotes relative distance from core of growth zone. Coloured outlines are used to give more detailed information about the sampling location within the clast. Shape gives clast location (matrix or impact melt clast). (Right) BSE image with electron microprobe sampling points (red). Dotted line represents reaction zone. Yellow arrow shows where clast was consumed by melt, as seen by embayed clast boundary (thin dotted line). Peridotite 458-3 pdt1 (top) and plagioclase (bottom).

3.5 SPHERULES

Spherules were divided into five types, based on texture, and composition of pyroxene. These included: enstatite, augite-plagioclase, lath grained enstatite in plagioclase-augite groundmass, diopside-plagioclase-enstatite, and enstatite-plagioclase spherules. Each type exhibited distinct zoning patterns (Table 9).

Table 9: Spherule types with their defining characteristic composition and -textures, and zoning patterns (from core to rim of spherule) and associated samples.

Type	*Defining characteristics*	*Zoning in pyroxene*	*Zoning in plagioclase*	*Representative sample(s)*
Enstatite	Enstatite with iron oxide phase inclusions	core to rim (lower Ca)	n/a	A sph1
Augite-plagioclase	Augite quench with radial plagioclase lath grains	Fe-Ca	core to rim (Ca to Na)	372 px (c)1
Lath grained enstatite in plagioclase-augite groundmass	Enstatite lath grains in felty plagioclase-augite groundmass	core to rim (Mg to Fe)	core to rim (Ca to Na)	362 lgn1
Diopside-plagioclase-enstatite	Diopside core contained in plagioclase with enstatite rim	core to rim (Fe to Mg), Ca enriched growth at rim	core to rim (Ca to Na, K)	458-3 cg2, 458-3 cg1
Enstatite-plagioclase	Plagioclase core with radial enstatite and plagioclase lath along rim	Mg – Fe	core to rim (Ca to Na)	D fg1

The *enstatite* spherule sampled (A sph 1) was compositionally similar to the other pyroxene phenocrysts in impact melt clasts. It had a similar Ca content (4 ± 1 %), but a higher Mg content (70 ± 1 %) and lower Fe content (25 ± 1 %). There was minor core to rim zoning, with the component becoming less calcic towards the rim (Figure 57). The spherule had a radius of ~150 µm and was composed predominantly of pyroxene (enstatite). It was distinguished from enstatite phenocrysts by its skeletal, radially grown iron oxide inclusions (~5 to ~15 µm). It had wide fractures (~5 µm), particularly along the clast boundary.

Augite-plagioclase spherule had a radius of ~350 µm. Exact clast boundary could not be defined. Plagioclase had skeletal and lath texture, lath grains were up to ~200 µm long, but pyroxene and iron oxide grains were <5 µm. Pyroxene (augite) was contained within a halo of lath grained plagioclase (albite – andesine) that grew perpendicular to clast boundary. Plagioclase lath grains were also found at the centre of the clast, zoned Ca to Na from core to rim (Figure 58). There were interstitial Fe-oxides, cross cutting pyroxene and plagioclase. Fractures were found along grain boundaries also, crosscutting Fe-oxides. As seen in the BSE image (Figure 59), pyroxene was heavily zoned from core to rim. Unfortunately, only two of the sampling probes yielded usable data (both taken from rim). These showed Ca-Fe variation. The phase in the core may not be defined as augite. The pyroxene along the rim of the clast was higher in Ca, while the phase at the centre is higher in Fe.

One spherule was characterised by its *lath grained enstatite in felty plagioclase-augite* groundmass (Figure 60). It was the only clast of its kind found throughout all mounts. It was located within a larger impact melt clast with larger grained groundmass and Fe-enriched composition (compared to matrix and other impact melt clasts). It had lath grains of enstatite, contained in an equigranular, aphanitic groundmass of plagioclase (anorthite) and pyroxene (augite). The groundmass had trachytic texture (feldspar microlites oriented in the same direction). Larger, rounded Fe-oxide phases displaced the groundmass. Groundmass exhibited compositional zoning, with Na content increasing from core to rim for plagioclase (Figure 62). Pyroxene lath grains were ~300 µm long and roughly parallel to each other. They contained Fe-oxide inclusions, parallel to growth direction, and fractures, both parallel and perpendicular to growth direction. Core to rim zoning of Mg to Fe was recorded in two separate lath grains. The lath grains in the centre of the clast had a higher Mg/Fe ratio than the ones at the edge. This was the opposite pattern exhibited by pyroxene phenocrysts sampled from impact melt clasts, where Mg concentration increased from core to rim.

Diopside-plagioclase-enstatite spherules were made up of a diopside core contained in a plagioclase mantle and enstatite rim. They were only found in impact melt clasts. These spherules were common in mount 458-3, where four clasts of this type were identified, three as part of one impact melt clast. Qemscan determined that all clasts of this type had a characteristic augite-plagioclase-enstatite composition. Clasts had pyroxene (diopside) cores, where the phase grew as lath grains, in some cases radially (Figure 64), or with cleavages intersecting at an ~120-125˚ angle (Figure 63). Diopsides were encased by highly fractured plagioclase (albite) and exhibited core to rim zoning of Fe to Mg. The plagioclase was an albite, with inhomogeneous composition. There was zoning in proximity of the diopside lath grains, where composition transitioned from sodic oligoclase to more calcic andesine (Figure 65). Along the clast boundary there was a rim of pyroxene (enstatite) (Figure 63). The clast boundaries in contact with melt were not well defined (embayed). The enstatite had an embayed grain boundary at the contact with the melt, whereas it had clearly defined grain boundaries at the contact with plagioclase. Clasts of this type commonly had Fe-Ti or Fe-oxide inclusions sized >80 µm, but not all. These inclusions were less fractured than the plagioclase.

Enstatite-plagioclase spherules were characterised by a plagioclase core with a rim of plagioclase (andesine) and enstatite lath grains, oriented primarily in a radially outward direction (Figure 66). The sampled clast had a diameter of ~160 µm. Its shape was not perfectly rounded. There was a change in growth texture, going from equigranular to lath. The spherule was surrounded by a fine grained reaction zone at the boarder to the melt. There was core to rim (Ca to Na) zoning in the plagioclase. The enstatite had a composition of 27 to 31% Fe (66 to 68% Mg), and no directional zoning. Like the other spherules, these were found in impact melt clasts.

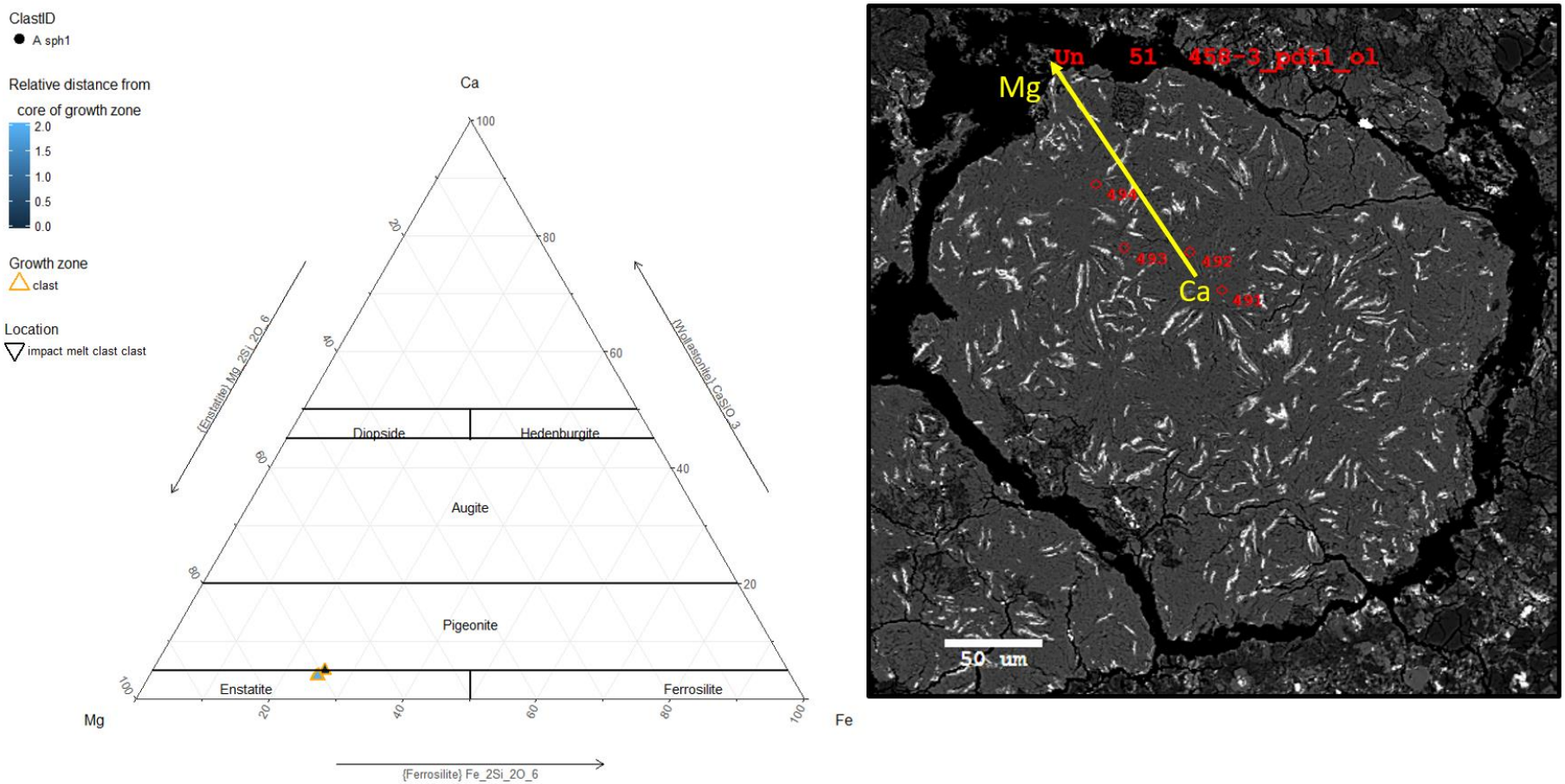

Figure 57: (Left) Pyroxene composition of enstatite spherule, based on normalized proportions of Mg, Ca and Fe. Grid represents areas of stability for the separate pyroxene components. Coloured outlines are used to give more detailed information about the sampling location within the clast. Shape gives clast location (matrix or impact melt clast). Blue bar denotes relative distance from core of growth zone, with 0.0 (dark blue) representing the core, and 2.0 (light blue) representing the rim. (Right) BSE image with electron microprobe sampling points (red) and zoning direction (yellow arrow).

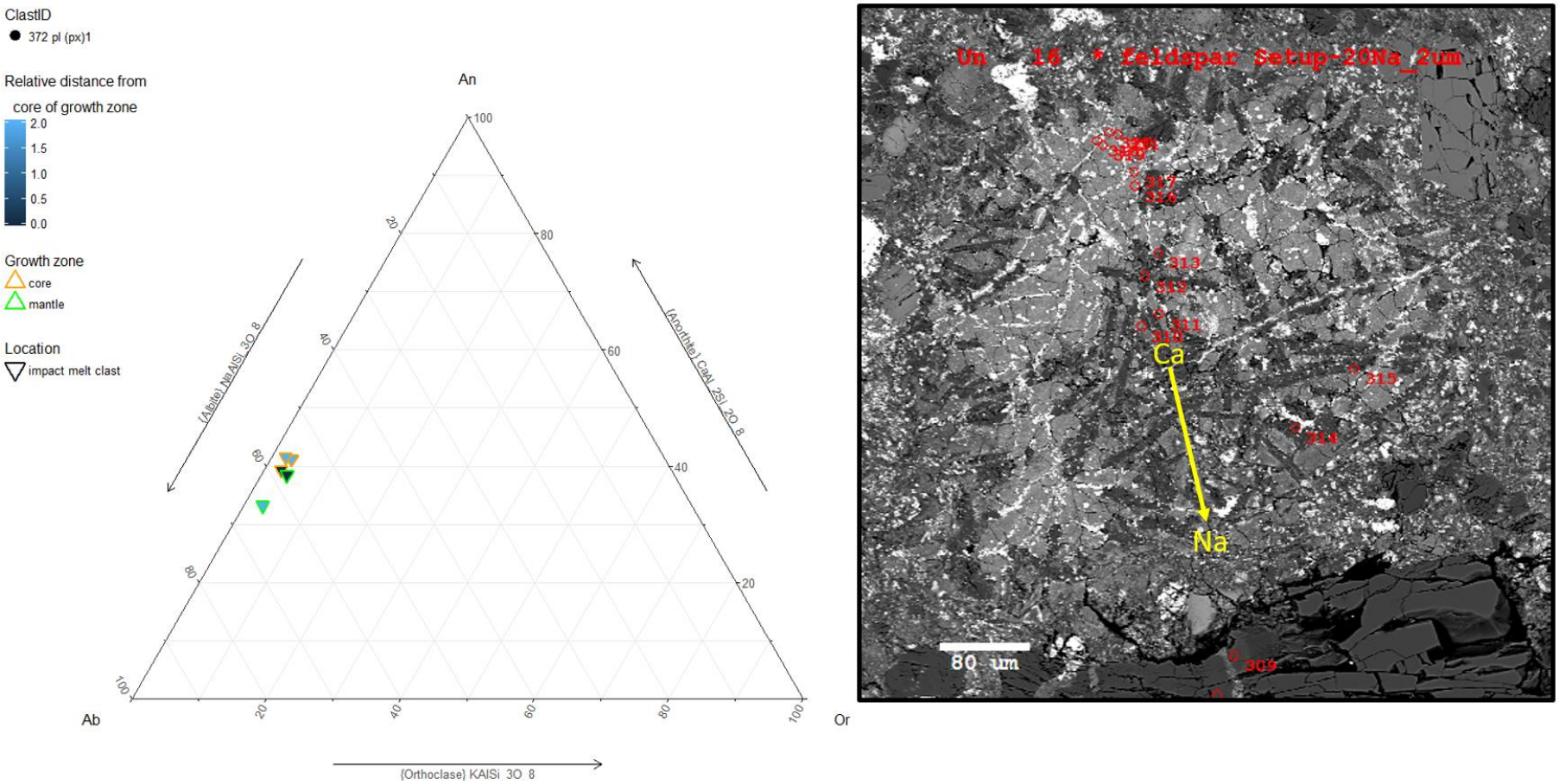

Figure 58: (Left) Feldspar composition of augite-plagioclase spherule, based on normalized proportions of K, Ca and Na. Coloured outlines are used to give more detailed information about the sampling location within the clast. Shape gives clast location (matrix or impact melt clast). Blue bar denotes relative distance from core of growth zone, with 0.0 (dark blue) representing the core, and 2.0 (light blue) representing the rim. (Right) BSE image with electron microprobe sampling points (red) and zoning direction (yellow arrow).

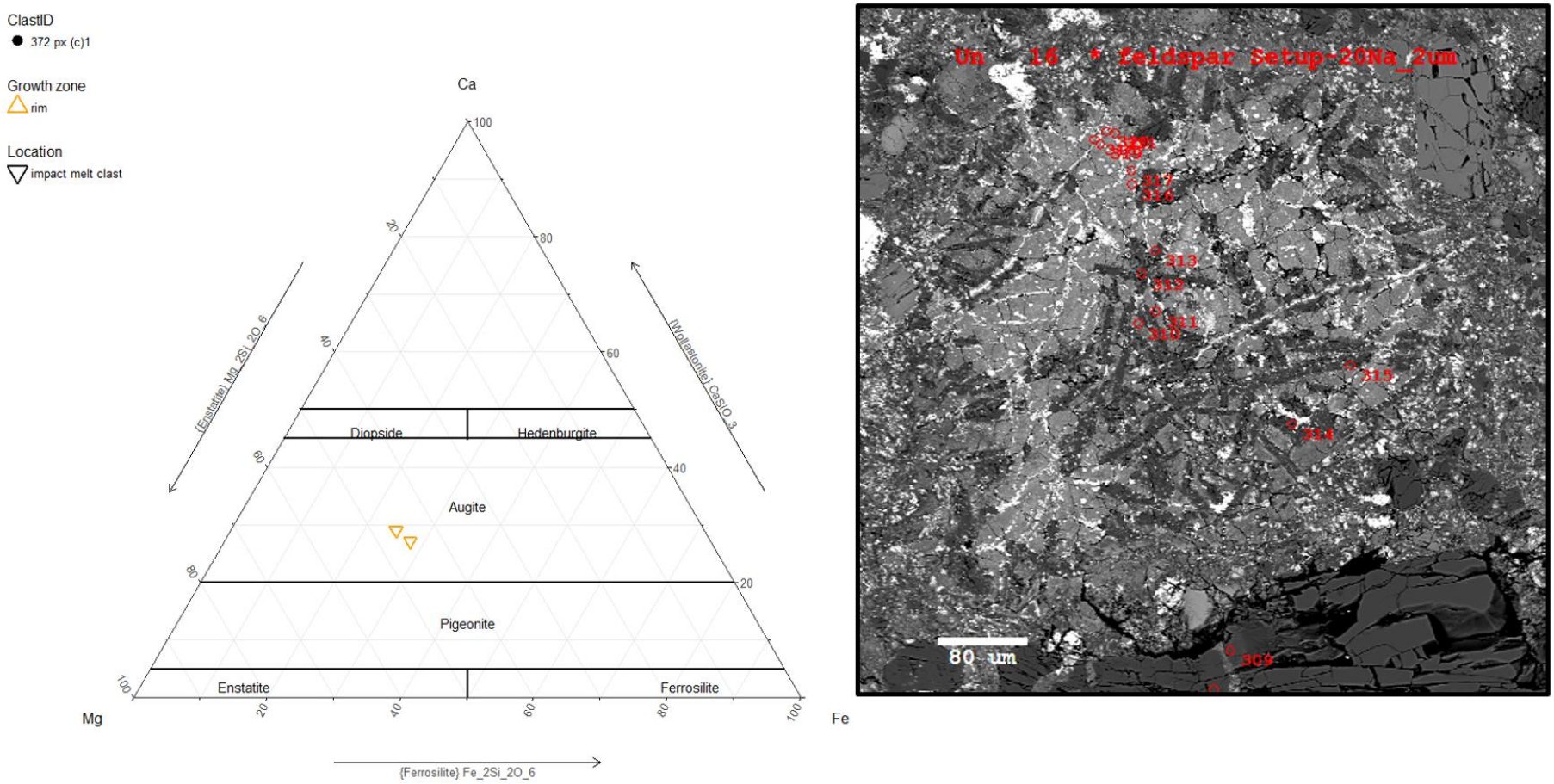

Figure 59: (Left) Pyroxene composition of augite-plagioclase spherule, based on normalized proportions of Mg, Ca and Fe. Grid represents areas of stability for the separate pyroxene components. Coloured outlines are used to give more detailed information about the sampling location within the clast. Shape gives clast location (matrix or impact melt clast). (Right) BSE image with electron microprobe sampling points (red) and zoning direction (yellow arrow).

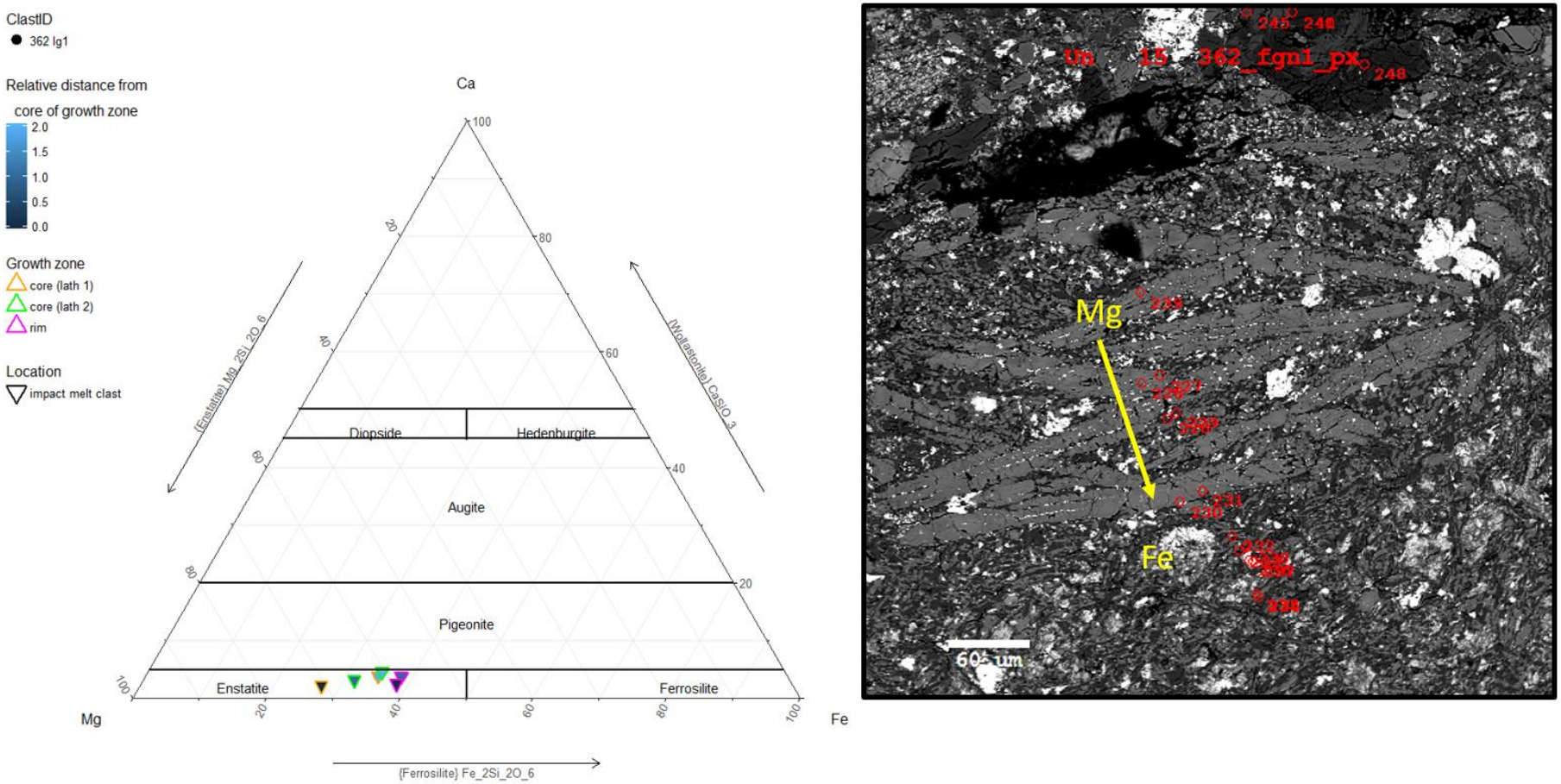

Figure 60: (Left) Pyroxene composition of lath grains in lath grained enstatite spherule, based on normalized proportions of Mg, Ca, Fe. Grid represents areas of stability for the separate pyroxene components. Coloured outlines are used to give more detailed information about the sampling location within the clast. Blue bar denotes relative distance from core of growth zone, with 0.0 (dark blue) representing the core, and 2.0 (light blue) representing the rim. Shape gives clast location (matrix or impact melt clast). (Right) BSE image with electron microprobe sampling points (red) and zoning direction (yellow arrow).

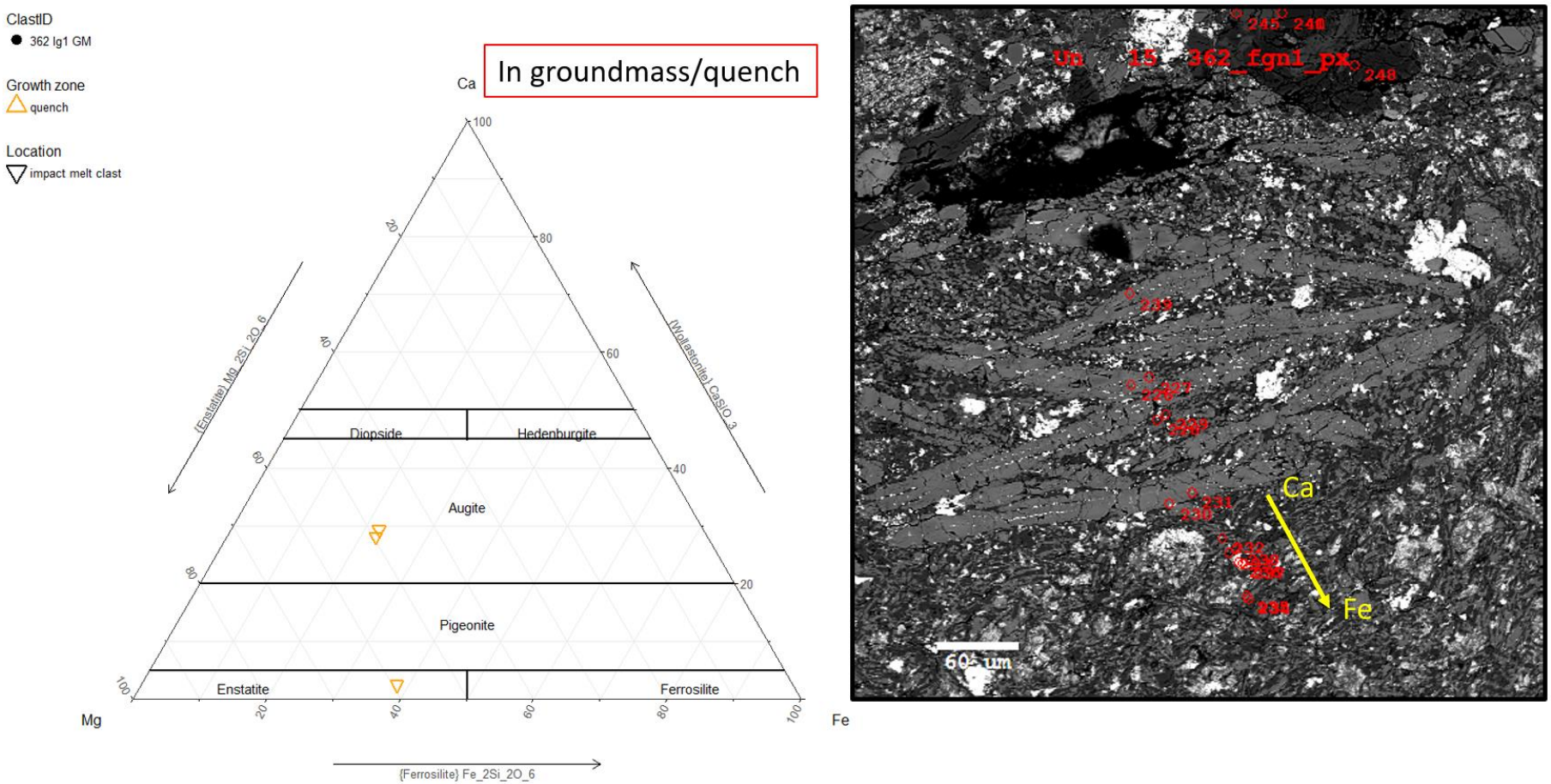

Figure 61: (Left) Composition of pyroxene in groundmass in lath grained enstatite spherule, based on normalized proportions of Mg, Ca, Fe. Grid represents areas of stability for the separate pyroxene components. Coloured outlines are used to give more detailed information about the sampling location within the clast. Shape denotes clast location (matrix or impact melt clast). (Right) BSE image with electron microprobe sampling points (red) and zoning direction (yellow arrow).

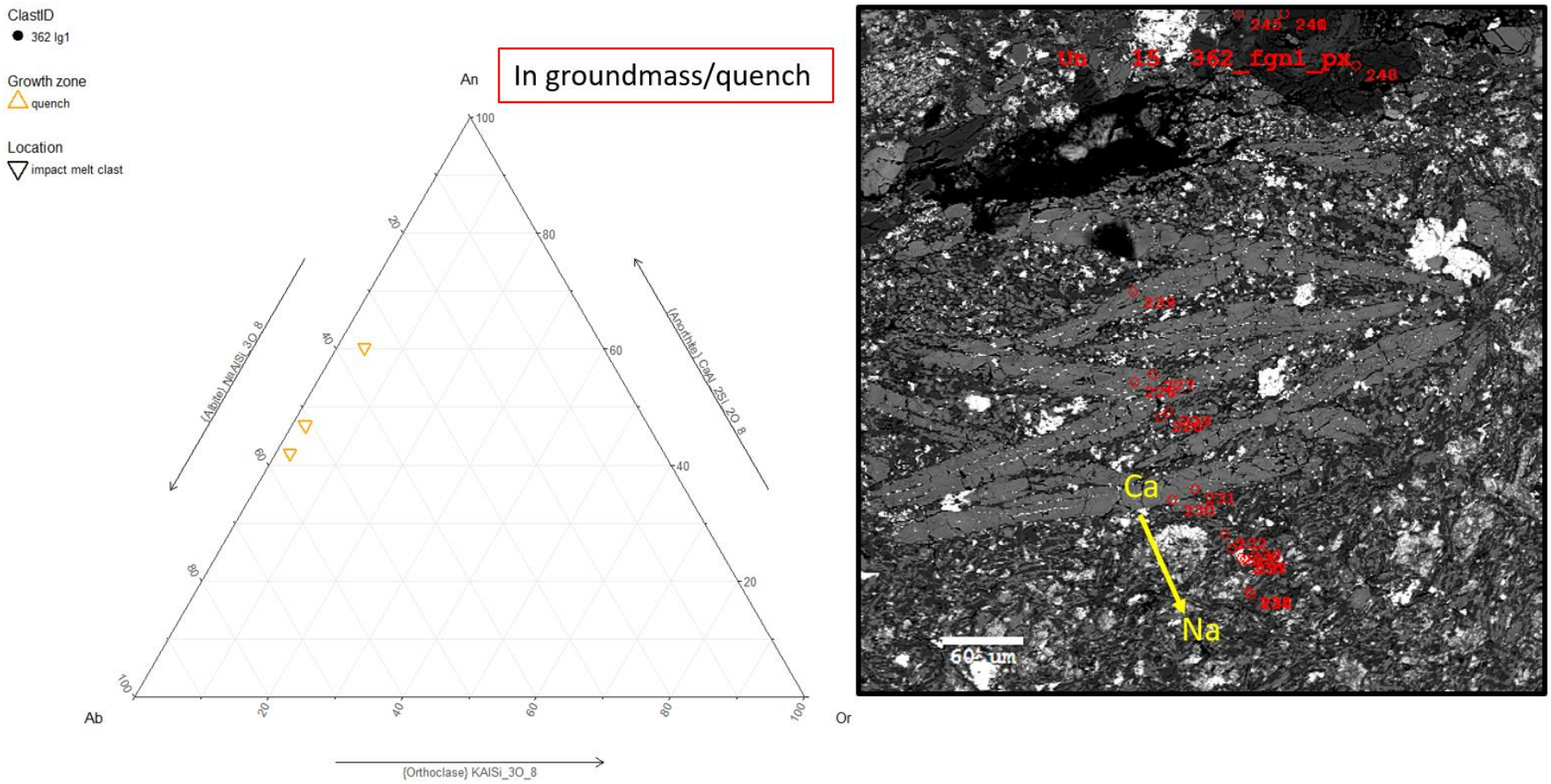

Figure 62: (Left) Composition of plagioclase in groundmass in lath grained enstatite spherule, based on normalized proportions of K, Ca and Na. Grid represents areas of stability for the separate feldspar components. Coloured outlines are used to give more detailed information about the sampling location within the clast. Shape gives clast location (matrix or impact melt clast). (Right) BSE image with electron microprobe sampling points (red) and zoning direction (yellow arrow).

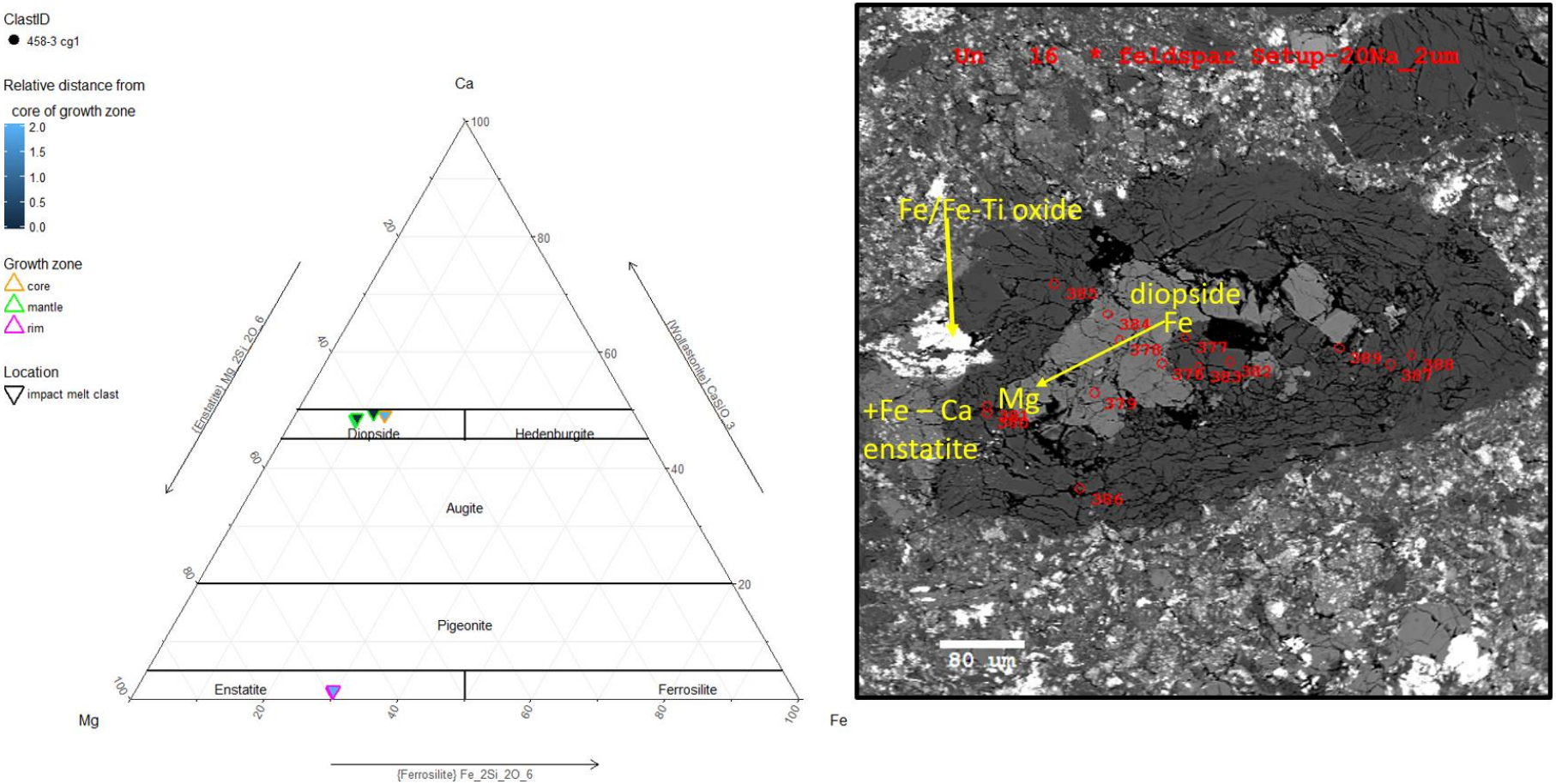

Figure 63: (Left) Pyroxene composition of diopside-plagioclase-enstatite spherule, based on normalized proportions of Mg, Ca and Fe. Grid represents areas of stability for the separate pyroxene components. Blue bar denotes relative distance from core of growth zone, with 0.0 (dark blue) representing the core, and 2.0 (light blue) representing the rim. Coloured outlines are used to give more detailed information about the sampling location within the clast. Shape denotes clast location (matrix or impact melt clast). (Right) BSE image with electron microprobe sampling points (red) and zoning direction (yellow arrow).

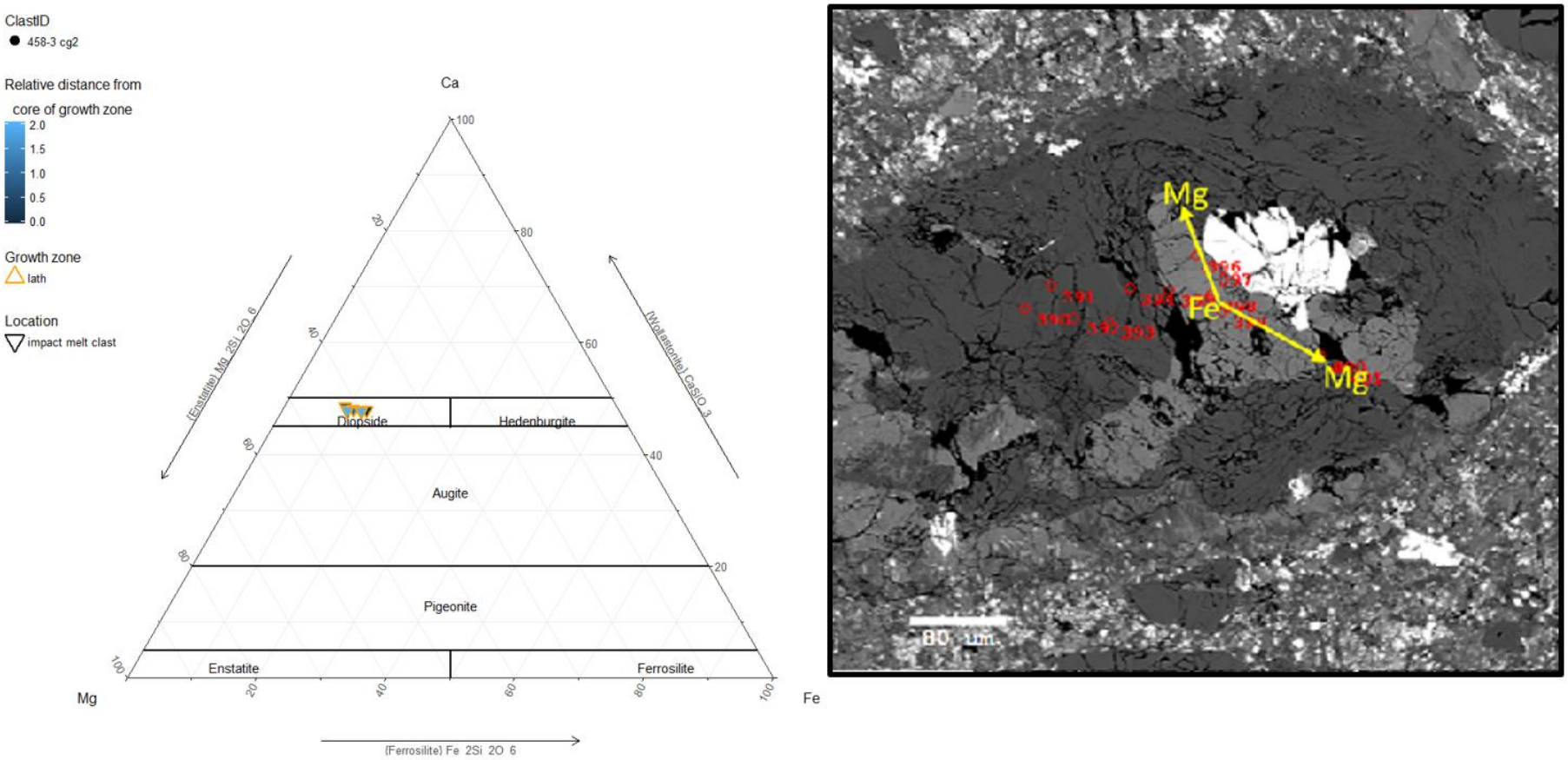

Figure 64: (Left) Pyroxene composition of diopside-plagioclase-enstatite spherule, based on normalized proportions of Mg, Ca and Fe. Grid represents areas of stability for the separate pyroxene components. Blue bar denotes relative distance from core of growth zone, with 0.0 (dark blue) representing the core, and 2.0 (light blue) representing the rim. Coloured outlines are used to give more detailed information about the sampling location within the clast. Shape denotes clast location (matrix or impact melt clast). (Right) BSE image with electron microprobe sampling points (red) and zoning direction (yellow arrow).

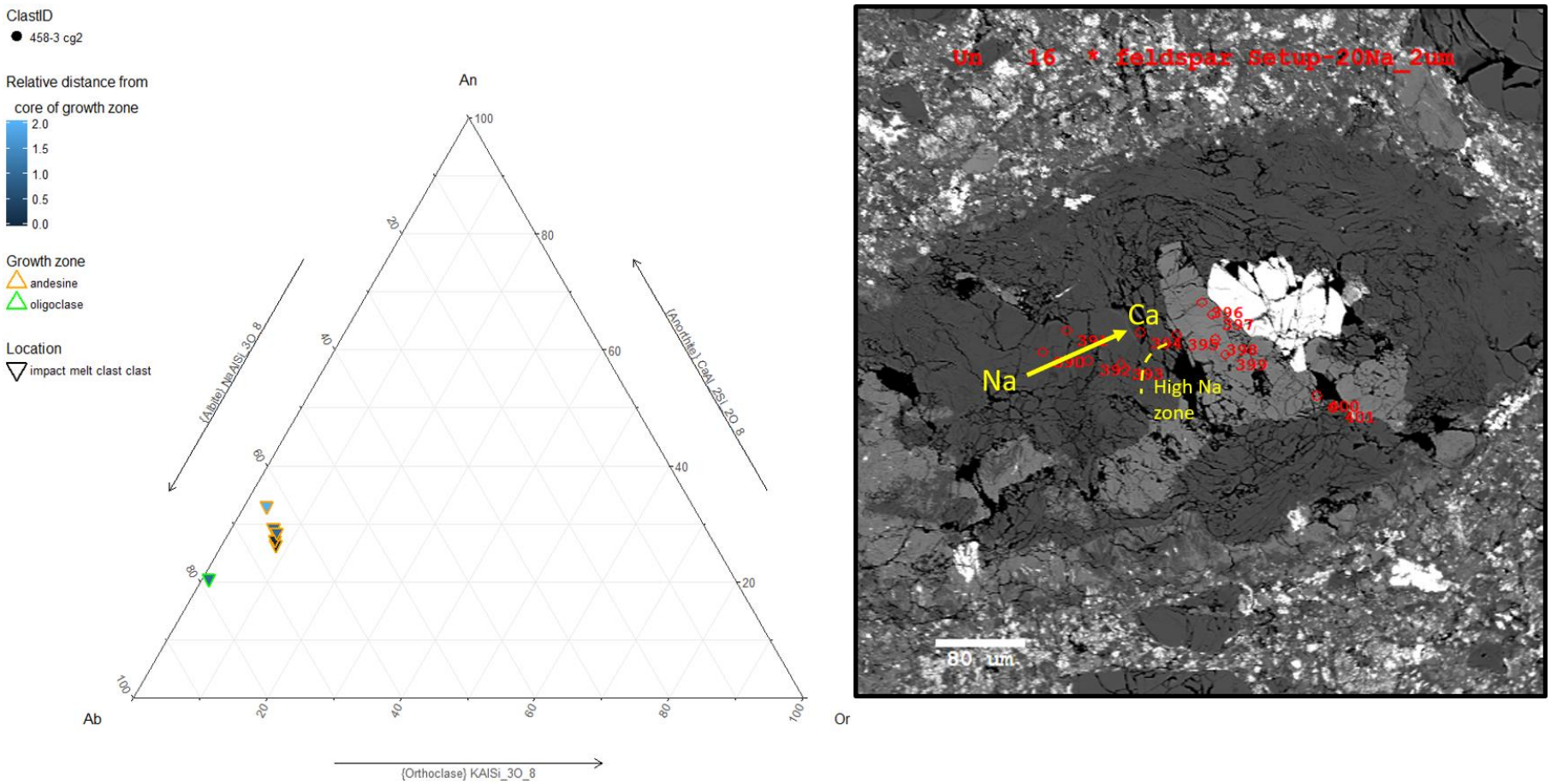

Figure 65: (Left) Feldspar composition of diopside-plagioclase-enstatite spherule, based on normalized proportions of K, Ca and Na. Grid represents areas of stability for the separate pyroxene components. Blue bar denotes relative distance from core of growth zone, with 0.0 (dark blue) representing the core, and 2.0 (light blue) representing the rim. Coloured outlines are used to give more detailed information about the sampling location within the clast. Shape denotes clast location (matrix or impact melt clast). (Right) BSE image with electron microprobe sampling points (red) and zoning direction (yellow arrow).

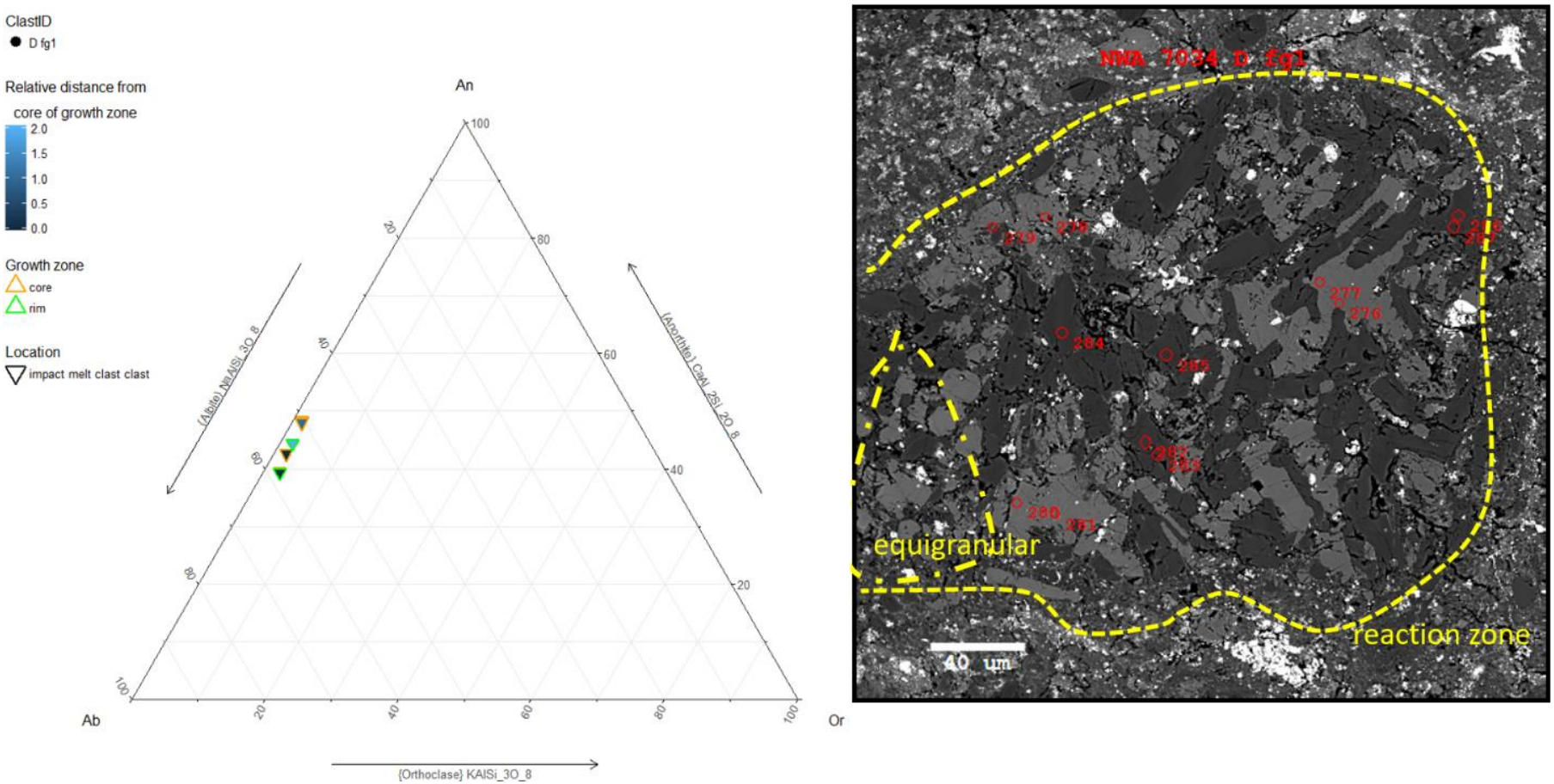

Figure 66: (Left) Composition of enstatite-plagioclase spherule, based on normalized proportions of K, Ca and Na. Grid represents areas of stability for the separate pyroxene components. Blue bar denotes relative distance from core of growth zone, with 0.0 (dark blue) representing the core, and 2.0 (light blue) representing the rim. Coloured outlines are used to give more detailed information about the sampling location within the clast. Shape denotes clast location (matrix or impact melt clast). (Right) BSE image with electron microprobe sampling points (red), zoning direction (yellow arrow). Note reaction zone (dashed line) and equigranular growth (dotted - dashed line).

4 DISCUSSION

This section relates the assembly of pyroxene and feldspar components to the circumstances and conditions that led to the genesis of the minerals inside of the meteorite and on the surface of Mars. Phase-temperature relations were based on Bowen's reaction series, and pyroxene- and feldspar thermometry (Bowen, 1922; Lindsley, 1983; Lindsley and Fuhrman, 1988). Pressure was assumed to be 1 atmosphere unless otherwise stated. Surface pressure on Mars has evolved over time, therefore this estimate is not realistic (Ehlmann *et al.,* 2011). To determine accurate pressure, impact velocity, regolith thickness, burial depth, and atmospheric thickness at formation should be considered for all components (Owen *et al.,* 1977). However, this information is not available.

Intergranular relationships between minerals in clasts were used to estimate order of crystallisation (Bowen, 1912). Grain morphology and zoning allowed to pinpoint relative crystallisation rate and temperature amongst the clasts. Granular grains cooled at a slower rate than tabular, which in turn cooled slower than skeletal grains (Lofgren, 1974). Degree of angularity implied whether the crystal or clast grew from the melt or underwent transport and abrasion (Krumbein, 1941). It was assumed that angular clasts were likely to have grown from the surrounding groundmass. By identifying core to rim compositional zoning, it was possible to deduce that the melt had undergone changes in composition during crystallization (Bowen, 1913; Lindsley, 1983; Miyamoto *et al.,* 1985). Exsolution lamellae were useful in determining cooling rate, crystallization temperature and melt composition (Vance, 1962; Dowty, 1976; Lindsley and Andersen, 1983; Lindsley and Fuhrman, 1988; Shore and Fowler, 1996). In addition, shock microstructures, such as lamellar zoning against the grain's natural growth direction, were used as indicators of whether a grain had experienced one or more high pressure impacts (Stöffler, 1966; Leroux, 2001; Leroux *et al.,* 2016). Interpretations were compared to the predicted timeline in Table 1. Adjustments were made to compose a more realistic timeline.

4.1 GENESIS OF MINERALS AND CLASTS

Mineral and clast composition was similar throughout all samples. All were mafic and contained a high amount of microscopic iron oxides, to the extent that there was difficulty collecting electron microprobe data due to a charging effect deflecting electrons. Variation was in the distribution and quantity of phenocrysts and polymineralic clasts. They contained phenocrysts of plagioclase, orthoclase, pyroxene, ilmenite, chromite and pyrrhotite. Additionally, there were several types of polymineralic clasts, such as norite-pyroxenite, gabbronorite, norite, spherules, apatite-plagioclase, and ilmenite-plagioclase clasts. Gabbros and phenocrysts of plagioclase and pyroxene were most abundant and can be considered major clasts. This assemblage is typical of suevite, commonly found in impact craters on Earth, such as the Ries crater in Germany (Shoemaker and Chao, 1961). Main matrix matched the description of material labelled protobreccia by McCubbin *et al.,* (2016) and Nyquist *et al.,* (2016), who also analysed NWA 7034. Based on BSE images and Qemscan, the groundmass of the matrix was determined to be porphyritic, aphanitic, with intergranular intergrowth of plagioclase, pyroxene (enstatite and augite) and Mg-phyllosilicates. Qemscan identified phases in the groundmass plagioclase and pyroxene were confirmed by electron microprobing, however Mg-phyllosilicates were not found. This could be due Mg-Phyllosilicates only occurring along grain boundaries and due to their microscopic size, it was not possible to sample at such precision using a 20 nA beam. Qemscan sampling, sized at 1 µm, may have falsely identified an overlap of pyroxene and plagioclase as Mg-phyllosilicate. Nonetheless the Qemscan's identification could be accurate

as Muttik *et al.,* (2014) identified a clay in the groundmass along plagioclase and pyroxene grain boundaries by Transmission Electron Microscopy (TEM).

Groundmass that differed in composition, texture, or grainsize was deemed a fossil impact melt clast, allowing clast locations to be divided into *matrix* and *impact melt clast*. This was done by human eyes. While it worked for the majority of clasts, this was an imperfect system, allowing for subjectivity, and could be improved upon by computer automatization.

Thanks to Qemscan images, it was possible to compare the composition of the matrix groundmass with the impact melt groundmass. Impact melt clast groundmass had a higher augite/enstatite ratio than the matrix groundmass. This implies that the matrix pyroxenes crystallized at a lower temperature at ~<1100˚C, compared to ~<1400˚C - 1100˚C for the impact melt pyroxenes (Lindsley and Andersen, 1983). This may also explain the preservation of the impact melt clasts, as the heath from the impact was not high enough to entirely melt and convert all pyroxenes. Additionally, the impact melt clast groundmass contained a higher alkali feldspar/plagioclase ratio, however plagioclase was significantly more abundant than alkali feldspar percentage for both. Alkali feldspars typically precipitate at low temperature after the majority of plagioclase crystallized, however, if the source melt contains a significantly high proportion of alkalis, alkali feldspar precipitates alongside plagioclase (Yoder *et al.,* 1957; Morse, 1970). The grainsize in the impact melt clast groundmass was finer than in the matrix for the majority of clasts and frequently contained pyroxene quench. Exsolution zoning was often patchy, lamellae were thinner than in matrix phenocrysts. Tabular grains were common. These are indicators of a rapid cooling (Watts, 1804; Judd and Cole, 1883; Poldervaart and Hess, 1951; Lofgren, 1974). In conclusion, the impact melt clasts crystallized at high temperatures (~<1400˚C) from an alkali-rich melt that underwent rapid cooling. The lower proportion of alkali feldspar in the matrix implies that the matrix did not crystallize directly from melting the alkaline impact breccia, but was likely mixed with additional low alkaline material, such as tholeiitic basalt. These were more common in Mars' later history, such as the Amazonian, while alkaline basalts were widely distributed in the pre-Noachian (McSween, 2015).

4.1.1 Feldspar phenocrysts

Zoning patterns in feldspar crystals provide insights into their crystallisation conditions and processes (Bowen, 1913; Lindsley and Fuhrman, 1988). As more crystals get precipitated, melt composition changes. In the plagioclase (albite-anorthoclase) system the liquid at all temperatures is enriched in Na while the solids are enriched in Ca. But the lower the temperature of the system, the higher the Na content of the solids (Bowen, 1913). Same is true for the alkali (albite-orthoclase) system, where the melt becomes enriched in K (Yoder *et al.,* 1957; Morse, 1970). For the plagioclase system to maintain equilibrium, an exchange reaction occurs between the coupled ions:

$$Na^{+}Si^{4+} = Ca^{2+}Al^{3+} \qquad \text{(Bowen, 1913)}$$

by diffusion across the crystal-melt interface. As melt cools it gets more viscous and the ions less mobile, resulting in equilibrium no longer being maintained, which is displayed by core to rim zoning. Therefore it is referred to as the plagioclase continuous reaction series (Bowen, 1913). Consequently, it is rare to find plagioclase phenocrysts of homogenous composition, unless formed by gravitational settling where the solids drop to the floor of the magma chamber, such as in a plutonic setting (Bowen, 1913). Zoned phenocrysts are evidence of incomplete equilibrium balancing during fractional crystallization and therefore denote an extrusive magmatic origin or late-stage saturation of volatiles in the residual melt (Bowen, 1913; Vance, 1962).

Unlike the plagioclase series, the alkali series is not continuous, and therefore exhibits different zoning patterns. Perthite texture is the name given to orthoclase and albite exsolved from an originally homogeneous feldspar crystal (Michot, 1951; Heier, 1955). Exsolution denotes formation at low pressure (Yoder *et al.,* 1957; Morse, 1970). High pressure lowers the solidus (crystallisation temperature) and solvus (exsolution boundary). At >0.5 GPa these overlap, resulting in two compositionally distinct feldspars forming. According to Bowen's reaction series (Bowen, 1922) and the ternary feldspar cooling model (Yoder *et al.,* 1957; Lindsley and Fuhrman, 1988), alkali feldspars crystallize at low temperatures, <1000˚C, after all calcic plagioclase has been precipitated. Pure binary albite orthoclase systems are rare, typically all three components are present and play a role (Lindsley and Fuhrman, 1988) (Figure 67).

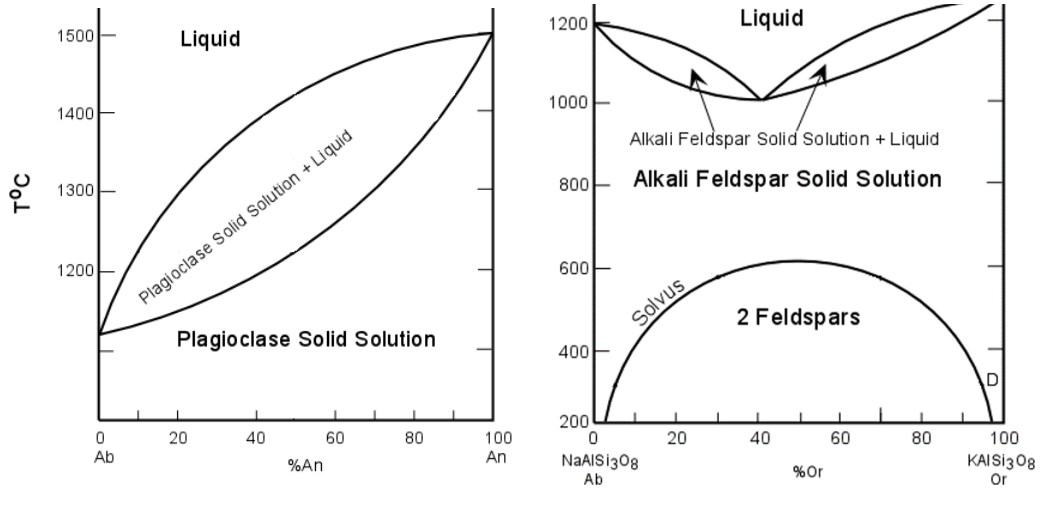

Figure 67: Binary phase diagrams of plagioclase series (right, redrawn from Yoder, 1957) and alkali feldspar series (left, redrawn from Bowen, 1928) at a pressure of 1 atm.

Info Box 1: Crystallization of feldspar in relation to Ca/Na/K composition and temperature.

Throughout the mounts sampled, calcic cores and sodic rims, known as “normal zoning”, were common for plagioclase phenocrysts. However, some plagioclases were homogenous in composition, implying they crystallised fast enough to precipitate before the melt composition changed (Bowen, 1913) (Info Box 1). These were generally smaller than the zoned plagioclases.

Further evidence for an extrusive origin of plagioclase phenocrysts in NWA 7034 is the absence of oscillatory zoning, which form by supersaturation of the melt in Ca, adjacent to growing crystals (Vance, 1962). Escaping volatiles prevent supersaturation, thereby equalizing rates of diffusion and crystallisation, resulting in normal zoning. Resorbed oscillatory cores may have occurred due to rapidly falling pressure, allowing for rapid crystallisation overriding the cores. While Vance described the mechanism behind the pressure chance and volatile release to be rising magma, in this case it was more likely impact induced.

One impact melt clast plagioclase exhibited homogenous composition but contained a more sodic component along a crack (Figure 20). Its glassy texture is in line with that of maskelynite, a plagioclase component commonly found in impact rocks (Tschermak, 1872). Maskelynite denotes high pressure (>300,000 atm, Stöffler *et al.*, 1986) shockwave induced quenching of a melt (Chen and El Goresy, 1997). The crack is evident of the clast having experienced brittle deformation, implying its source rock was located in the brittle zone of an impact basin (Grieve *et al.,* 1977; Caristan, 1982). Maskelynite more precisely places it in impact facies 3, as defined by Stöffler (1966) (Info Box 3). According to the plagioclase cooling model, it crystallized at 1265˚C ± 25˚C (Bowen, 1928; Lindsley and Fuhrman, 1988). As the adjacent clast was higher in Ca, it is inferred that the quenched melt was not hot enough to resorb the entire clast (Bowen, 1913).

Calcium feldspar (*anorthite*), forms at high temperatures (Bowen, 1913; Lindsley and Fuhrman, 1988). The only anorthite to be sampled, a labradorite, was contained in a quenched groundmass alongside a peridotite (Figure 56, Figure 69), implying an older origin than the matrix phenocrysts. Composition implies a crystallization temperature of 1225˚C ± 25˚C (Bowen, 1928; Lindsley and Fuhrman, 1988). Unlike the peridotite, the plagioclase phenocryst was well preserved with sub-angular edges well intact, homogenous composition, and no filled in cracks. The only alteration was a narrow reaction rim along clast boundary. The nearby peridotite was composed of olivine, with pyroxene along edges and cracks. This suggest that both phenocrysts grew from the same superhot melt, which then got quenched (rapidly cooled), resulting in a different chemical composition along the rim (Bowen, 1912, 1922; Krumbein, 1941). As labradorite is stable at lower temperatures than olivine, it was less overwritten by the cooling process (Bowen, 1922).

Sodic feldspar (*albite*) can precipitate in both the plagioclase and alkali system but represents the low temperature component in both (Bowen, 1913, 1922). However, at low pressure in a water-reduced system, it is unlikely to get a non-perthitic albite, therefore, the albites lacking exsolution lamellae likely formed in the plagioclase system (Yoder *et al.,* 1957; Morse, 1970). There is evidence that some albites found predate the matrix, while others grew from it. Angular shapes lacking reactions rims or normal zoning, imply that the clasts grew from the matrix they are contained in (Krumbein, 1941). This is supported by a phenocryst (Figure 22) having the same composition as plagioclase sampled from the nearby groundmass. Their compositions define a crystallization temperature range of 1210-1175˚C ± 25˚C (Bowen, 1928; Lindsley and Fuhrman, 1988). Phenocrysts with concave indentations, reaction rims, normal zoning and cracks containing new growth phases are more likely to pre-date the matrix and were altered and in part resorbed by hot melt (Bowen, 1912). According to the plagioclase cooling model this occurred at 1210-1140˚C ± 25˚C (Bowen, 1928; Lindsley and Fuhrman, 1988). From the wide temperature range and intergrowth of different components, it can be inferred that the clast underwent slow cooling (Lindsley and Fuhrman, 1988).

All alkali feldspars phenocrysts found had exsolution making them *perthites* (Michot, 1951). This texture is evident of crystallization at low pressure, <5000 atm, and low temperature, ≤1000˚C ± 50˚C (assuming 1 atm) (Yoder *et al.,* 1957; Morse, 1970). Perthite phenocrysts were more abundant in impact melt clasts than in the matrix. They had irregular intergrowths of potassium rich orthoclase and sodium rich albite, rather than ordered lamellar exsolution, implying rapid cooling (Poldervaart and Hess, 1951). An exception was clast 362 pl (c)2, which had both (Figure 17). Since neither orthoclase nor albite was dominantly present, these were classified as mesoperthite (Michot, 1951). The presence of alkali feldspar suggests that the basaltic clast they are contained in is remnant of alkali volcanism on Mars, which would make these phenocrysts Pre-Noachian, >4.4 Ga old, predating the remaining clasts in NWA 7034 (McCubbin *et al.,* 2016). However, without dating, one cannot say for certain. It is possible alkali volcanism went on for longer than previously assumed.

Qemscan identified the surrounding groundmass of these clasts to be high in augite as opposed to the main matrix, implying a different age and origin. Melt clasts that contained these perthite phenocrysts were frequently crosscut by veins that had been filled with Fe-Ti oxide and unidentified phases. An unknown phase also appeared to crosscut perthite, and physically displace a vein (Figure 15). This vein was also crosscut by an ilmenite (Figure 16). This implies the formation of the ilmenite and unknown phase supersede both the crystallisation of the perthite clasts, the groundmass they are contained in, and subsequent veins crosscutting, but not the main matrix emplacement (Bowen, 1912). Consequently, some sort of event, possibly heating, had to have occurred for this new phase to crystallize from the groundmass (Bowen, 1912). The ilmenite limits the temperature range, as ilmenite can form at temperatures as low as 550˚C, while perthites of the compositions recorded would start melting at >1000 ˚C (Yoder *et at.,* 1957; Buddington and Lindsley, 1964). Clast boundaries of perthites were well defined. Phenocrysts were sub-rounded to sub-angular but no reaction rims or core to rim zoning characteristic of contact metamorphism were present. Groundmass along clast boundary was deformed (Figure 16). These observations make it likely the phenocrysts grew in the groundmass which was elastically deformed by the growing clasts, rather than being rounded by physical processes prior to being enclosed in the matrix (Krumbein, 1941). The matrix around the clasts exhibited iron oxides and other phases arranged in sinusoidal shapes, which is indicative of elastic deformation while the matrix was in a plastic state but not hot enough to resorb the perthite, which likely occurred in the same event the ilmenite formed. Plastic deformation implies that alkali feldspar containing melt clasts were igneous in nature, rather than stemming from an impact, which matches alkali basalt's extrusive history (Werner, 2009; Yin *et al.,* 2014).

Qemscan identified the vein to be filled with Fe-Ti oxide, Fe-Ti hydroxide and an unknown phase, which suggests that the parent body experienced hydrothermal activity after it had fully crystallised (Phillips, 1879; Goderis *et al.,* 2016). Mars had the most active volcanism in the Pre-Noachian and early Noachian (Werner, 2009), and hydrothermal sub-circulation seized ~3.75 Ga (Ehlmann *et al.,* 2011), which would suggest a >3.75 Ga age for both the matrix these clasts are contained in in, and the veins crosscutting it. Veins did not crosscut the matrix that these clasts were melt clast were contained in, making the veins pre-date breccia formation at 2.1 Ga (Agee *et al.,* 2013), limiting their formation age >2.1 Ga, and the metamorphic process that led to ilmenite growth to ~3.75 - 2.1 Ga.

4.1.2 Pyroxene phenocrysts

Ca/Mg/Fe distribution in pyroxenes is said to be primarily driven by temperature, therefore their ratio can be used as an indicator of cooling rate and temperature at crystallization. Both diffusion reactions are not strongly affected by pressure (Kretz, 1963, 1982).

In a pure pyroxene system, at equilibrium:

$$MgSiO_3 + CaFeSi_2O_6 = FeSiO_3 + CaMgSi_2O_6$$

$$(Mg)orthopyroxene + (Fe)clinopyroxene \ = (Fe)orthopyroxene + (Mg)clinopyroxene$$

(Kretz, 1982)

A shift to the left or right means that equilibrium could not be achieved.

It is known that Ca content of low Ca pyroxene phases increases with increased temperature, while Ca content of high Ca phases decreases (Poldervaart and Hess, 1951; Lindsley and Andersen, 1983). Poldervaart and Hess (1951) recorded that both high and low Ca phases could coexist in equilibrium in solid solution in a saturated basalt melt, allowing for the crystallisation of either enstatite/ferrosilite or diopside/hedenburgite. They predicted that subsequent slow cooling allowed for the exsolution of the two mentioned components in one crystal, whereas rapid cooling would result in homogenous composition. Homogeneity denotes degree of metamorphism, where high homogeneity implies high degree of metamorphism (Miyamoto et al., 1985).

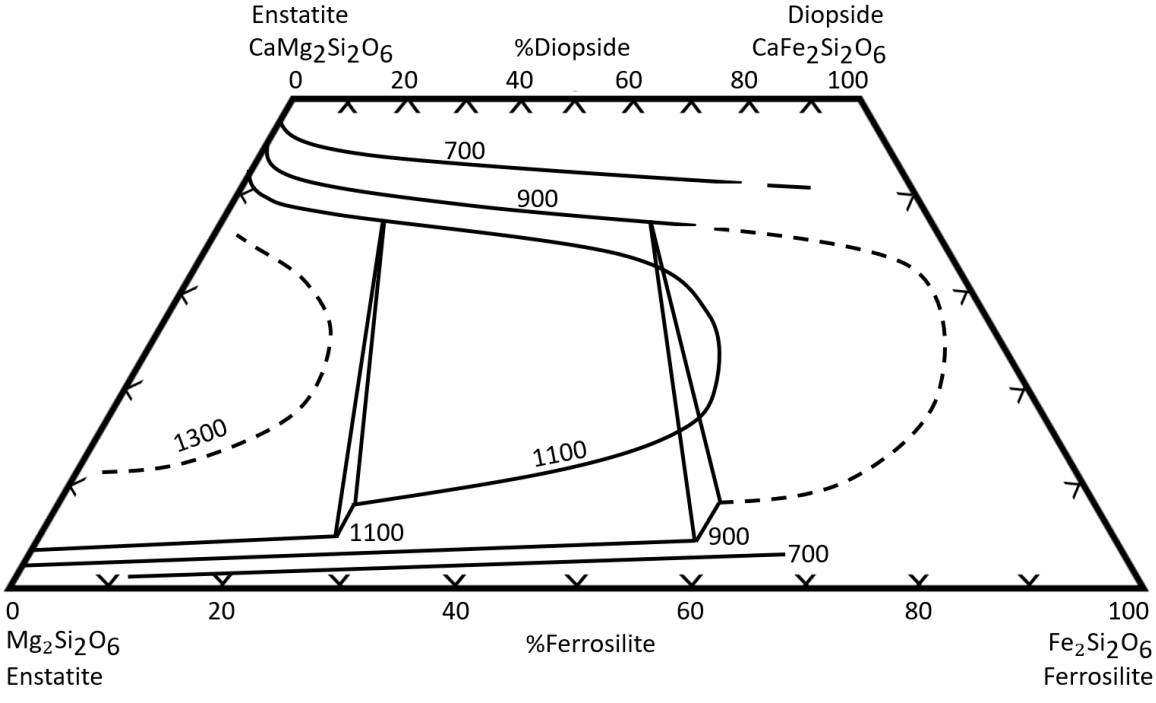

Figure 68: Temperature dependent pyroxene compositions at a pressure of 1 atm, with isotherms in ˚C (redrawn from Lindsley, 1983).

Info Box 2: Crystallization of pyroxene in relation to Ca/Mg/Fe composition and temperature.

Both low and high Ca phases were equally common throughout the mounts, however, Mg pyroxenes were much more abundant than Fe pyroxenes (Figure 13). No hedenburgite was found, and the few ferrosilites plotted close to the cut-off point of being defined as enstatites, meaning the source melt was enriched in Mg relative to Fe (Kretz, 1982; Lindsley, 1983) (Info Box 2). Most pyroxene phenocrysts exhibited core to rim zoning of Fe to Mg. This implies that the melt became more enriched in Mg relative to Fe as it cooled (Kretz, 1982). Likely because the Fe was being used up by other phases, such as Fe-oxides and Fe-Ti-oxides, which start crystallizing at ≤1070˚C (Wright and Okamura, 1977). Qemscan maps showed these to be abundant (Figure 10, Figure 12). Corona of very fine-grained iron oxides (<5 µm) commonly surrounded the phenocrysts implying that these grew rapidly, while pyroxenes grew magnesic rims in order to preserve compositional equilibrium. The matrix contained a wide range of phenocrysts, which were for the most part zoned, meaning they underwent little to no metamorphism (Miyamoto *et al.,* 1985).

The two-pyroxene thermometer created by (Lindsley and Andersen, 1983) was used to estimate crystallization temperature range. Pressure was assumed to be 1 atm. Results were determined graphically, they were precise to ± 50˚C for augites and pigeonites, and ± 100˚C for orthopyroxenes. High temperatures imply a source melt origin close to the impact epicentre (Stöffler, 1966) (Info Box 3). Zoning was used as an indicator for crystallization rate. For the Ca-rich phase to separate as exsolution lamellae of calcic pyroxene, time was needed. Therefore, the presence of lamellae suggests a slow cooling rate, relative to pyroxenes without exsolution (Poldervaart and Hess, 1951). Alternatively, the lamellar intergrowths may be a shock induced microstructure that were produced by a nearby impact while the phenocrysts were in the brittle zone of the impact basin (Stöffler, 1966; Leroux, 2001).

Clasts containing lamellar intergrowths of three distinct compositions were identified. These were: intergrowths of pigeonite-augite, low- and high Ca augite, and augite-orthopyroxene. Pigeonite typically breaks down into orthopyroxene and augite, as it is not compositionally stable, and as such rarely preserved in slow cooling processes (Poldervaart and Hess, 1951). Therefore, the pigeonite-augite clasts underwent the fastest cooling and the augite-orthopyroxene clasts the slowest. Low- and high Ca augite intergrowths were likely the first to form out of the matrix pyroxenes, as they are the highest temperature polymorph, crystallizing at 1200-600˚C ± 50˚C (Lindsley and Andersen, 1983).

Pigeonite-augite clasts were sub-angular with monoclinic crystal face intact, intersecting at ~120˚, making them easily identifiable as a clinopyroxene. The composition suggested they crystallised at 1150-950˚C ± 50˚C (Lindsley and Andersen, 1983). The sampled clast was heavily fractured, meaning brittle deformation occurred, so it likely was in solid state during impact (Stöffler, 1966). Zoning occurred in the form of exsolution lamellae and core to rim (Fe to Ca). Pigeonite was found in the core, and augite along the rim. Meaning it cooled too fast for all pigeonite to be broken down via exsolution lamellae (Poldervaart and Hess, 1951).

Augite-orthopyroxene clasts were the lowest temperature polymorph. They crystallized at 1000 ± 50˚C - 600 ± 100˚C (Lindsley and Andersen, 1983). Their crystallization temperature range and advanced composition imply they were last to form out of the three types.

One unique clast was as *enstatite with intergrowths of ferrosilite and augite* (Figure 31). This phenocryst was heavily zoned with patchy areas of augite, enstatite and ferrosilite. The messy zoning indicates rapid cooling (Poldervaart and Hess, 1951). Crystallization was estimated to occur at 1000-600˚C ± 100˚C (Lindsley and Andersen, 1983). A 100 µm section at the bottom of the clast recrystallised as an equigranular plagioclase, pyroxene and iron oxide intergrowth, that was identified as gabbronorite. This suggests the clast experienced a high degree of contact metamorphism, where the temperature and/or pressure

change was large enough to induce the growth of plagioclase (Bowen, 1912, 1922). This clast may represent a pre-stage to the microcrystalline gabbronorite clasts found in the matrix. In support of this theory, the clast was sub-rounded, a feature that was shared by many gabbronorite clasts found in NWA 7034. Furthermore, sub-roundedness is indicative of this clast not having crystallised in the matrix immediately surrounding it, but having formed at an earlier point and later having been rounded by abrasion or transport (Krumbein, 1941). A zone of increasing grainsize, and decreasing iron oxide content, in the matrix, away from the clast suggests that recrystallisation of the melt did occur, however, the gabbronorite growth within the clast itself suggests that there were multiple processes, possibly two separate re-heating events, that this clast may have experienced. The clast exhibited twinning in the (001) orientation. This is commonly found in shocked clinopyroxene in meteorites (Ashworth, 1980; Leroux, 2001). Alternatively, twinning could have formed by static deformation at high strain rate (Kirby and Christie, 1977), but formation by impact melt matches the known history of NWA 7034.

Enstatites in the matrix occurred as sub-angular clasts with well-defined clast boundaries, indicative of having grown from the melt (Krumbein, 1941). The compositional range of the phenocrysts was narrow (< 5% variation), indicative of having crystallised from a low temperature melt at a rapid cooling rate (Poldervaart and Hess, 1951). This was confirmed when plotted in the cooling model of Lindsley and Andersen (1983), which yielded 1100-1000˚C ± 100˚C for one sample, and 850-750˚C ± 100˚C for the other. One of the clasts exhibited core to rim zoning from Fe to Mg (Figure 33), indicating the melt underwent compositional changes, likely due to degassing of volatiles (Vance, 1962). Fe-oxides were concentrated in the groundmass near the clast. These phases likely formed from the excess Fe that was made available when the magnesic rim formed (Kretz, 1982). Phenocrysts were heavily to moderately fractured, with fractures occurring primarily at 90˚ for one and at ~120˚ and ~˚60 for the other clast (Figure 32, Figure 33), indicative of the propagating shock wave orientated against to the primary growth direction (Stöffler, 1966). One of the phases contained a lath shaped inclusion about 5 µm long. The inclusion was found at the centre of a grain at the centre of the clast, overgrowing the pyroxene and therefore postdating it (Bowen, 1912). Qemscan identified this as an unknown Fe-oxide phase. This inclusion may have crystallised from the resorbed core in order to balance an excess of Fe, or precipitated as part of hydrothermal processes (McCubbin *et al.,* 2009).

High Ca augites with low compositional range (<5%) crystallised from a low temperature melt, 850-800˚C ± 50˚C, at a rapid rate (Poldervaart and Hess, 1951; Lindsley and Andersen, 1983). These likely formed in solid solution with the enstatite phenocrysts. Like the enstatites, they were lightly fractured compared to other pyroxene phenocrysts, which indicates that the clast underwent a compositional change recently, most likely the conversion of pigeonite to augite, resulting in fractures being overprinted. Their crystallisation conditions match a history of having crystallised from solid rocks that were molten due to being located in the melt zone of an impact (Stöffler, 1966). Likely by the same impact that formed the matrix. The clast was speckled with inclusions that increase in quantity towards the edge. This is likely the result of a rapid compositional change, where the system was not able to balance Fe and Mg fast enough, and formed these inclusions, rather than replace the composition of the entire phenocryst (Bowen, 1912; Kretz, 1982; Lindsley, 1983).

In summation, the composition and zoning patterns of pyroxene phenocrysts indicate that the parent body that would later form the matrix was located in the partially molten zone of an impact basin according to the zones defined by Stöffler, 1966. This zone was superheated to minimum 1200˚C ±50˚C and then rapidly cooled. First to form were exsolved augites and pigeonites, then enstatites and high Ca augites when it cooled to about 1000˚C ± 100˚C and continued cooling at a slower rate (Poldervaart and Hess, 1951; Lindsley and Andersen, 1983).

Pyroxene phenocrysts in impact melt clasts were distinguished from the matrix phenocrysts, as they were found inside of melt pockets, denoting an older age (Norton, 1917). It is likely that these clasts remained from a previous generation impact and can therefore provide a compositional and physical framework for how an earlier generation source magma or source melt might have evolved (Santos *et al.,* 2015; Goderis *et al.,* 2016).

All pyroxenes sampled by electron microprobe fell in the *enstatite* range, indicating crystallisation from a low temperature melt: 1050-1000˚C ± 100 ˚C and 800-700 ˚C ± 100 ˚C (Lindsley and Andersen, 1983). Pyroxenes frequently had exsolution lamellas, though not as defined those found seen in matrix pyroxenes, suggesting a slow cooling rate (Poldervaart and Hess, 1951). Alternatively, these may also be shock microstructure as described by Leroux, 2001, and therefore unrelated to cooling rate. However, the direction of fracture propagation did not align with that of lamellae (Figure 35, Figure 36). Fractures imply deformation occurred in cooled, brittle state (Caristan, 1982). This suggests they underwent at least two impact events. The first impact likely produced the melt out of which these phenocrysts grew. These were then contained within or a zone that was far away to not be entirely re-molten but close enough to be altered by the shock front of the second impact event, likely facies 2 (Stöffler, 1966). However, this interpretation is based on two clasts, that were sampled near each other. Sample size needs to be increased and other minerals in the proximity need to be analysed to draw more accurate conclusions about the melt composition.

Both clasts maintained a vaguely trapezoidal shape and could be classed as angular, indicating that they grew from the melt they were contained in (Krumbein, 1941). The crystal face of one clast (Figure 35) was not intact, implying it was resorbed by the surrounding melt. Defined, straight edges remained at the Mg-rich lamellae, which appeared to hold up better than the Fe-rich phase, implying it was more stable. This indicates the melt was saturated in Mg and an exchange reaction took place in which Fe and Mg were diffused across the crystal melt interface in order to preserve equilibrium (Kretz, 1982).

A nearby phenocryst contained in a separate impact melt clast had a more Mg-rich composition (Figure 36). Its clast boundaries were more clearly defined, supporting the previous assumption that this Mg-rich phase was more stable than the Fe-rich phase. Nonetheless there were localised reaction zones, particularly spread along the clast edges where unknown phases formed, likely metal oxides. Additionally, there are bright inclusions, which could be metal oxides, or more interestingly, a source of rare earth elements (Santos *et al.,* 2013). Contact metamorphism altered mineral phase composition along clast boundaries and within fracture zones (Miyamoto *et al.,* 1985).

As both phenocrysts were sampled from mount D, close to each other, it is likely that the impact melt clasts that contained them originated from the same crystallisation event. The source melt was Mg-rich and possibly depleted in Ca, as indicated by the low abundance of augites and diopsides. Mg and Fe rich phases, such as pyroxene, were first to form and rapidly grew to large phenocrysts (Bowen, 1922). The system reached the point where the majority or all of Fe had already been incorporated into pyroxenes and was no longer available for other phases, while there was still an abundance of Mg. To make Fe available, it had to be sourced from already existing phenocrysts, and was replaced with Mg. However, the system cooled too quickly, and not all Fe in Fe-rich pyroxenes could be replaced (Kretz, 1982).

An additional impact melt pyroxene was sampled from mount A (Figure 37). Like the impact melt pyroxenes in mount D, this was an Mg-rich enstatite, indicating it cooled from a low temperature melt: 1100-1050˚C ±100˚C (Lindsley and Andersen, 1983). It did not exhibit exsolution lamellae, making it likely it was quenched (Poldervaart and Hess, 1951). Like the pyroxenes in D, it had parallel fractures, possibly

brittle deformation induced by an impact shock wave propagation (Leroux, 2001). Unlike those found in D, these were only one-directional, likely originating from the matrix-forming impact.

What is striking is that the pyroxene in mount A exhibited core to rim zoning of Mg to Fe, meaning the melt was enriched in Fe over Mg as it cooled (Kretz, 1982). The opposite pattern of the phenocrysts found in the impact melt clasts in mount D. This provides further evidence that NWA 7034 contains impact melt clasts sourced from more than one origin. Unfortunately, many of the samples taken from phenocrysts in impact melt clasts could not be used in the analysis due to bad totals and other problems with data collection. It would be useful to focus on sampling impact melt clasts to figure out if any major elemental components were overlooked. Sampling in grain cores only might improve the quality of data obtained.

4.1.3 Gabbroic clasts

4.1.3.1 Norite pyroxenite

A *Norite-pyroxenite* clast only appeared once in all the mounts analysed. What made this clast special is that it was the only alkaline basalt clast found throughout the sampled mounts. An alkaline basalt clast had been previously identified in NWA 7034 and dated to be 4.72 ± 0.23 Ga (McCubbin *et al.,* 2016). This clast is likely of a similar age. Furthermore, the clast was composed of a norite joint to an orthopyroxenite along a clearly defined boundary. Its appearance is akin to that of cumulate clasts, typically found at the bottom of magma chambers (Wager *et al.,* 1960). These form as heavier minerals drop out of the melt and are thereby sorted by mass. This allows for norite to be deposited on top of orthopyroxenite. Norite is a mafic intrusive igneous rock, defined as an assemblage of orthopyroxenes and plagioclase, where orthopyroxene makes up >80% (amongst the two minerals), and is composed primarily of orthopyroxenes, rather than clinopyroxenes (Bayley, 1888). Pyroxenite is an ultramafic rock consisting of >90% pyroxene, whereas an orthopyroxenite is defined as a pyroxenite containing predominantly orthopyroxene with minor or no clinopyroxene (Streckeisen, 1974). The norite section was an equigranular intergrowth of feldspar (albite and orthoclase) and pyroxene (enstatite), implying that the growth of both minerals was favoured equally by the system (entailing composition and temperature of the melt). In the pyroxenite section, feldspar grains were embayed in the pyroxene, which implies that the system favoured the growth of orthopyroxenes but shifted towards allowing plagioclase to form (Bowen, 1912). This suggests a change to the system, either a change in the melt composition from ultramafic to mafic, after it was depleted in Mg and Fe, or a temperature change (Wright and Okamura, 1977; Kretz, 1982). Grains in the pyroxenite section had core to rim zoning from Fe to Mg, implying the Mg/Fe ratio increased as the melt cooled, or that contact metamorphism occurred (Kretz, 1982). The norite contained plagioclase while the pyroxenite had alkali feldspar, which generally forms at lower temperatures. The composition denotes a crystallization temperature of ≤1180˚C ± 50˚C for the alkali feldspar (Yoder *et al.,* 1957; Morse, 1970), 1210-1195˚C ± 25˚C for the plagioclase (Lindsley and Fuhrman, 1988), and 1100-1000˚C ± 100˚C for the pyroxene (Lindsley and Andersen, 1983). These imply crystallization occurred at 1210-1000˚C ± 100˚C for the norite, and at ≤1180 ± 100˚C for the pyroxenite. As these temperatures overlap one cannot say with certainty that the phase change in the rock was temperature driven. The clast was contained in the matrix. However, this does not mean that it formed recently or that alkali volcanism extended for longer than previously expected. It is more likely that it was integrated in the most recent assimilation. The clast is rounded, implying that it cannot have grown in the matrix melt, but rather that it had been exposed, possibly due to an earlier impact, erosion, weathering, or a combination of these, and then transported and heavily abraded, allowed for its perfectly rounded shape (Krumbein, 1941).

4.1.3.2 Gabbronorite

Gabbronorite a was the most commonly found polymineralic clast type. It was characterised by equigranular intergrowth of feldspar and pyroxene, implying that the growth of both minerals was congenital and favoured equally by the system (entailing composition and temperature of the melt) (Bowen, 1912) (Figure 41). Two of the clasts sampled had a wide compositional range and therefore crystallization temperature range, of 1160-600˚C ± 50˚C and 1000-550˚C ± 50˚C, indicating slow cooling (Bowen, 1928; Lindsley and Andersen, 1983; Lindsley and Fuhrman, 1988). The rest had a small compositional range and therefore small (<50˚C) crystallization temperature range, 1100-1000˚C ± 50˚C for pyroxene and 1225-1160˚C ± 25˚C for plagioclase (Figure 40). The lack of overlap does not imply that pyroxene growth superceded that of plagioclase, but is more likely due to a lack of precision of the models, or not accounting for pressure (Lindsley, 1983; Lindsley and Fuhrman, 1988).

Gabbronorite b was the second most commonly found polymineralic clast type. It was characterised by its porphyritic texture and cryptocrystalline grainsize, which is small, relative to other gabbronorites found (Figure 43). Change in grainsize denotes a change in nucleation and cooling rate (Shaw, 1965). Electron microprobing of a sample identified the pyroxene as enstatite of narrow (<5%) compositional range, indicating rapid crystallization (Poldervaart and Hess, 1951). Composition denotes a crystallization temperature of 1100-1000˚C ± 100˚C (Lindsley and Andersen, 1983). However, only two sampling points yielded good totals, so it is impossible to make assumptions about directional zoning. The surrounding groundmass was porphyritic, cryptocrystalline and intergranular, making it hard to differentiate the clast from the groundmass. The textural similarity between clast and matrix suggests it might have been grown from the same melt. Microprobing of the surrounding groundmass might give clarity.

Gabbronorite c had lath grains of plagioclase contained in anhedral pyroxene, with pyroxene lath grains of a different composition cross cutting both, implying secondary growth, postdating them (Bowen, 1912) (Figure 44). There were poikilitic iron oxides scattered throughout that also crosscut the anhedral pyroxene and plagioclase, but not the lath grains, meaning they might have formed simultaneously. In the sample probed the pyroxene lath grains were higher in Fe, relative to the anhedral pyroxene, which supports the theory that they formed together with the iron oxides (Kretz, 1963) (Figure 45). The anhedral pyroxene was strongly zoned with a compositional variability of ~25% from core to rim (Ca to Mg), implying the melt that it grew from crystallised slowly at a large thermal range (Poldervaart and Hess, 1951). This is reflected by the cooling model, yielding 1225-800˚C ± 100˚C for the anhedral pyroxene and 1100-1000˚C ± 50˚C for the lath grain superimposing it (Lindsley and Andersen, 1983). This confirms the cooling history implied by their textural relationships. Clasts had elongated shapes with uneven clast boundaries. The feldspar also had a large compositional range, both albite and orthoclase were present. Cooling models yielded crystallization temperatures of 1225-1160˚C ± 25˚C for the plagioclase and 1140-1080 ˚C ± 50˚C for the alkali feldspar (Bowen, 1928; Yoder, Steward and Smith, 1957; Lindsley and Fuhrman, 1988). Clasts of similar composition were found in the nearby matrix, which suggests that clasts of these types grew from the matrix melt. This implies the matrix had some high K feldspar components, which contradicts the matrix composition implied by other polymineralic clasts and phenocrysts that were believed to have grown from it. So far, alkali right feldspar was primarily identified in impact melt clasts. A possible explanation could be that in the location where the clast grew, a high K phase had been molten and recrystallised.

Gabbronorite d was made of lamellar pyroxene, plagioclase and pyroxene xenocrysts (Figure 47). The lamellar pyroxene had intergrowths of enstatite and pigeonite, denoting a crystallization temperature range of 1025-900˚C ± 100˚C (Lindsley and Andersen, 1983). Twinning occurred at 120˚. Twins may have formed due to impact induced high pressure shock metamorphism (Stöffler *et al.*, 1986). Alternatively,

slightly different compositions (<%5 variation in Fe and Ca) of the twins suggests that pyroxene crystals could have drifted together in a fluid medium to combine into a twinned cluster (Prasad and Naidu, 1971). There was plagioclase (sanidine) along the outside of the pyroxene, superimposing the pyroxene. Rounded and angular xenoliths of pyroxene were contained in plagioclase and pyroxene, crosscutting and superimposing it, indicating they crystallised later, possibly due to two-stage heating (Bowen, 1912). Plagioclase composition yielded a crystallization temperature of 1190˚C ± 25˚C (Lindsley and Fuhrman, 1988). Plagioclase clasts with similar xenoliths of pyroxene were found nearby in the matrix. The clast was angular. This implies it grew from the matrix melt and could therefore be used to approximate composition and cooling history of the matrix (Krumbein, 1941).

4.1.3.3 Apatite-/ilmenite-plagioclase

Apatite-plagioclase clasts were common throughout the mounts sampled. Often, clasts contained intergrowths of ilmenites and/or pyrrhotites as well (Figure 48, Figure 49, Figure 50). Ilmenite can crystallize at a range of 1300-550˚C (Buddington and Lindsley, 1964). Since their composition was not sampled, textural relationships and plagioclase compositions were used to more precisely limit clast formation temperatures. Grain boundaries between plagioclase and ilmenites were angular, implying congenital growth, and embayed between apatite, implying apatite grew later (Bowen, 1912). Plagioclase compositions yield crystallization temperatures of 1280-1170˚C ± 25˚C (Bowen, 1928; Lindsley and Fuhrman, 1988). At lower temperatures, apatite started forming. Presumably at ≤1030˚C (Wright and Okamura, 1977). This allowed the excess Ca to be integrated, when temperatures were too low for pyroxene to be stable (Bowen, 1922). This denotes a crystallization temperature range of 1280˚C ± 25˚C to ≤1030˚C for the clast. Some clasts had ilmenite and plagioclase grains growing in equigranular shapes (Figure 48) others in lath shapes (Figure 49). A faster growth rate can be inferred for the latter (Lofgren, 1974). Some clasts contained alkali feldspars, indicating they formed during times of alkaline volcanism (McCubbin *et al.*, 2016). This suggests at least two separate origins for apatite plagioclase clasts, where they formed under different conditions and compositions. It was common for these clasts to be heavily fractured or have bent lath grains, indicating clasts underwent brittle and ductile deformation (Caristan, 1982). Possibly formed by propagation of an impact induced shockwave (Stöffler *et al.*, 1986). Further support for this were coronas along rim and filled in cracks containing interstitial pyroxene, Mg-phyllosilicates and unknown phases, denoting a recrystallised, quenched melt associated with shock metamorphism (Stöffler *et al.*, 1986).

4.1.3.4 Gabbro

In *gabbro* clasts, the pyroxene component was augite, denoting a slower cooling rate, relative to gabbronorite clasts (Poldervaart and Hess, 1951). Augite was paired with sodic or potassic feldspar, denoting intermediate to low crystallization temperatures (Yoder *et al.,* 1957; Lindsley and Fuhrman, 1988) (Figure 55). Pyroxenes in both gabbronorites and gabbros plot on the magnesic side of the ternary, meaning the melt was depleted in Fe relative to Mg when they formed (Kretz, 1963).

In *gabbros* of type *a*, augite was intergrown with alkali feldspar. Augite occurred as rounded grains and euhedral laths (Figure 51). The rounded grains superimposed euhedral augite grains and feldspar. Texturally, it can be inferred that the rounded grains grew later (Bowen, 1912). Furthermore, they were more magnesic than the lath grains, denoting that the melt composition had changed (Kretz, 1963). The composition of the rounded grains matched that of the rim pyroxene, which implies they grew under same conditions and therefore the same time (Bowen, 1912). The composition of augites infers a crystallization temperature range of 1225-1025˚C ± 50˚C (Lindsley and Andersen, 1983). The alkali feldspar had both normal zoning and lamellar intergrowths, implying a slow cooling rate (Yoder *et al.,* 1957). Their

composition yielded a temperature range of 1125-1020˚C ± 50˚C. However, the sampling points were clustered, making it possible there was a larger range. The composition of feldspar differed from that of the surrounding matrix groundmass, which contained plagioclase, meaning the clast originated from a different melt. A corona of finer grained intergrowth of feldspar and pyroxene along the clast boundary implies recrystallization due to contact metamorphism occurred (Shaw, 1965).

Gabbro b described clasts in which randomly arranged euhedral lath grains of plagioclase (100 µm to 200 µm long) were interspersed among anhedral augite (Figure 52). Gabbro b had similar zoning patterns to lath grained gabbronorite c and other gabbro types, however the difference in pyroxene composition suggests a different origin. Compositions yielded a crystallization temperature range of 1025-800˚C ± 50˚C for augite and 1245-1205˚C ± 25˚C for plagioclase (Bowen, 1928; Lindsley and Andersen, 1983; Lindsley and Fuhrman, 1988). The shape of the plagioclase implies they cooled at a faster rate than the other gabbros (Lofgren, 1974).

Clasts of equigranular, microcrystalline texture with intergrowths of augite and albite (andesine, oligoclase) were defined as *Gabbro c* (Figure 53). These showed compositional variation in augite grains, but no directional trend, however for plagioclase there was zoning from core to rim (Ca to Na). This suggests the source melt underwent slow cooling. Compositions yielded a crystallization temperature range of 1050-650˚C ± 50˚C for augite and 1190-1150˚C ± 25˚C for plagioclase (Bowen, 1928; Lindsley and Andersen, 1983; Lindsley and Fuhrman, 1988). Both a clast from the matrix and one from an impact melt clast were probed. Their plagioclase composition overlapped, but the pyroxene from the matrix sample was higher in Fe, suggesting that the source melt was higher in Fe also (Kretz, 1982). Average grainsize was larger for the matrix clast, implying a slower crystallisation rate (Shaw, 1965). Plagioclase grains were larger than augite grain, implying that these grew at a faster rate (Shaw, 1965). This is in line with the temperature ranges inferred by the cooling models. The matrix clast was angular, and only had core to rim zoning in the plagioclase. There were no signs of the matrix being plastically deformed or signs of contact metamorphism along clast boundary making it likely that it nucleated in the matrix and could therefore be used to determine original composition of the matrix melt (Krumbein, 1941). However, the clast of this type that was sampled from the impact melt was contained in a felty plagioclase-pyroxene groundmass and had poorly defined clast boundaries and with pyroxene recrystallised in some spots, indicating that it underwent thermal metamorphism when coming in contact with a shock induced quenched melt (Stöffler *et al.*, 1986).

Type *Gabbro d* was characterised by its high plagioclase (>80%) and low pyroxene (<20%) composition (Figure 54). Compositionally it came close to being anorthosite (defined by >90% plagioclase, Streckeisen, 1974). The representative sample was made up of a ~ 600 µm x 800 µm, singular, euhedral andesine grain, with growth of augite along one corner and in the core. Its angular shape strongly implies that it grew from the surrounding melt (Krumbein, 1941), and its relatively large grain size means it grew at a slow rate (Shaw, 1965). The matrix surrounding it is plastically deformed, implying it was in a plastic state and therefore displaced whilst the plagioclase grain grew (Caristan, 1982). The plagioclase grain was zoned from core to rim (Ca to Na), indicative of slow cooling (Lindsley and Fuhrman, 1988). The augite was strongly zoned (Ca – Mg), through no core to rim compositional pattern could be identified, which speaks against it being a result of contact metamorphism (Miyamoto *et al.,* 1985). The augite grew in a convex shape and was less fractured than the plagioclase, implying that its growth superseded the plagioclase's, possibly replacing it (Bowen, 1912). Compositions yielded a crystallization temperature range of 850-650˚C ± 50˚C for augite and 1220-1200˚C ± 25˚C for plagioclase (Bowen, 1928; Lindsley and Andersen, 1983; Lindsley and Fuhrman, 1988). Temperature ranges support a formation history in which augite crystallized after the plagioclase.

4.1.4 Peridotites

Multiple peridotites were identified in Qemscan images, however only one could successfully be microprobed as the rest yielded bad totals. Peridotite is rarely stable at the surface, as olivine gets converted into pyroxene when pressure and temperature decreases, or it comes in contact with water (Bowen, 1922). The presence of olivine denotes an early stage of crystallisation of the melt (Poldervaart and Hess, 1951). However, if pyroxene underwent contact metamorphism with high temperatures or pressures, it may no longer be stable in the pyroxene field and gets converted into olivine, the next stable phase of same chemical composition but with different molar arrangement (Bowen, 1922). Using Qemscan (Figure 69), olivine was typically identified along edges and cracks of pyroxene phenocrysts, indicative of contact metamorphism, or in the clast core, indicative of melt cooling or possible surface exposure with subsequent weathering. However, angular shape makes the latter unlikely (Krumbein, 1941).

The lack of microprobe data made it not possible to make general assumptions about the phase composition of olivines in NWA 7034. The successfully sampled clast had pyroxene high in Mg (77 ± 1 %) with some Fe (21 ± 1 %), making it an enstatite (Figure 56). Ca composition was low (<2 ± 1 %), indicating it formed at low temperature, 800˚C ± 100˚C (Lindsley and Andersen, 1983). Assuming a closed system, one can presume that the olivine grew from an Mg rich melt and was therefore a forsterite (Bowen, 1922). Zoning in the enstatite was minimal (<5%) and occurred in the Mg-Fe range. The highest Fe content was in the reaction zone on the clast boundary to the matrix. All other sampling points overlapped in composition, suggesting that Mg was being replaced by Fe at the reaction zone, implying a changing melt composition (Kretz, 1982).

BSE images of multiple peridotite clasts revealed them to be heavily fractured, with melt intruding into some of the fractures, indicating it experienced high pressure, but not enough to cause ductile deformation or phase replacement. Brittle deformation suggests high pressure at low to medium temperature, which would be consistent with an impact (Caristan, 1982). The fractures did not crosscut the groundmass. In combination with intruding melt this makes impossible that the brittle deformation originated from the most recent impact event, meaning the clast experienced at least one previous impact. Some peridotites were partially consumed by the melt along edges (Figure 56, see thin dotted line). This melt was classified as Mg-phyllosilicate by Qemscan but may be a fine grained intergrowth of fine grained pyroxene and plagioclase, which could not be accurately classified due to grainsize being smaller than the Qemscan's resolution (1 µm). One plausible explanation could be that a previous impact caused the groundmass to partially melt but did not induce enough heat to resorb the pyroxene, only fracturing it. The melt intruded into cracks and along clast boundaries where it induced a phase change to olivine, and rapidly cooled producing the quench texture in the groundmass (McSween *et al.,* 2015). This fits with the pattern of olivine in the Qemscan images, where olivine was detected along cracks and clast boundary (Figure 69).

Alternatively, many peridotites contained Fe-rich phases which were smaller than 1 µm, making it possible that areas of overlap may have been misidentified as olivine by the Qemscan. This explanation fits with the electron microscope data, where no olivine was detected in the peridotites sampled.

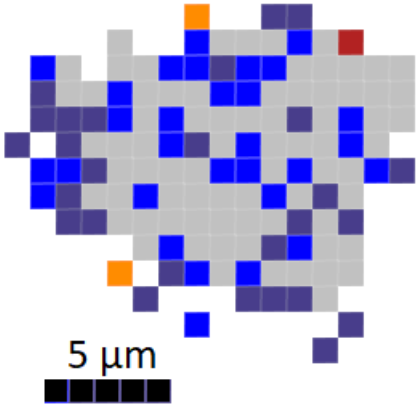

Figure 69: Peridotite clast classified by Qemscan (grey = olivine, purple = enstatite, blue = Mg-phyllosilicate, orange = Fe-oxide/hydroxide, red = Fe-Ti oxide).

4.1.5 Spherules

Quenched clasts were primarily found in impact melt clasts. Likely they were ejected allowing them to rapidly cool in the air, then landed in molten area of impact basin impact, and were later assimilated into an earlier generation of breccia (Bowen, 1912). This suggests that the melt the quenches were formed from originated from a different location, closer to the epicentre of the impact, than the melt they were enclosed in, which was likely near the surface, allowing the ejecta to deposit (Grieve *et al.,* 1977). The absence of impact spherules in the latest generation matrix implies that the most recently formed melt originated from an area where no quenched spherules were deposited: possibly buried or further away from the epicentre (Grieve *et al.,* 1977).

The *enstatite spherule* was compositionally similar to the other pyroxene phenocrysts in impact melt clasts (Figure 57). It was distinguished by its quenched texture with skeletal growths of iron oxides, which implies it experienced rapid cooling (Bowen, 1912; Hays, 1976). It was heavily fractured. As these fractures crosscut the iron oxide growth, this brittle deformation must have occurred afterwards (Steno, 1669). Likely resultant of shockwave propagation (Stöffler *et al.*, 1986). Ca content was higher in the core than the rim, characteristic of cooling. According to the pyroxene cooling model, it crystallized at 1125-1100˚C ± 100˚C (Lindsley and Andersen, 1983). Like other impact melt enstatites, it was high in Mg (77 ± 1%), meaning it grew from a Mg rich melt (Kretz, 1982). This supports the idea that the previous generation impact melt was enriched in Mg, relative to the matrix.

Augite spherules were represented by one sample (Figure 58). Unfortunately, there were not enough sampling points to determine zoning patterns in augite as bad totals allowed only two to be used for analysis (Figure 59). Composition of augite implies a crystallization temperature of 1175˚C ± 50˚C (Lindsley and Andersen, 1983). Grain size was cryptocrystalline (<~5 µm) for pyroxene and iron oxides, with tabular, skeletal plagioclase grains up to ~200 µm long, implying rapid growth (Lofgren, 1974). The plagioclase grains were relatively small, meaning it continued to cool rapidly (Lofgren, 1974). Pyroxene (augite) had disorderly glassy texture, denoting rapid cooling, after a possibly shock induced melting (Stöffler *et al.*, 1986). It was contained within a halo of lath grained plagioclase (albite – andesine) that grew perpendicular to clast boundary. The halo of plagioclase along the clast boundary may be due to cooling behaviour (Bowen, 1912). If clast recrystallised from the melt and grew centre outwards, the melt might have cooled to the point where plagioclase was stable over pyroxene (Bowen, 1922). Temperatures obtained via cooling models suggest the augite crystallised at 1175˚C ± 50˚C, and the plagioclase at 1210-1190˚C ± 25˚C. Their temperatures suggest simultaneous formation, however the models have been shown to not be

entirely precise and accurate (Bowen, 1928; Poldervaart and Hess, 1951; Lindsley and Andersen, 1983; Lindsley and Fuhrman, 1988). Also, the only valid sampling points in the pyroxene were taken near the plagioclase. Probing the rim could have yielded different temperatures, as the pyroxene was visibly zoned. Plagioclase lath grains were also found at the centre of the clast, where they appeared to be stacked in the same direction as the iron oxide veins. This is indicative of compression, possibly resulting in formation of iron oxides which recorded a directional component. This has been recorded in other meteorites and likely denotes an impact induced shock structure (Stöffler *et al.*, 1986; Ma *et al.*, 2016). The clast underwent multiple stages of deformation. The matrix around it appeared to be elastically deformed. Fractures crosscut these, implying pyroxene and plagioclase growth was followed by physical deformation (Steno, 1669; Bowen, 1912). These Fe-oxide veins were overprinted by a second set of fractures, likely from a second impact. These veins were not filled in, meaning these formed while the clast was in a brittle state and was not pressurized or heated enough to initiate recrystallisation (Caristan, 1982; Stöffler *et al.*, 1986). It is evident that the clast underwent at least two high pressure deformation events (possibly impacts) after its formation. This theory is further supported by the fact that the clast was found within an impact melt clast.

Only one example of a *lath grained spherule* was identified throughout all mounts (Figure 60). No similar clast has been described throughout NWA 7034 by other authors, making it extremely rare. It was a spherule of melt located within a larger impact melt clast, of distinctly different groundmass appearance. The unusual zoning pattern (replacement of Mg by Fe from core to rim of clast, the opposite of pyroxene phenocrysts in impact melt clasts) supports this assumption that it originated from a melt of a different composition (Kretz, 1982). The pyroxene component in the groundmass was augite, denoting a high temperature formation (Lindsley and Andersen, 1983). The groundmass had a wavy, quench texture that was equigranular and aphanitic (with grains large enough to be identified in microscope images), indicating a fast cooling rate (Lofgren, 1974). Groundmass was displaced by larger, rounded Fe-oxide phases, in the shape of a cat-eye, suggesting it crystallised first (Bowen, 1912). Enstatite lath grains were stacked roughly parallel to each other, indicating directional orientation, such as due to flow in igneous extrusive basalts. Its texture and mineral makeup resembled that of picritic lunar basalt (Hays, 1976). Based on the assumption that each impact melt clast found within another impact melt is of an older generation, this origin would mean that the clast would be minimum two generations older than the clasts found in the matrix. Alternatively, they could have originated as melt condensate droplets. They resemble barred spherules of this origin, as described by Belza *et al.*, (2017). The groundmass between the enstatite grains was composed of augite and plagioclase with scattered iron oxides. As augite is the higher temperature phase, it is likely to have crystallized first, followed by rapidly grown enstatite lath grains once the melt cooled to 1050-800˚C ± ˚100C (Lindsley and Andersen, 1983), and iron oxides at ≤1030˚C (Wright and Okamura, 1977). The cores of the lath grains had a higher Mg/Fe ratio, which compliments the theory that the source magma was depleted in Mg, relative to the source magma of the impact melt which encapsulated the spherule (Kretz, 1982). Lath grains had an oxide phase at their core, likely a spinel, which would be in line with the melt being depleted in Mg, therefore leading to the zoning pattern seen (Kretz, 1982). This is in line with what was observed in the barred spherules described by Belza *et al.*, (2017). The low plagioclase content and absence plagioclase lath grains denotes an ultramafic composition for the source melt. Augite and plagioclase compositions suggest a temperature range of 1225-1200˚C ± 50˚C (Lindsley and Andersen, 1983) and 1260-1205˚C ± 25˚C (Bowen, 1928; Lindsley and Fuhrman, 1988), respectively; indicating that the two phases grew congenitally. The high temperature plagioclase component was found adjacent to the lath grains and the low temperature component near the clast boundary, from which it can be inferred that the spherule cooled from core to rim. The plagioclase composition does not support heat induced metamorphism at the contact between the spherule and

impact melt clast. This further supports an origin as described by Belza *et al.*, (2017). Therefore, the spherule and impact melt clast it is contained in formed in the same event but originated from different source melt, making it only one generation older than the matrix. Fractures denote a high-pressure deformation event, while the clast was brittle (Caristan, 1982). This may represent a subsequent impact (Stöffler *et al.*, 1986).

Diopside-plagioclase-enstatite spherules were made up of a diopside core contained in a plagioclase mantle and enstatite rim (Figure 63, Figure 64). Ca-rich pyroxene (diopside) occurred as lath grains, in some cases radially, or with cleavages intersecting at an ~120-125˚ angle. The cleavage indicated that this might be a hornblende rather than a pyroxene (Streckeisen, 1974). The molar quantities of Si, O, Fe, Ca, Mg and Al recorded for this sample made it possible for it to be hornblende, however, yielded better totals for pyroxene (Pasero, 2018). The lath shaped crystals indicate rapid growth and fast cooling rate (Lofgren, 1974). The temperatures obtained from composition indicate that crystallization of plagioclase preceded that of the pyroxene. Temperature ranges were: 1190-1150˚C ± 25˚C for plagioclase (Bowen, 1928; Lindsley and Fuhrman, 1988), 800 ± 100˚C for enstatite, and ≤500 ± 50˚ for diopside (Lindsley and Andersen, 1983). This cooling history was supported by the textural observations. There was brittle deformation of the plagioclase in the growth direction of the lath grains, indicating that their growth superseded the plagioclase while in a crystalline state (Bowen, 1912; Caristan, 1982). At other contacts with the plagioclase the diopside grew in a concave pattern, indicative of a more gradual replacement of plagioclase by diopside. The pockets of remaining plagioclase may be due to the plagioclase being zoned, and one component being more stable. Enstatite was zoned and occurred sectionally and along the rim of the clast, indicative of high heat induced contact metamorphism. The enstatite was less fractured than the plagioclase, supporting the theory that its formation superseded the plagioclase. Plagioclase was heavily fractured, indicative of heavy brittle deformation. Some fractures crosscut both enstatite and plagioclase, meaning the clast underwent two separate events in which it was deformed after having fully cooled. Possibly two separate impact events (Stöffler *et al.*, 1986). Having two pyroxene groups of such radically different compositions in one clast is significant and indicates that the clast formed in two stages with two separate heating-cooling events (Lindsley and Andersen, 1983). Diopside core likely originated from original source melt while the composition of the enstatite rim reflects composition of the melt it came in contact with (Miyamoto, Duke and McKay, 1985). This supports the theory that the first generation impact melt was enriched in Mg. The clast may be a remnant of a gabbronorite clast that underwent compositional alteration due to heating that was not extensive enough to recrystallise the clast entirely. It was heavily fractured compared to gabbronorite clasts found in the matrix, indicative of having been located in a zone that experiencing higher pressure during a previous impact (Stöffler, 1966; Stöffler *et al.*, 1986).

The *enstatite-plagioclase spherule* was characterised by a plagioclase core with a rim of plagioclase (andesine) and enstatite lath grains (Figure 66). The lath grains were oriented primarily in a radially outward direction, indicative of rapid cooling (quenching), possibly by becoming airborne (Lofgren, 1974). Its shape was not perfectly rounded, this may be due to it not having finished crystallising when coming in contact with the impact melt. This is further supported by a change in growth texture from one side to the other, going from equigranular to lath, meaning the crystallisation rate must have changed (Lofgren, 1974). Plagioclase composition yields a temperature range of 1195-1215˚C ± 25˚C, consistent with rapid cooling (Bowen, 1928; Lindsley and Fuhrman, 1988).

4.1.6 Vein

A gabbronorite clast (Figure 41) was crosscut by a vein filled with an unknown mineral. This vein crosscut the clast and impact melt it was contained in, but not the matrix, meaning it post-dates clast and impact

melt formation, but not matrix formation. The enstatite was compositionally zoned Mg to Fe and very low in Ca (<5%) apart from one point sampled by the vein, which had a composition is much higher in Ca (54%), making it a diopside (Figure 41). The difference in composition implies that the intrusion of the vein caused chemical alteration and contact metamorphism in the surrounding material. The origin of the vein is unknown, but it supports the theory that NWA 7034 contains clasts from hydrothermal or porphyry areas (McCubbin *et al.,* 2016). Alternatively it could be the result of quenched melt intruding into a fracture, both of which were caused by a high-pressure shockwave (Stöffler *et al.*, 1986).

4.2 QUANTIFYING IMPACT EVENTS

The brecciated structure eliminates the possibility that it was an igneous rock ejected from Mars by a volcanic eruption, making the most likely culprit an impact (Norton, 1917). The presence of cogenetic (by principle of cross cutting) impact melt particles in a glassy or crystallised state contained within a matrix, and shock textures such as planar deformation features in feldspars and pyroxenes (such as lamellae and twinning) and contact metamorphism along clast rims, makes it likely that this area had previously been located in the suevite formation zone of a previous impact (where unmolten regolith clasts were sintered with molten regolith), analogous to Ries crater in Germany (Engelhardt *et al.,* 1995). Assuming similar conditions, the impact pressure of the matrix forming event would have been ~800,000 atm and induced a temperature of ~750 ˚C (Engelhardt *et al.,* 1995). Estimated crystallization temperatures for the feldspar and pyroxenes components observed in the matrix were significantly higher, however, these conditions cannot be set with reliable accuracy, since atmospheric pressure on Mars is far lower (averaging 0.7 atm (Kaplan *et al.,* 1964). Also, unlike the predominately felsic site in Germany, data obtained from remote sensing and meteorites indicate that the makeup of the Martian crust is principally mafic to ultramafic (McSween, 2015).

BSE images showed cracks passing through NWA 7034, crosscutting multiple minerals and clast types. These were consistently present throughout all mounts and had similar appearance (lacking mineral replacement or melt intrusion), making them likely to be caused by a singular event, most likely the ejection event or impact on Earth (French, 1998). These cracks lack melt intrusion or recrystallisation, implying that the temperature and pressure upon impact was not high enough to cause ductile deformation, resulting in brittle deformation instead (Caristan, 1982). This implies that any cracks containing melt intrusions and recrystallisation were caused by different high pressure events, likely other impacts. These observations support the identification of NWA 7034 as a polymict breccia, which had been suggested by Santos *et al.,* (2015). Some of these filled in cracks crosscut melt clasts and the igneous clasts contained in these. For this to occur, the groundmass had to have been solid, meaning the impact event following the emplacement of the vein that did not cause complete melting, but formed cracks that were filled by superheated quenched melt (Stöffler *et al.*, 1986). Alternatively, the already veined impact melt clasts were emplaced in the cooler matrix melt as xenocrysts. Both origins mean that the fracture event predates the matrix formation (Steno, 1669; Bowen, 1912). Porphyritic groundmass indicates cooling at a decreasing, rather than a discontinuously increasing rate (Bowen, 1912; Hays, 1976). This means the parent body that NWA 7034 was sourced from had enough time to cool down and crystallise following the matrix-forming impact event. This implies that the brecciation event occurred during a period of low impact density in Mars' history. This may be reflected by the Xe isotope ratios observed by Cartwright *et al.*, (2014), denoting a long period of non-disturbance. Mahajan (2015) suggested that NWA 7034 was ejected at ~7.3 Ma. At that time, impact basins were geographically widespread, as Mars experienced multiple periods of bombardment, but impact frequency itself was reduced (Anders and Arnold, 1965; Wetherill, 1975). Despite frequency of impacts decreasing throughout the Amazonian period (Tanaka,

1986; Barlow, 1988), weathering in the Post-Hesperian period, when the Martian climate changed from wet to dry (Baker, 2001; Jakovsky and Philips, 2001), occurred at an extremely slow rate due to absence of water (Chevrier and Mathé, 2007), allowing for these types of regions to be preserved.

After the parent body had cooled to a solid state, another impact event occurred. This time around, the source region of NWA 7034 was located in the brittle, projectile zone of the impact crater (Grieve *et al.,* 1977). Small clasts, including NWA 7034 were catapulted into the atmosphere at high enough velocity to override Mars escape velocity, allowing them to be ejected from Mars (Agee *et al.,* 2013).

Stöffler (1966) defined impact zone facies according to shock alteration textures found in minerals. The innermost zone, closest to the epicentre of the impact, is described to be made up of recrystallized rocks (facies 4). These are remnants of sediments or bedrock that was melted completely during impact. The next zone out was partially melted by the impact. It is defined by the presence of quenched plagioclase glass (facies 3). The following zone experienced brittle deformation due to shock wave propagation. Here impact induced twinning or lamellae can be observed in plagioclase (facies 2). The outermost zone is defined by shocked quartz and plagioclase (facies 1). The absence of shocked quartz, typically found throughout impact craters (Wackerle, 1962), can be explained by a lack of felsic minerals in the parent body based on the mafic nature of the mineral composition (Santos, Agee, McCubbin, Shearer and Burger, 2013). Due to the low abundance of quartz, facies categorisations were made based on textural evidence in plagioclase and pyroxene. It was assumed that pyroxene behaved the same way as plagioclase.

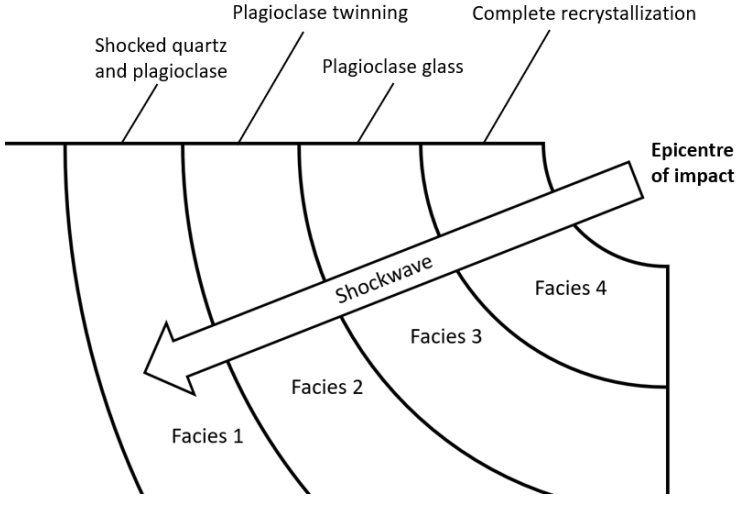

Figure 70: Graphical representation of impact facies and their signature alteration features as described by Stöffler, 1966.

Info Box 3: Impact zone facies as defined by Stöffler, 1966.

Impact facies based on textures and shock structures, as defined by Stöffler (1966), were used to pinpoint the location of various clasts contained in NWA 7034, relative to the impact zone (Info Box 3). According to textures observed in NWA 7034, clasts sourced from all four zones were contained in NWA 7034, providing further support to the theory that it experienced multiple impact events. Preservation of polymict breccia texture show that NWA 7034 did not experience high enough temperatures to partially melt when it was ejected. Furthermore, lamellar intergrowths, differing from the optical orientation of their host crystal, were seen in some pyroxenes and feldspars, as well as twinning. These were similar to

shock structures in feldspars in zones 1 and 2. These were randomly oriented and not seen in all pyroxene and feldspar phenocrysts throughout NWA 7034. Therefore, it is unlikely they originated from the latest impact (on Earth). This would make the likely location of the source rock during ejection from Mars facies 1 or even further away from the impact epicentre. Additionally, quenched plagioclase glass was identified, in cracks of a matrix plagioclase. This denotes facies 4. The shocked plagioclase component matches the texture and composition of sodic maskelynite, which forms at a pressure ≥300,000 atm (Chen and El Goresy, 1997). These alteration textures indicate that the source rock of NWA 7034 experienced multiple shock metamorphism events after the latest brecciation event, at different pressures and distances away from impact epicentres. These could be the cause of resetting events at about 1.7 Ga, 1.6 Ga, 1.35-1.5 Ga, and 170 Ma, as described by (Humayun *et al.*, 2013; Nyquist *et al.*, 2013; Cartwright *et al.*, 2014).

The brecciated texture, and quenched pyroxene and plagioclase glass in the matrix, the source rock of NWA 7034 was located in the partly molten zone, facies 2, during the matrix forming impact. Previous generation impact melt clasts were also brecciated and contained pyroxene glass, microcrystalline gabbroic clasts, and quenched plagioclase and pyroxene spherules, indicating that at they were sourced from a zone even closer to the epicentre, likely inner facies 3 or even facies 4 (Stöffler, 1966).

4.3 Source rock origin on Mars

This section describes where on Mars the clasts making up NWA 7034 might have originated from, and what these new findings say about the rock forming conditions on the surface of Mars. Petrology (impact melt basalts, including alkali basalts) and mineralogy (ortho- and clinopyroxene, plagioclase, alkali feldspars) match those of Gale (5.4°S 137.8°E) and Gusev (14.5°S 175.4°E) crater (Figure 71). As do estimated temperature and pressure range of polymineralic clasts in NWA 7034 (Figure 72) (Filiberto, 2017).

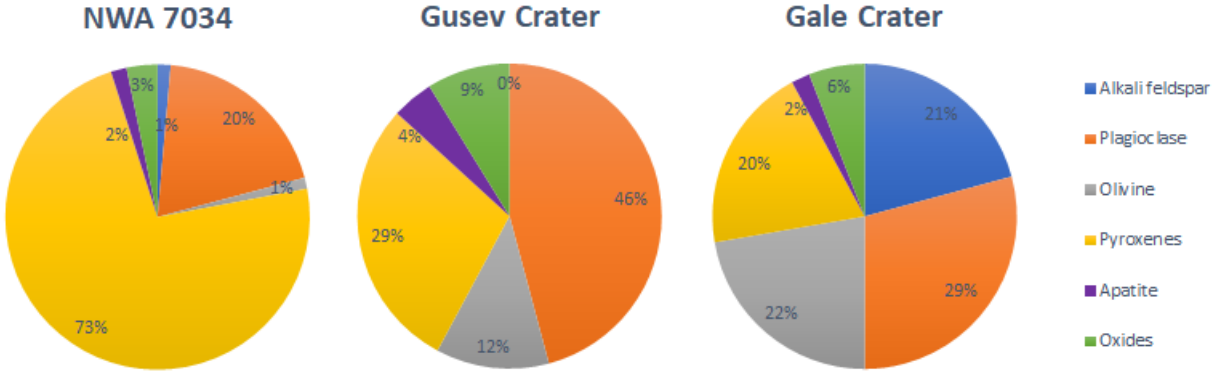

Figure 71: Normalised mineral composition of mounts sampled from NWA 7034 and igneous rocks from Gale crater (Stolper et al., 2013; Schmidt et al., 2014). Modal mineral composition of igneous rocks from Gusev crater (McSween et al., 2008). Adapted from (McSween, 2015).

Therefore, I propose that clasts from both Gale and Gusev crater were sourced and accumulated into NWA 7034. In this scenario, the ejection spot is located where the projectile range of the two craters overlap, likely within Elysium Planitia. This area experienced hydrothermal events, a possible origin for the veins found within impact melt clasts in NWA 7034, and further hydrothermal evidence observed by (McCubbin *et al.,* 2016). The largest zircon found had a rounded edge (Figure 11), indicative of weathering and subsequent transport, possibly by fluid infiltration, as seen with zircons at Jack Hills, Australia (Trail, Mojzsis and Harrison, 2004).

Thermal Emission Spectrometry identified alkali feldspars to be distributed in correlation with high albedo regions on Mars, which fall within the proposed ejection area (Bandfield, 2002). Within this area, Martian rovers have identified alkali basalts, such as the ones found in NWA 7034, in the Columbia Hills in Gusev crater (McSween *et al.,* 2006). A zircon grain contained within an alkali basalt in NWA 7034 had been dated to be 4.72 ± 0.23 Ga (McCubbin *et al.,* 2016). Mudstone bedrock in Gale crater was dated at 4.21 ± 0.35 (Farley *et al.,* 2014) and layering of strata has been inferred to have occurred 3.6–3.8 Ga, placing crater formation near the Late Noachian–Early Hesperian boundary (Thomson *et al.,* 2011). Flood basalts in Gusev crater were inferred to have formed ~3.65 Ga (Greeley *et al.,* 2005). However, the basalts assessed were not alkaline. Absolute age of Columbia Hills alkaline rocks has yet to be determined and likely predates the generation of the crater and impact melt basalts at ~4.1-3.9 Ga (Werner, 2008), as the ridge is believed to have formed from impact induced uplift (Mccoy *et al.,* 2008). So far, alkali volcanism on Mars has been correlated with ancient ages, which can be explained by alkalis being incompatible elements and therefore depleted early on in the partial melting of the mantle, making the alkali basalts remnants of early Martian crust (McCubbin *et al.,* 2016). In line with this reasoning, either the impact that formed Gusev crater, or alternatively one of the smaller ones that occurred after Columbia Hills alkaline basalts were already exposed, likely propelled the alkaline rocks into the ejecta zone in which NWA 7034 was accreted, allowing for NWA 7034 to contain these ancient clasts. The presence of the layered norite-pyroxenite alkali basalt makes it likely that alkali clasts, sourced from two separate regions at minimum two separate events, found their way into NWA 7034. Likely the first impact ejected the impact melt clast containing the alkali felspars and the latest event let to the accretion of these clasts together with the alkaline basalt clast, in the matrix. The timeline of crater stratification of Gusev crater restricts the occurrence of the first brecciation event to after ~3.65 Ga, which is in line the brecciation date of ~2.1 Ga, proposed by (Nyquist *et al.*, 2013).

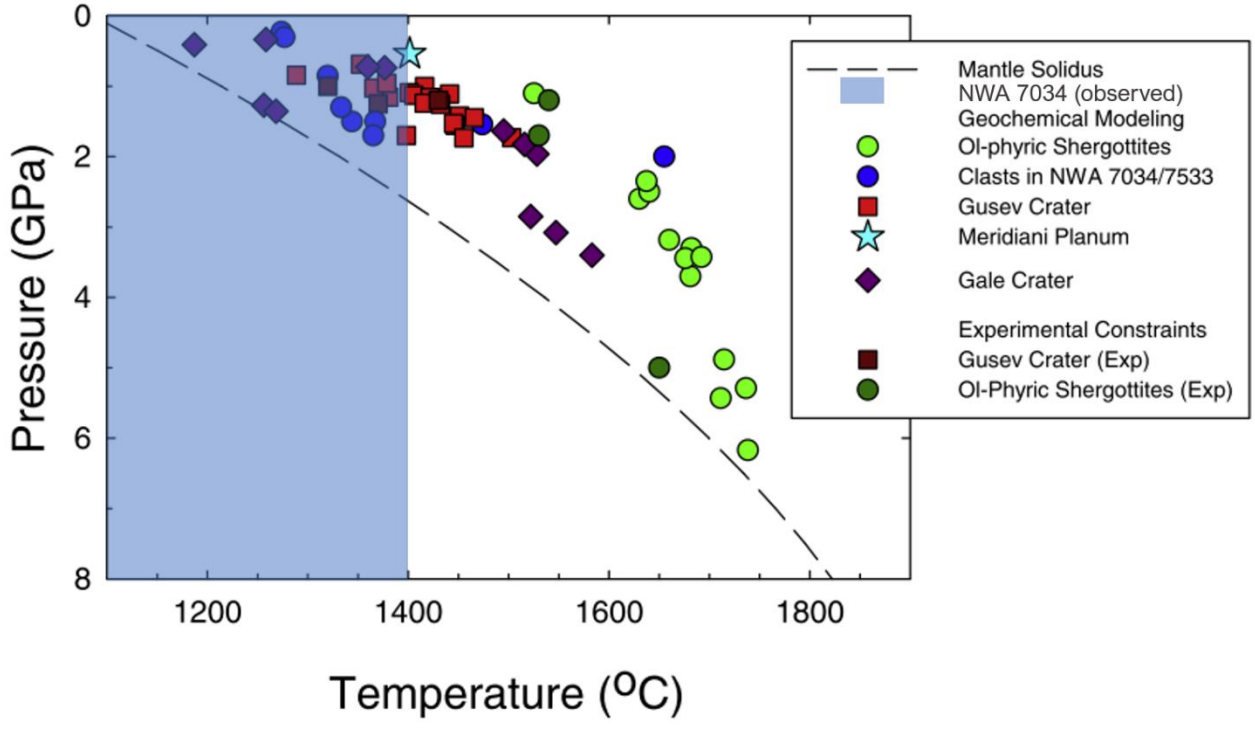

Figure 72: Temperatures and pressures calculated for Martian compositions, taken from Filiberto (2017). Adapted from (Filiberto and Dasgupta, 2011, 2015). Experimental constraints for basalts from Gusev Crater (dark red squares) and Martian meteorites (dark green circles). Solidus of nominally volatile-free Martian mantle (dashed line, Kiefer et al., 2015).

4.4 COMPARISON TO OTHER STUDIES

Petrographic interpretations support those by Santos *et al.*, (2015), Wittmann *et al.*, (2015), McCubbin *et al.,* (2016) and Nyquist *et al.,* (2016). Wittmann *et al.*, 2015 proposed Gatteri crater as a launch site based on matching Th and K proportions to the surface rock, and a crater formation age of ~5 Ma which is in line with 2 of the 3 cosmic radiation exposure ages calculated for NWA 7034 by Cartwright *et al.*, (2014). Gratteri crater is close enough to encompass an abundance of ejecta from the Gale and Gusev crater region proposed by this study, and is a match in terms of petrology, mineralogy, geochronology and geochemistry. Additionally, the results of these combined studies independently of each other support a source region along the Northern edge of the Southern Highlands (Wittmann *et al.*, 2015), making this region a likely candidate, even if the source crater itself cannot be determined with certainty.

The clast formation temperatures determined in this study were overall lower than those proposed by Filiberto (2017), however this can be explained as the highest possible temperature phases such as olivine were only sparingly sampled and yielded unreliable results (Bowen, 1912). Another factor is the use of a different pressure model. Filiberto (2017) used a PMELTS model. However, I did not deem the model reliable for this sample. The reason for this was NWA 7034 being a porphyry clast and there being too many unknown variables to consider. There was insufficient data available to determine many factors that influence crustal pressure such as: crustal age, temporal and geographic proximity to other impacts, impact density, burial depth, atmospheric thickness etc., for each clast at the time of formation (Abramov and Mojzsis, 2016). Therefore, I decided to use a 1 atm standard so that the temperatures could be more easily converted if used in further studies. Additional research into the pressures at clast formation could be beneficial, especially in combination with isotope ages, in order to place constrictions on the pressure history of the Martian crust.

5 CONCLUSION

NWA 7034 subsamples were primarily composed of clinopyroxene (45%), orthopyroxene (15%), Mg-phyllosilicates (17%), plagioclase (17%), alkali feldspar (1%), oxides (3%), apatite (1%), and olivine (1%). Major clasts include gabbroids (gabbronorite and gabbro), feldspar phenocrysts, pyroxene phenocrysts, apatite-plagioclase(-ilmenite) clasts, and impact melt clasts.

Pyroxenes were magnesic and occurred both as ortho- and clinopyroxene, indicating different cooling rates and therefore multiple heating events. Formation temperatures of 1210-<500˚C ± 50˚C in older generation clasts, and 1225-600˚C ± 50˚C in the youngest generation clasts were inferred from their composition. Both alkali and plagioclase feldspars were found. The plagioclase was sodic, denoting a formation temperature of 1260-1150˚C ± 25˚C in older generation clasts, and 1245-1150˚C ± 25˚C in the youngest generation clasts. Alkali feldspar occurred as perthite, implying a formation temperature of ≤1000˚C ± 50˚C, and pressure <0.5 GPa, or as part of gabbroic rock where its composition suggests a crystallization temperature of ≤1070˚C ± 50˚C.

Porphyritic texture denotes a continuously decreasing cooling rate, meaning that the source rock experienced a period of non-disturbance following its breccia accretion. This might reflect the Xe isotope ratios noted by Cartwright *et al.*, (2014). Lithic and matrix textures resemble that of suevite found in Ries crater on Earth. This implies a similar origin where in suevite unmolten regolith clasts were sintered with molten regolith (Engelhardt *et al.,* 1995). Assuming similar formation conditions, the impact pressure of the matrix forming event would have been ~800,000 atm.

The degree of shock was estimated based on shock textures and used to estimate the distance from the impact epicentre for the different generations of clasts, according to impact shock zones defined by Stöffler (1966). It was deduced that the source rock was located in the partly molten zone during the matrix forming impact (facies 3), and in the completely molten and recrystallized zone (facies 4) during at least one of the previous brecciation events (impact melt forming event). Unmolten xenocrysts with contact metamorphism along clast boundaries, with pyroxene and plagioclase compositions differing to that of matrix phenocrysts were deduced to be sourced from different regions.

Shock textures, such as brecciation, twinning in pyroxene, fractures, quenched pyroxene and plagioclase (maskelynite) glass, partial melting and resorption, were observed at different degrees throughout different sections, some only present in some impact melt clasts, others in the matrix. These reflect multiple impact shock metamorphism events, at different pressures, temperatures and distances from impact epicentre. A sodic maskelynite was found in a matrix plagioclase, indicating that the accreted breccia experienced shock metamorphism at a pressure ≥300,000 atm after its formation ~2.1 Ga (Chen and El Goresy, 1997; Agee *et al.*, 2013). The shock textures observed are likely remnants of metamorphic resetting events occurring at about 1.7 Ga, 1.6 Ga, 1.35-1.5 Ga, and 170 Ma, as described by (Humayun *et al.*, 2013; Nyquist *et al.*, 2013; Cartwright *et al.*, 2014).

Bulk rock composition and general mineralogical assemblage match mineral composition of Gusev crater, which has been suggested to be situated above an alkali volcanic source (Blake *et al.*, 2013; Stolper *et al.*, 2013). Furthermore, a cumulate clast was found in NWA 7034 whose composition matches a Noachian-age (~4.1 – ~3.7 Ga) layered intrusion that was exposed following the meteorite impact that formed Gusev crater during the Hesperian period (~3.7 – ~3.0 Ga) (Francis, 2011). Petrology and molar composition of plagioclase and pyroxene in the subsamples closely match the clasts at Gale crater (Blake *et al.*, 2013;

Filiberto, 2017). It is likely that rocks sourced from both these regions ended up in NWA 7034, and that its ejection location was in the zone that encompasses impact ejecta from both Gale and Gusev crater.

Overall, the petrologic evidence suggests that NWA 7034's formation and alteration history began with alkaline rocks formed in the Pre-Noachian (~>4.4 Ga), and were later molten by a high-pressure impact forming the first generation breccia. During Mars' period of heavy bombardment, it underwent multiple high-pressure shock metamorphism events, as indicated by filled in fractures not cross-cutting main matrix. This older breccia was partially molten and integrated into another breccia, forming the main matrix at ~2.1 Ga. This source rock was subjected to continuous shock metamorphism by other impacts, throughout the Amazonian. Finally, NWA 7034 was ejected from the brittle zone of an impact crater at ~7.3 Ma, ending up on Earth.

BIBLIOGRAPHY

Cover image: “Meteorite Impact Update” by John Doop. Taken from deviantart.net/johndoop.

Abramov, O. and Mojzsis, S. J. (2016) ‘Thermal effects of impact bombardments on Noachian Mars’, *Earth and Planetary Science Letters*. Elsevier B.V., 442, pp. 108–120. doi: 10.1016/j.epsl.2016.02.035.

Agee, C. B. *et al.* (2013) ‘Unique meteorite from early Amazonian Mars: water-rich basaltic breccia Northwest Africa 7034’, *Science*, 339(6121), pp. 780–5. doi: 10.1126/science.1228858.

Anders, E. and Arnold, J. R. (1965) ‘Age of Craters on Mars’, *Science*, 149(3691), pp. 1494–1496.

Ashworth, J. R. (1980) ‘Deformation mechanisms in mildly shocked chondritic diopside’, *Meteoritics*. John Wiley & Sons, Ltd (10.1111), 15(2), pp. 105–115. doi: 10.1111/j.1945-5100.1980.tb00514.x.

Baker, V. R. (2001) ‘Water and the Martian landscape’, *Nature*, 412(6843), p. 228.

Bandfield, J. L. (2002) ‘Global mineral distributions on Mars’, *Journal of Geophysical Research*, 107(E6), pp. 9–1.

Barlow, N. G. (1988) ‘Crater size-frequency distributions and a revised Martian relative chronology’, *Icarus*, 75(2), pp. 285–305.

Bayley, W. S. (1888) ‘Synopsis for Rosenbusch’s New Scheme for the Classification of Massive Rocks’, *The American Naturalist*, 22(255), pp. 207–217.

Bellucci, J. J. *et al.* (2016) ‘A Pb isotopic resolution to the Martian meteorite age paradox’, *Earth and Planetary Science Letters*, 433(September 2016), pp. 241–248. doi: 10.1016/j.epsl.2015.11.004.

Belza, J. *et al.* (2017) ‘Petrography and geochemistry of distal spherules from the KPg boundary in the Umbria Marche region (Italy) and their origin as fractional condensates and melts in the Chicxulub impact plume’, *Geochimica et Cosmochimica Acta*, 202, pp. 231–263. doi: 10.1016/j.gca.2016.12.018.

Blake, D. F. *et al.* (2013) ‘Curiosity at Gale Crater, Mars: Characterization and Analysis of the Rocknest Sand Shadow’, *Science*, 341(September), p. 1239505. doi: 10.1126/science.1239505.

Bohor, B. F. and Hughes, R. E. (1971) ‘Scanning electron microscopy of clays and clay minerals’, *Clays and Clay Minerals*, 19(1), pp. 49–54.

Boston, P. J. *et al.* (2003) ‘Human utilization of subsurface extraterrestrial environments.’, *Gravitational and space biology bulletin : publication of the American Society for Gravitational and Space Biology*, 16(2), pp. 121–31. doi: 10.1017/CBO9781107415324.004.

Bowen, N. L. (1912) ‘The order of crystallization in igneous rocks’, *The Journal of Geology*, 20(5), pp. 457–468.

Bowen, N. L. (1913) ‘Melting phenomena of the plagioclase feldspars’, *American Journal of Science*, S4 V35(210), pp. 577–599.

Bowen, N. L. (1922) ‘The reaction principle in petrogenesis’, *The Journal of Geology*, 30(3), pp. 177–198.

Bowen, N. L. (1928) *The evolution of the igneous rocks*. Princeton, NJ, Princeton University: Princeton, NJ, Princeton University.

Boynton, W. V. *et al.* (2007) ‘Concentration of H, Si, Cl, K, Fe, and Th in the low- and mid-latitude regions of Mars’, *Journal of Geophysical Research E: Planets*, 112(12), pp. 1–15. doi: 10.1029/2007JE002887.

Buddington, A. F. and Lindsley, D. H. (1964) ‘Iron-Titanium Oxide Minerals and Synthetic Equivalents’, *Journal of Petrology*, 5(2), pp. 310–357. doi: 10.1093/petrology/5.2.310.

Caristan, Y. (1982) ‘The transition from high temperature creep to fracture in Maryland diabase’, *Journal of Geophysical Research*, 87(B8), pp. 6781–6790.

Cartwright, J. A. *et al.* (2014) ‘Modern atmospheric signatures in 4.4 Ga Martian meteorite NWA 7034’, *Earth and Planetary Science Letters*. Elsevier B.V., 400(March), pp. 77–87. doi: 10.1016/j.epsl.2014.05.008.

Castaing, R. (1960) ‘Electron Probe Microanalysis’, *Advances in Electronics and Electron Physics*, 13, pp. 317–386. doi: 10.1016/s0065-2539(08)60212-7.

Chen, M. and El Goresy, A. (1997) ‘The nature of “maskelynite” in shocked meteorites: not diaplectic glass but a glass quenched from shock-induced dense melt at high pressures’, in *62nd Annual Meteoritical Society Meeting*, pp. 1–2.

Chevrier, V. and Mathé, P. E. (2007) ‘Mineralogy and evolution of the surface of Mars: A review’, *Planetary and Space Science*, 55(3), pp. 289–314. doi: 10.1016/j.pss.2006.05.039.

Dowty, E. (1976) ‘Crystal structure and crystal growth: II. Sector zoning in minerals ’, *American Mineralogist*, 61, p. 460.

Ehlmann, B. L. *et al.* (2011) ‘Subsurface water and clay mineral formation during the early history of Mars’, *Nature*. Nature Publishing Group,

479(7371), pp. 53–60. doi: 10.1038/nature10582.

Engelhardt, W. V. *et al.* (1995) 'Suevite breccia from the Ries crater, Germany: Origin, cooling history and devitrification of impact glasses', *Meteoritics*, 30(3), pp. 279–293.

Farley, K. A. *et al.* (2014) 'In Situ Radiometric and Exposure Age Dating of the Martian Surface', *Science*, 343(6169), pp. 1–5.

Filiberto, J. (2017) 'Geochemistry of Martian basalts with constraints on magma genesis', *Chemical Geology*. Elsevier, 466(June), pp. 1–14. doi: 10.1016/j.chemgeo.2017.06.009.

Filiberto, J. and Dasgupta, R. (2011) 'Fe2+-Mg partitioning between olivine and basaltic melts: applications to genesis of olivine-phyric shergottites and conditions of melting in the Martian interior', *Earth and Planetary Science Letters*, 304(3–4), pp. 527–537.

Filiberto, J. and Dasgupta, R. (2015) 'Constraints on the depth and thermal vigor of melting in the Martian mantle', *Journal of Geophysical Research: Planets*, 120(1).

Francis, D. (2011) 'Columbia Hills - An exhumed layered igneous intrusion on Mars?', *Earth and Planetary Science Letters*. doi: 10.1016/j.epsl.2011.08.003.

French, B. M. (1998) 'Impact Melts', *Traces of Catastrophe: A Handbook of Shock-Metamorphic Effects in Terrestrial Meteorite Impact Structures*, pp. 79–96.

Gellert, R. *et al.* (2006) 'Alpha Particle X-Ray Spectrometer (APXS): Results from Gusev crater and calibration report', *Journal of Geophysical Research E: Planets*, 111(2). doi: 10.1029/2005JE002555.

Goderis, S. *et al.* (2016) 'Ancient impactor components preserved and reworked in martian regolith breccia Northwest Africa 7034', *Geochimica et Cosmochimica Acta*. Elsevier Ltd, 191, pp. 203–215. doi: 10.1016/j.gca.2016.07.024.

Goldstein, J. I. *et al.* (1981) 'Specimen Preparation for SEM and X-Ray Microanalysis', in *Scanning Electron Microscopy and X-Ray Microanalysis*. Boston, MA: Springer.

Gottlieb, P. *et al.* (2000) 'Process Mineral Applications Microscopy for Process', *Microtextural Mineralogy*, (April), pp. 0–2. doi: 10.1007/s11837-000-0126-9.

Greeley, R. *et al.* (2005) 'Fluid lava flows in Gusev crater, Mars', *Journal of Geophysical Research*, 110(E5). doi: 10.1029/2005JE002401.

Greenwood, J. P. *et al.* (2008) 'Hydrogen isotope evidence for loss of water from Mars through time', *Geophysical Research Letters*, 35(5). doi: 10.1029/2007GL032721.

Grieve, R. A. F. ., Dence, M. R. . and Robertson, P. B. . (1977) 'Cratering processes - As interpreted from the occurrence of impact melts', in *Impact and explosion cratering: Planetary and terrestrial implications; Proceedings of the Symposium on Planetary Cratering Mechanics*. Flagstaff, AZ: New York, Pergamon Press, Inc, pp. 791–814.

Hays, F. (1976) 'Crystallization history of lunar picritic basalt sample 12002 : Phase-equilibria and cooling-rate studies', *Geological Society of America Bulletin*, 2(60502), pp. 646–656.

Heier, K. (1955) 'The formation of feldspar perthites in highly metamorphic gneisses', *Norsk Geologisk Tidsskrift*, 35, pp. 87–92.

Hubbard, N. J. *et al.* (1971) 'The composition and derivation of Apollo 12 soils', *Earth and Planetary Science Letters*, 10(3), pp. 341–350. doi: 10.1016/0012-821X(71)90040-9.

Humayun, M., Nemchin, A., Zanda, B., Hewins, R. H., Grange, M., Kennedy, A., Lorand, J.-P., *et al.* (2013) 'Origin and age of the earliest Martian crust from meteorite NWA 7533', *Nature*, 503(7477), pp. 513–516. doi: 10.1038/nature12764.

Humayun, M., Nemchin, A., Zanda, B., Hewins, R. H., Grange, M., Kennedy, A., Lorand, J. P., *et al.* (2013) 'Origin and age of the earliest Martian crust from meteorite NWA 7533', *Nature*, pp. 513–516. doi: 10.1038/nature12764.

Jakovsky, B. M. and Philips, R. J. (2001) 'Mars'volatile and climate history', *Nature*, 412(6843), p. 237.

Judd, J. W. and Cole, G. A. (1883) 'On the basalt-glass (tachylyte) of the Western Isles of Scotland', *Quarterly Journal of the Geological Society*, 34(1–4), pp. 444–465.

Kaplan, L. D., Münch, G. and Spinrad, H. (1964) 'An analysis of the spectrum of Mars', *Astrophysical Journal*, 139(1), pp. 1–15.

Kiefer, W. S. *et al.* (2015) 'The effects of mantle composition on the peridotite solidus: implications for the magmatic history of Mars', *Geochimica et Cosmochimica Acta*, 162(0), pp. 247–258.

Kirby, S. H. and Christie, J. M. (1977) 'Mechanical twinning in diopside Ca(Mg,Fe)Si2O6: Structural mechanism and associated crystal defects', *Physics and Chemistry of Minerals*. Springer-Verlag, 1(2), pp. 137–163. doi: 10.1007/BF00307315.

Kirkpatrick, R. J. (1975) 'Crystal growth from the melt: a review', *Am. Mineral.*, 60, pp. 798–814.

Kretz, R. (1963) 'Distribution of magnesium and iron between orthopyroxene and calcic pyroxene in natural mineral assemblages', *The Journal of*

Geology, 71(6), pp. 773–785.

Kretz, R. (1982) 'Transfer and exchange equilibria in a portion of the pyroxene quadrilateral as deduced from natural and experimental data', *Geochimica et Cosmochimica Acta*, 46(3), pp. 411–421. doi: 10.1016/0016-7037(82)90232-0.

Krumbein, W. C. (1941) 'Measurement and geological significance of shape and roundness of sedimentary particles', *Journal of Sedimentary Research*, 11(2), pp. 64–72.

Leroux, H. (2001) 'Microstructural shock signatures of major minerals in meteorites', *European Journal of Mineralogy*, 13(2), pp. 253–272. doi: 10.1127/0935-1221/01/0013-0253.

Leroux, H. *et al.* (2016) 'Exsolution and shock microstructures of igneous pyroxene clasts in the Northwest Africa 7533 Martian meteorite', *Meteoritics and Planetary Science*, 51(5), pp. 932–945. doi: 10.1111/maps.12637.

Lindsley, D. H. (1983) 'Pyroxene thermometry', *American Mineralogist*. Mineralogical Society of America, 68(5–6), pp. 477–493.

Lindsley, D. H. and Andersen, D. J. (1983) 'A two-pyroxene thermometer', *Journal of Geophysical Research*, 88(S02), pp. 887–906. doi: 10.1029/jb088is02p0a887.

Lindsley, D. H. and Fuhrman, M. L. (1988) 'Ternary-feldspar modeling and thermometry', *American Mineralogist*, 73(3–4), pp. 201–215.

Liu, Y. *et al.* (2016) 'Rare-earth-element minerals in martian breccia meteorites NWA 7034 and 7533: Implications for fluid–rock interaction in the martian crust', *Earth and Planetary Science Letters*. Elsevier B.V., 451, pp. 251–262. doi: 10.1016/j.epsl.2016.06.041.

Lofgren, G. (1974) 'An experimental study of plagioclase crystal morphology; isothermal crystallization.', *American Journal of Science*, 274(3), pp. 243–273.

Lorand, J. P. *et al.* (2015) 'Nickeliferous pyrite tracks pervasive hydrothermal alteration in Martian regolith breccia: A study in NWA 7533', *Meteoritics and Planetary Science*, 50(12), pp. 2099–2120. doi: 10.1111/maps.12565.

Ma, C. *et al.* (2016) 'Ahrensite, γ-Fe2SiO4, a new shock-metamorphic mineral from the Tissint meteorite: Implications for the Tissint shock event on Mars', *Geochimica et Cosmochimica Acta*. Elsevier Ltd, 184, pp. 240–256. doi: 10.1016/j.gca.2016.04.042.

Mahajan, R. R. (2015) 'Martian rocks that reached to Earth were ejected in 10 possible ejection events', *46th Lunar and Planetary Science Conference (2015)*, pp. 11–12.

Mccoy, T. J. *et al.* (2008) 'Structure , stratigraphy , and origin of Husband Hill , Columbia Hills , Gusev Crater , Mars', *Journal of Geophysical Research*, 113(E6), pp. 1–14. doi: 10.1029/2007JE003041.

McCubbin, F. M. *et al.* (2009) 'Hydrothermal jarosite and hematite in a pyroxene-hosted melt inclusion in martian meteorite Miller Range (MIL) 03346 : Implications for magmatic-hydrothermal fluids on Mars', *Geochimica et Cosmochimica Acta*. Elsevier Ltd, 73(16), pp. 4907–4917. doi: 10.1016/j.gca.2009.05.031.

McCubbin, F. M. *et al.* (2016) 'Geologic history of Martian regolith breccia Northwest Africa 7034: Evidence for hydrothermal activity and lithologic diversity in the Martian crust', *Journal of Geophysical Research E: Planets*, 121, pp. 2120–2149. doi: 10.1002/2016JE005143.

McSween, H. Y. *et al.* (2006) 'Alkaline volcanic rocks from the Columbia Hills, Gusev crater, Mars', *Journal of Geophysical Research E: Planets*. doi: 10.1029/2006JE002698.

McSween, H. Y. *et al.* (2008) 'Mineralogy of volcanic rocks in Gusev Crater, Mars: Reconciling Mössbauer, Alpha Particle X-Ray Spectrometer, and Miniature Thermal Emission Spectrometer spectra', *Journal of Geophysical Research: Planets*, 113(E6).

McSween, H. Y. (2015) 'Petrology on Mars', *American Mineralogist*. doi: 10.2138/am-2015-5257.

McSween, H. Y., Labotka, T. C. and Viviano-Beck, C. E. (2015) 'Metamorphism in the Martian crust', *Meteoritics and Planetary Science*, 50(4), pp. 590–603. doi: 10.1111/maps.12330.

Michot, P. (1951) 'Essai sur la géologie de la catazone', *Bull. Acad. roy. Belg., Cl. des Sciences*, pp. 260–76.

Ming, D. W. *et al.* (2008) 'Geochemical properties of rocks and soils in Gusev Crater, Mars: Results of the Alpha Particle X-Ray Spectrometer from Cumberland Ridge to Home Plate', *Journal of Geophysical Research E: Planets*, 113(12). doi: 10.1029/2008JE003195.

Miyamoto, M., Duke, M. B. and McKay, D. S. (1985) 'Chemical zoning and homogenization of pasamonte-type pyroxene and their bearing on thermal metamorphism of a Howardite parent body', *Journal of Geophysical Research*, 90(S02), p. C629. doi: 10.1029/jb090is02p0c629.

Mojzsis, S. J. and Arrhenius, G. (1997) 'Early Mars and early Earth: paleoenvironments for the emergence of life', in *Proc. SPIE 3111, Instruments, Methods, and Missions for the Investigation of Extraterrestrial Microorganisms*, pp. 162–163. doi: https://doi.org/10.1117/12.278769.

Morse, J. A. (1970) 'Alkali feldspars with water at 5 kb. pressure', *Journal of Petrology*, 11, pp. 221–253.

Muttik, N. *et al.* (2014) 'Inventory of H2O in the ancient Martian regolith from Northwest Africa 7034: The important role of Fe oxides', *Geophysical Research Letters*, 41, pp. 8235–8244. doi: 10.1002/2014GL062533.Received.

Norton, W. H. (1917) 'A classification of Breccias', *The Journal of Geology*, 25(2), pp. 160–194.

Nyquist, L. E. *et al.* (2013) 'NWA 7034 MARTIAN BRECCIA: DISTURBED Rb-Sr SYSTEMATICS, PRELIMINARY ~4.4 Ga Sm-Nd AGE', *Science Space Science Reviews*, 90(5318), p. 7034. doi: 10.1038/natcomm2414.

Nyquist, L. E. *et al.* (2016) 'Rb-Sr and Sm-Nd isotopic and REE studies of igneous components in the bulk matrix domain of Martian breccia Northwest Africa 7034', *Meteoritics and Planetary Science*, 51(3), pp. 483–498. doi: 10.1111/maps.12606.

Owen, T. *et al.* (1977) 'The composition of the atmosphere at the surface of Mars', *Journal of Geophysical Research*. John Wiley & Sons, Ltd, 82(28), pp. 4635–4639. doi: 10.1029/JS082i028p04635.

Pasero, M. (2018) *The New IMA List of Minerals – A Work in Progress – Updated: November 2018*. International Mineralogical Association (IMA), Commission on New Minerals Nomenclature and Classification (CNMNC).

Phillips, J. A. (1879) 'A Contribution to the History of Mineral Veins', *Quarterly Journal of the Geological Society*, 35(1–4), pp. 390–396.

Pirrie, D. *et al.* (2002) 'QemSCAN—a fully automated quantitative SEM-based mineral analysis system', in *Forensic Geoscience: Principles. Techniques and Applications*. Geological Society of London. doi: 10.1163/_q3_SIM_00374.

Poldervaart, A. and Hess, H. H. (1951) 'Pyroxenes in the crystallization of basaltic magma', *The Journal of Geologyhe Journal of Geology*, 59(5), pp. 472–489. doi: 10.1086/625891.

Prasad, V. and Naidu, M. G. C. (1971) 'On pyroxene twinning', *Norsk Geologisk Tidsskrift*, 51, pp. 15–23.

Santos, A. R., Agee, C. B., McCubbin, F. M., Shearer, C. K., Burger, P. V., *et al.* (2013) 'Apatite and merrillite from Martian meteorite NWA 7034', in *44th Lunar and Planetary Science Conference*, p. LPSC-2013-1486. doi: 10.1029/2005JE002544.

Santos, A. R., Agee, C. B., McCubbin, F. M., Shearer, C. K. and Burger, P. V. (2013) 'Martian breccia NWA 7034: Basalt, mugearite, and trachyandesite clasts', *76th Annual Meteoritical Society Meeting*, 212, p. 7034. doi: 10.1038/natcomm2414.

Santos, A. R. *et al.* (2015) 'Petrology of igneous clasts in Northwest Africa 7034: Implications for the petrologic diversity of the martian crust', *Geochimica et Cosmochimica Acta*. Elsevier Ltd, 157, pp. 56–85. doi: 10.1016/j.gca.2015.02.023.

Schmidt, M. E. *et al.* (2014) 'Geochemical diversity in first rocks examined by the Curiosity rover in Gale crater: Evidence for and significance of an alkali and volatile-rich igneous source', *Journal of Geophysical Research*, 119, pp. 64–81. doi: 10.1002/2013JE004481.

Schwertmann, U. (1958) 'The Effect of Pedogenic Environments on Iron Oxide Minerals', *Advances in soil science*. Springer, New York, NY, pp. 171–200. doi: 10.1007/978-1-4612-5046-3_5.

Shaw, H. R. (1965) 'Comments on viscosity, crystal settling, and convection in granitic magmas', *American Journal of Science*, 263(2), pp. 120–152.

Shoemaker, E. M. and Chao, E. C. T. (1961) 'New evidence for the impact origin of the Ries Basin, Bavaria, Germany', *Journal of Geophysical Research*, 66(10), pp. 3371–3378.

Shore, M. and Fowler, A. D. (1996) 'Oscillatory zoning in minerals: A common phenomenon', *Canadian Mineralogist*, 34(6), pp. 1111–1126.

Smith, K. C. A. and Oatley, C. W. (1955) 'The scanning electron microscope and its fields of application', *British Journal of Applied Physics*, 6(11), p. 391.

Steno, N. (1669) *Dissertationis prodromus*. Accademia della Crusca.

Stöffler, D. (1966) 'Zones of impact metamorphism in the crystalline rocks of the Nördlinger Ries crater', *Contributions to Mineralogy and Petrology*, 12(1), pp. 15–24.

Stöffler, D. . *et al.* (1986) 'Shock metamorphism and petrography of the Shergotty achondrite', *Geochimica et Cosmochimica Acta*, 50(6), pp. 889–903. doi: 10.1016/0016-7037(86)90371-6.

Stolper, E. M. *et al.* (2013) 'The petrochemistry of Jake_M: A martian mugearite', *Science*, 341(6153). doi: 10.1126/science.1239463.

Streckeisen, A. (1974) 'Classification and Nomenclature of Plutonic Rocks. Recommendations of the IUGS Subcomission on the Systematics of Igneous Rocks', *Geologische Rundschau*, 63(2), pp. 773–786.

Tanaka, K. L. (1986) 'The stratigraphy of Mars', *Journal of Geophysical Research: Solid Earth*, 91(B13), pp. E139–E158.

Thomson, B. J. *et al.* (2011) 'Constraints on the origin and evolution of the layered mound in Gale Crater , Mars using Mars Reconnaissance Orbiter data', *Icarus*. Elsevier Inc., 214(2), pp. 413–432. doi: 10.1016/j.icarus.2011.05.002.

Trail, D., Mojzsis, S. . and Harrison, T. M. (2004) 'Inclusion mineralogy of pre-4.0 Ga zircons from Jack Hills , Western Australia : A progress report', in *Geochimica et Cosmochimica Acta*. Pergamon-Elsevier Science, pp. A743–A743.

Tschermak, G. (1872) *Die meteoriten von Shergotty und Gopalpur*. KK Hof-und Staatsdruckerei.

Udry, A. *et al.* (2014) 'Petrogenesis of a vitrophyre in the martian meteorite breccia NWA 7034', *Geochimica et Cosmochimica Acta*. Elsevier Ltd,

141, pp. 281–293. doi: 10.1016/j.gca.2014.06.026.

Vance, J. A. (1962) 'Zoning in igneous plagioclase; normal and oscillatory zoning', *American Journal of Science*, 260(10), pp. 746–760.

Wackerle, J. (1962) 'Shock-wave compression of quartz', *Journal of Applied Physics*, 33(3), pp. 922–937.

Wager, L. R., Brown, G. M. and Wadsworth, W. J. (1960) 'Types of Igneous Cumulates', *Journal of Petrology*, 1(1), pp. 73–85.

Wahl, W. (1952) 'The brecciated stony meteorites and meteorites containing foreign fragments', *Geochimica et Cosmochimica Acta*, 2(2), pp. 91–117.

Watts, G. (1804) 'Observations on Basalt , and on the Transition from the Vitreous to the Stony Texture , Which Occurs in the Gradual Refrigeration of Melted Basalt ; With Some Geological Remarks Author (s): Gregory Watt Source : Philosophical Transactions of the Royal S', *Philosophical Transactions of the Royal Society of London*, 94, pp. 279–314.

Werner, S. C. (2008) 'The early martian evolution — Constraints from basin formation ages', *Icarus*, 195, pp. 45–60. doi: 10.1016/j.icarus.2007.12.008.

Werner, S. C. (2009) 'The global Martian volcanic evolutionary history', *Icarus*, 201(1), pp. 44–68.

Wetherill, G. W. (1975) 'Late heavy bombardment of the moon and terrestrial planets', in *Lunar and Planetary Science Conference Proceedings*.

Wittmann, A. *et al.* (2015) 'Petrography and composition of Martian regolith breccia meteorite Northwest Africa 7475', *Meteoritics & Planetary Science*, 50(2), pp. 326–352. doi: 10.1111/maps.12425.

Wright, T. L. and Okamura, R. T. (1977) 'Cooling and crystallization of tholeiitic basalt, 1965 Makapuhi lava, Hawaii', *US Geological Survey Professional Paper*, 1004.

Yin, Q. *et al.* (2014) 'An Earth-like beginning for ancient Mars indicated by alkali-rich volcanism at 4.4 Ga', in *45th Lunar and Planetary Science Conference*. doi: 10.1126/science.1239463.

Yoder, H. S. J., Steward, D. B. and Smith, J. V. (1957) 'Ternary feldspars', *Ann. Rep. Geophys. Lab. Carn. Inst. Wash. Yrbk.*, 56, pp. 206–214.

Zubrin, R. (2015) 'COLONISING THE RED PLANET HUMANS TO MARS IN OUR TIME', *Special issue: Space Architecture*, 84(6), pp. 46–53.

Zubrin, R. and Baker, D. (1991) 'Humans to Mars in 1999', in *NASA, Washington, Space Transportation Propulsion Technology Symposium. Volume 3: Panel Session Summaries and Presentations;*, pp. 881–891.

Zworykin, V. K. and Ramberg, E. G. (1941) 'Surface studies with the electron microscope', *Journal of Applied Physics*, 12(9), pp. 692–695.